Measurement of ω Meson Production in pp and p–Pb Collisions at $\sqrt{s_{\scriptscriptstyle {\rm NN}}}=5.02$ TeV with ALICE

MASTER THESIS at the Institute for Nuclear Physics

submitted by

NICOLAS STRANGMANN

Department of Physics Goethe University Frankfurt am Main

November 2023

FIRST REFEREE: Prof. Dr. Henner Büsching SECOND REFEREE: Prof. Dr. Harald Appelshäuser

CONTENTS

| 0 | Intr | oduction 1 | | | | | | |
|---|---|--|--|--|--|--|--|--|
| 1 | Phy | Physics Context 3 | | | | | | |
| | 1.1 | | | | | | | |
| | 1.2 QCD Evolution in Extreme Environments 6 | | | | | | | |
| | | 1.2.1 Color Glass Condensate 7 | | | | | | |
| | | 1.2.2 Phase Diagram of QCD 8 | | | | | | |
| | 1.3 | | | | | | | |
| | | 1.3.1 Proton-Proton Collisions 10 | | | | | | |
| | | 1.3.2 Lead–Lead Collisions 11 | | | | | | |
| | | 1.3.3 Proton–Lead Collisions 13 | | | | | | |
| | 1.4 | Monte Carlo Event Generators 15 | | | | | | |
| | 1.5 | Related Work 15 | | | | | | |
| 2 | Experiment 18 | | | | | | | |
| | 2.1 | Particle Acceleration at CERN 18 | | | | | | |
| | 2.2 | A Large Ion Collider Experiment 20 | | | | | | |
| | | 2.2.1 Inner Tracking System (ITS) 21 | | | | | | |
| | | 2.2.2 Forward Trigger Detectors (V0 and T0) 22 | | | | | | |
| | | 2.2.3 Time Projection Chamber (TPC) 22 | | | | | | |
| | | 2.2.4 Time Of Flight (TOF) Detector 23 | | | | | | |
| | | 2.2.5 Electromagnetic Calorimeter (EMCal) 24 | | | | | | |
| | 2.3 | 3 Analysis Framework 25 | | | | | | |
| 3 | Data | asets and Event Selection 26 | | | | | | |
| 4 | Pior | n Reconstruction 29 | | | | | | |
| | 4.1 | Charged Pion Reconstruction 29 | | | | | | |
| | 4.2 | Photon Reconstruction 32 | | | | | | |
| | | 4.2.1 Photon Measurement with the EMCal 33 | | | | | | |
| | | 4.2.2 The Photon Conversion Method (PCM) 35 | | | | | | |
| | 4.3 | Neutral Pion Reconstruction 37 | | | | | | |
| 5 | Om | Omega Meson Reconstruction 41 | | | | | | |
| | 5.1 | Mass Resolution Correction 41 | | | | | | |
| | 5.2 | Background Studies 47 | | | | | | |
| | | 5.2.1 Background Contributions 47 | | | | | | |
| | | 5.2.2 Feasibility of a ρ Prefilter 48 | | | | | | |
| | | 5.2.3 Impact of Possible DCA Restrictions 50 | | | | | | |
| | 5.3 | Signal Extraction 51 | | | | | | |

| 6 | Signal Processing 55 | | | | | | | |
|---|--|---|----|--|--|--|--|--|
| | 6.1 | Spectra Corrections 55 | | | | | | |
| | 6.2 | Calculation of the Nuclear Modification Factor 57 | | | | | | |
| | 6.3 | 5.3 Systematic Uncertainties 59 | | | | | | |
| | 6.3.1 $p_{\rm T}$ Independent Uncertainties 59 | | | | | | | |
| | | 6.3.2 Uncertainties from the Signal Extraction | 61 | | | | | |
| | | 6.3.3 Uncertainties from the Selection Criteria | 63 | | | | | |
| | 6.4 | Combination of Reconstruction Methods 66 | | | | | | |
| | 6.5 | Finite Bin Width Correction 71 | | | | | | |
| 7 | Results 73 | | | | | | | |
| | 7.1 | Invariant Cross-Sections 73 | | | | | | |
| | 7.2 | ω/π^0 Ratios 75 | | | | | | |
| | 7.3 | Nuclear Modification Factor 78 | | | | | | |
| 8 | 8 Summary and Outlook 80 | | | | | | | |
| A | Appendix 83 | | | | | | | |
| | A.1 | Runlists 83 | | | | | | |
| | A.2 | Unexpected TOF Signals 84 | | | | | | |
| | A.3 | Pion and Photon Observables in pp Collisions | 86 | | | | | |
| | A.4 | Uncertainties 88 | | | | | | |
| | A. 5 | Invariant-Mass Distributions 90 | | | | | | |
| | | | | | | | | |
| | Bibl | iography 105 | | | | | | |
| | Ack | nowledgments 115 | | | | | | |
| | Dec | leration 117 | | | | | | |

INTRODUCTION

All matter within the visible universe is composed of atoms. At the core of each atom resides a nucleus, consisting of nucleons – protons and neutrons. These nucleons, upon closer examination, reveal a substructure of three quarks. These quarks typically only exist in pairs or triplets confined within hadrons. There is, however, a notable exception to this rule in the form of the Quark Gluon Plasma (QGP), which is believed to emerge at extremely high energy densities caused either by large temperatures or baryon densities. In these extreme conditions, quarks are deconfined from their hadrons and traverse the QGP quasi-free.

The necessary temperatures for developing a QGP are believed to be reached at highly energetic collisions of heavy ions at the largest and most powerful accelerator in the world, the Large Hadron Collider (LHC). The ALICE experiment at the LHC is dedicated to the study of heavy-ion collisions. Besides the QGP, the ALICE experiment is utilized to isolate so-called Cold Nuclear Matter (CNM) effects caused by the hadrons being bound within nuclei. These effects are commonly studied in p-Pb collisions, where CNM effects are expected within the lead nucleus; however, the energy density in the collision is not expected to reach the threshold of the QGP formation.

While there has been extensive research in recent years on the production of pseudoscalar mesons (π, η, K) as evidenced by studies such as [Abe+12; Ach+18b; Aai+23], the investigation into vector mesons like the ω has received comparatively less attention. This scarcity of experimental data not only hampers theoretical models to better describe the production of vector mesons but also increases systematic uncertainties of direct photon measurements, which serve as direct probes of the QGP.

In an effort to address this gap, the production of ω mesons in pp and p-Pb collisions is measured at $\sqrt{s_{\rm NN}}=5.02$ TeV and presented in this thesis. From the measured production cross-sections in the two collision systems, the respective ω/π^0 ratios are calculated, as well as the first measured nuclear modification factor $R_{\rm pPb}$ of the ω meson at LHC energies.

The presented measurement of ω mesons in pp and p-Pb collisions is guided by three primary motivations, as outlined in the following.

1. Theoretical models describe the production of particles in hadronic collisions using Parton Distribution Functions (PDFs) and Fragmentation Functions (FFs). Measurements of the production of particles, such as the ω meson, can constrain these functions and thereby further our understanding of the different processes involved in a particle collision. The measured production cross-sections can also be compared

- to Monte-Carlo (MC) event generators such as PYTHIA, EPOS LHC, and DPMJET to test their description of ω mesons based on the various phenomenological models.
- 2. Comparisons of the ω meson production in p-Pb collisions to the reference measurement in pp collisions are sensitive to possible CNM effects induced by partons being bound within the lead nucleus. The measurements in both collision systems furthermore serve as a reference for future studies of the QGP in Pb-Pb collisions.
- 3. Measurements of real and virtual direct photons, as probes of the QGP, require experimental data on neutral meson production to describe the background of decay photons. As decays of ω mesons are the third largest contributor to this background [Ada+16], precise measurements of their production serve as vital input for measurements of direct photons. This becomes especially important in smaller collision systems like pp and p-Pb, where the direct photon signal is expected to be small.

This thesis is structured into eight chapters: The introduction is followed in chapter 1 by an overview of the theoretical foundations and related work that motivate this analysis. The subsequent chapter 2 contains a brief description of the ALICE experiment, where the datasets, outlined in chapter 3, are recorded. Chapter 4 describes how the charged and neutral pions are measured, from which the ω mesons are reconstructed, as portrayed in chapter 5. The extracted yields are then corrected and combined in chapter 6, leading to the final spectra presented and discussed in chapter 7. Chapter 8 concludes this thesis with a summary and outlook of future prospects of ω meson analyses.

1

PHYSICS CONTEXT

This chapter provides the context necessary to understand the analysis steps and to interpret the results presented in this thesis. With mesons being at the center of this work, the first section 1.1 outlines their role within the standard model of particle physics. Looking for the origin of ω mesons, section 1.2 introduces extreme states of matter in Quantum Chromodynamics (QCD). These unique environments of QCD can be probed, as done in this analysis, through particle collisions of various sizes, as explained in section 1.3. With MC event generators playing a crucial role in the analysis of these collisions, they are briefly characterized in section 1.4 before this chapter concludes with section 1.5 and a compilation of previous related analyses.

1.1 MESONS IN THE STANDARD MODEL OF PARTICLE PHYSICS

The standard model of particle physics describes all known elementary particles as well as three out of the four known fundamental forces within one coherent theory. According to the standard model, all matter consists of six (anti-) quarks, and six (anti-) leptons with five bosons carrying the forces between them. As the linear potential of the strong interaction prohibits free color charge, (anti-) quarks are always found in color neutral groups of two or more, called hadrons. While hadrons, consisting of three (anti-) quarks, are called baryons, mesons are pairs of a quark and an antiquark. All known mesons are unstable and decay into leptons, photons, or hadrons (protons and neutrons). The finite lifetime τ of any unstable state corresponds to an uncertainty of its energy E, according to the Heisenberg uncertainty principle $\Delta E \Delta \tau > \hbar/2$ [MT45]. This translates to an uncertainty of a particle's mass, manifested as a width Γ when measuring the mass of the particles as follows:

$$\Gamma = 2\Delta E = \hbar/\tau. \tag{1.1}$$

Mesons are classified into J^P multiplets according to their spin J and parity P. The parity of a meson with angular momentum l is $P=(-1)^{l+1}$. In the following, only the orbital ground states (l=0) are considered, which therefore have an uneven parity (P=-1). Within the so-called eightfold way [GM61], combinations of the 3 light quarks u, d, and u and u antiquarks can be decomposed into an octet u and a singlet u state: u and u state: u and u shows these nine combinations ordered in one nonet for pseudoscalar mesons with anti parallel spins (u by u and one nonet for vector mesons with parallel spins (u by u by u

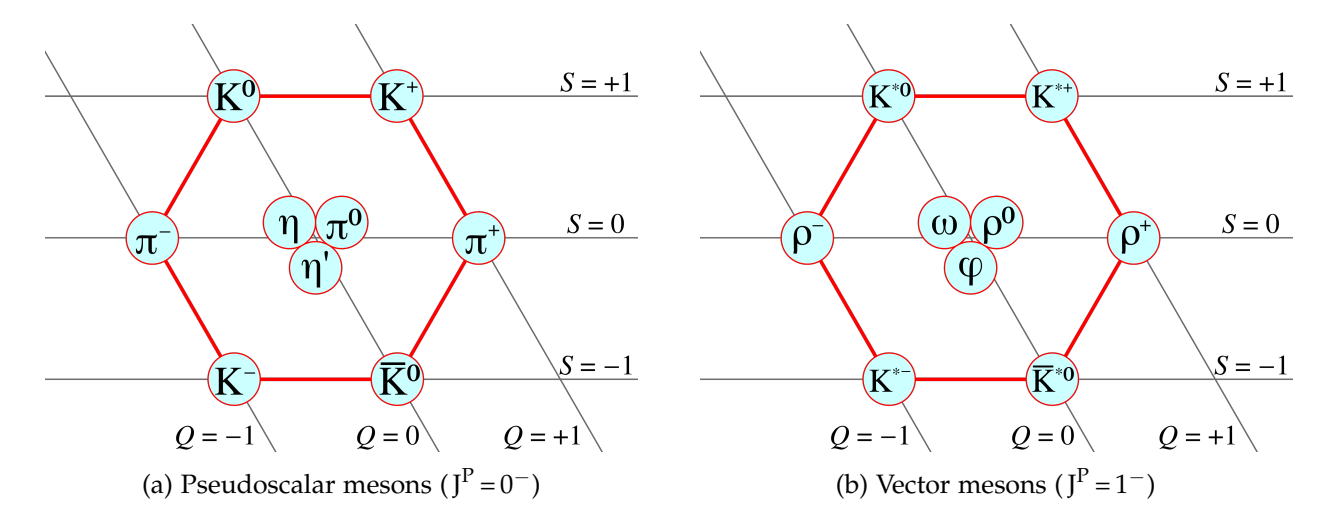


Figure 1.1: Combinations of u, d and s (anti-)quarks forming one nonet of pseudoscalar (J=0) and one of vector (J=1) mesons [SE]

middle row contains mesons without net strangeness (S=0). In the pseudoscalar sector, this row comprises the isospin triplet (I=1) of pions and the singlet (I=0) formed by a combination of η and η' . The ρ mesons make up the isospin triplet of vector mesons, with the singlet state being a combination of the ϕ and ω meson. The two isoscalar singlet states in both nonets are a combination of two mesons (η/η' and ω/ϕ), as they have the same quantum numbers (Q=S=I=0) and therefore mix [Ams18]. The composition of these mixed states can be described using a linear combination of the SU(3) singlet and octet wavefunctions:

$$|\psi_1\rangle = |u\bar{u} + d\bar{d} + s\bar{s}\rangle / \sqrt{3}$$

$$|\psi_8\rangle = |u\bar{u} + d\bar{d} - 2s\bar{s}\rangle / \sqrt{6}.$$
(1.2)

The observed wavefunctions of the ω and ϕ meson are a sum of the singlet and octet wavefunction weighted by the mixing angle of the vector mesons θ_V .

$$\phi = |\psi_8\rangle \cos \theta_V - |\psi_1\rangle \sin \theta_V$$

$$\omega = |\psi_8\rangle \sin \theta_V + |\psi_1\rangle \cos \theta_V \tag{1.3}$$

The mixing angle θ_V between the two singlet states can be calculated from the masses of the vector mesons using the following equation [Ams18]:

$$\theta_V = \arctan\left(\sqrt{\frac{4m_{K^*} - m_{\rho} - 3m_{\phi}}{-4m_{K^*} + m_{\rho} + 3m_{\omega}}}\right) \simeq 36.5^{\circ}.$$
 (1.4)

This angle happens to cause almost ideal separation of the quarks into the two mesons with the ω mesons wavefunction only containing around 2 % strangeness. Its wavefunction can therefore be approximated as a superposition of the up and down (anti-)quarks, as shown in Table 1.1, while the ϕ meson can be approximated as a pure $s\bar{s}$ state.

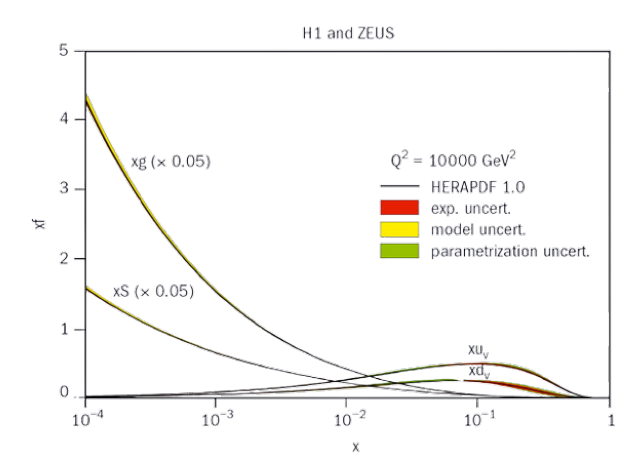
| | Quark content | $m \text{ (MeV/}c^2\text{)}$ | Γ | сτ |
|---------|--|------------------------------|------------------------|-----------------|
| ω | $\frac{1}{\sqrt{2}}\left[\left u\bar{u}\right\rangle + \left d\bar{d}\right\rangle\right]$ | 782.65 | $8.49 \text{ MeV}/c^2$ | 23.2 fm |
| π^0 | $\left \frac{1}{\sqrt{2}} \left[u\bar{u}\rangle - d\bar{d}\rangle \right] \right $ | 134.98 | $7.7 \text{ eV}/c^2$ | 25.5 nm |
| π^+ | $ uar{d}\rangle$ | 139.57 | $25 \text{ neV}/c^2$ | 7.8 m |
| π^- | $ dar{u} angle$ | 139.57 | $25 \text{ neV}/c^2$ | $7.8\mathrm{m}$ |

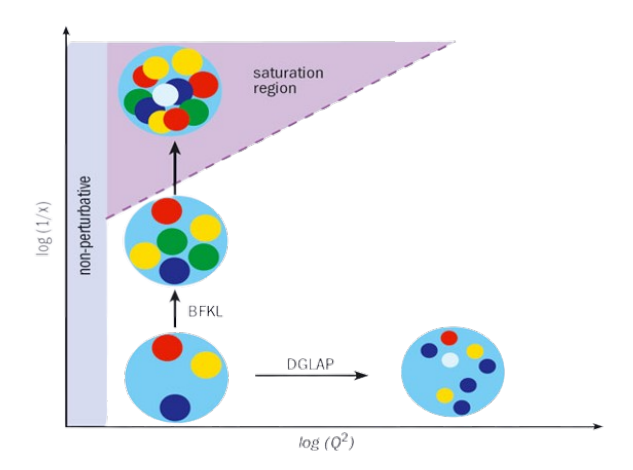
Table 1.1: Properties of the ω meson and the pions it decays into [Pdg22]

As the ω meson is an unstable particle, measurements of its production, as presented in this thesis, require a good understanding of how and when the ω meson decays. Particle decays are often described by Fermi's golden rule [Fer74], where in the case of the ω meson decay, the conservation of G-parity plays an important role. G-parity is a multiplicative quantum number that is a generalization of C-parity to include charged particles using their isospin. Because the C-parity and the isospin are conserved under strong interaction, so is the G-parity. Both the ω meson and all pions have a negative G-parity. This means the decay of the ω meson into pions is only possible under the strong interaction with an uneven number of pions. Therefore, the ω meson predominantly decays into three pions, with a branching ratio of $\mathcal{B}(\omega \to \pi^+\pi^-\pi^0) = 89\%$ [Pdg22], motivating its use for the reconstruction of the ω in the analysis presented in this thesis. The measured Full Width at Half Maximum (FWHM) of the ω meson $\Gamma = 8.49$ MeV/ c^2 [Pdg22] can be converted using equation 1.1 into a lifetime of $\tau_{\omega} = 23.2$ fm/c.

Pions are by far the lightest hadrons with a mass more than three times smaller than the next lightest hadrons, the kaons [Pdg22]. Table 1.1 shows the quark composition, measured masses, and respective widths of the pions. While one observes very similar masses of the charged and neutral pions, their lifetimes and, therefore, widths differ drastically. This difference comes from their particular decays:

As pions are the lightest hadrons, they can only decay into leptons and bosons, prohibiting strong decays. The neutral pion decays almost exclusively into two photons with a branching ratio of $\mathcal{B}\left(\pi^0\to\gamma\gamma\right)=98.8\,\%$. This electromagnetic decay comes with a lifetime of $\tau_{\pi^0}=25.5\,\mathrm{nm/c}$, which is much larger than that of the ω stated above. This results in a small width of the π^0 of $\Gamma=7.7\,\mathrm{eV/c^2}$ compared to its mass of $M_{\pi^0}=135\,\mathrm{MeV/c^2}$ [Pdg22]. Due to charge conservation, charged pions can not decay into only photons. As no hadron is lighter than pions, they can only decay into leptons. Parity violation of the weak interaction and helicity considerations yield that the decay into an electron and a neutrino is strongly suppressed, leaving only the decay into a muon and the corresponding neutrino [Pov+13]. This decay therefore has a very large branching ratio of $\mathcal{B}\left(\pi^+\to\mu^++\nu_\mu\right)=\mathcal{B}\left(\pi^-\to\mu^-+\bar{\nu}_\mu\right)=99.98\,\%$. As this is a weak decay with a small phase space available due to the similar masses of the pion and the muon $(m_{\pi^\pm}\approx\frac43m_{\mu^\pm})$, the lifetime of the pion is rather large with $\tau_{\pi^\pm}=7.8\,\mathrm{m/c}$ [Pdg22].





- (a) The Parton Distribution Functions of the proton measured by H₁ and ZEUS at fixed Q^2 are dominated by gluon (xg) and sea-quark (xS) contributions at low x.
- (b) While the DGLAP equations describe the QCD evolution with rising momentum transfer Q, the BFKL equation describes its behavior at decreasing momentum fraction x.

Figure 1.2: Dependance of parton distributions on the momentum transfer Q and the partons momentum fraction x at which it is probed [Dia10]

1.2 QCD EVOLUTION IN EXTREME ENVIRONMENTS

Quantum Chromodynamics (QCD) is a Quantum Field Theory (QFT) describing the strong interaction between color-charged quarks and gluons. Combinations of these fundamental partons make up hadrons, as described in the previous section. In addition to the constituent quarks, defining the charge of a hadron, the special nature of QCD also predicts the existence of virtual, short-lived quarks and gluons. The composition of partons within a hadron is quantified by so-called PDFs. These describe the probability of finding a specific parton with a momentum fraction (x) of the total hadron between x and x + dx. Figure 1.2a shows measurements of the PDFs of a proton by the H₁ and ZEUS working groups at a fixed momentum transfer of $Q^2 = 10000 \,\text{GeV}^2$. When probing relative momenta of $x \approx 1/3$, the largest contribution comes from the constituent quarks of the proton (uud). At smaller relative momenta, one finds more and more short-lived vacuum fluctuations in the form of sea quarks and gluons. The evolution of the PDFs at fixed momentum transfer and decreasing momentum fraction ($x \to 0$) is called the Regge-Gribov limit and is experimentally achieved by increasing the center of mass energy $\sqrt{s} \rightarrow \infty$ while keeping the transverse momentum constant [Gel+10]. Growth of the gluon density is observed at small-x, which arises due to gluon splitting $(g \rightarrow gg)$ [Kan19]. The sea quark density also rises here, as they are produced in gluon splitting $g \rightarrow q\bar{q}$. However, as their production is suppressed by one power of the coupling constant α_S in the splitting, the sea quark density is negligible at very low x [GEL13]. Figure 1.2b depicts the QCD evolution with changing Q and x. The described Regge-Gribov limit $(Q^2, x \to 0)$ corresponds to the two vertical arrows showing the rising density within the nucleus. This experimentally observed rapid rise of the gluon density at small-x is described by the Balitsky-Fadin-Kuraev-Lipatov (BFKL) equation [Gel+10]. When the increasing number of confined gluons in the nucleus leads to overlap and therefore recombination ($gg \rightarrow g$), the gluon density saturates [Kan19]. A description of the properties of saturated gluons in the Regge-Gribov limit is given by the Color Glass Condensate (CGC).

1.2.1 Color Glass Condensate

Saturated low-x gluons are theorized within an effective field theory as a new type of matter called Color Glass Condensate (CGC) [McLo8a; McLo8b]. The following three paragraphs outline the concept of CGC following the three components of its name.

COLOR As this proposed new form of matter consists of gluons, which only interact strongly via their color charge, the name of this effective theory contains the charge defining all fields and interactions within: *color*.

GLASS The highly energetic hadrons contain very fast gluons, whose interactions are slowed down by Lorentz-time dilation [GEL13]. This property of behaving like a solid on short time scales, but a liquid on long ones, prompts the word *glass* to be borrowed from silica, where similar behavior is observed [McLo2]. The CGC as an effective theory uses this to approximate the low *x* gluons by static classical fields [McLo8a].

The packing of more and more gluons into a hadron can be illustrated CONDENSATE by thinking of the gluons as hard spheres [McLo8b]. With a Lorentz gamma factor of $\gamma \sim 1000$ in heavy ion collisions at the LHC, the hadron and therefore this sphere analogy can be described as a two-dimensional circle in the transverse plane. The size of the gluon can be approximated by their De Broglie wavelength in the transverse plane $r_{\rm T} \sim 1/p_{\rm T}$ [McLo8b]. Gluons of fixed size (momentum) can be added to the hadron until they start to overlap. At this point the number of gluons can still increase, however, their size would have to decrease to fit into holes left by the bigger gluons. This way, more and more gluons of smaller and smaller sizes can be packed into the hadron. For a given hadron energy there is a characteristic saturation momentum Q_{sat} , corresponding to the inverse size of the smallest packed gluons [McLo8a]. Gluon modes with transverse momenta $p_T \leq Q_{\text{sat}}$ are therefore saturated [Gel+10]. This saturation momentum $Q_{\text{sat}}(x)$ grows with rising density when increasing the energy of the hadron or the number of contained nucleons [Kan19]. It is important to note, that saturation does not imply that the number of gluons stops growing. It means that for a given transverse momentum scale the rapid growth of gluons stops but continues for gluons of higher transverse momentum and, therefore, smaller sizes [McLo8b]. Figure 1.2b depicts this saturation behavior with the purple shaded area when probing small x and Q. This extreme phase space density

explains the word *condensate* to describe this theory.

While the CGC offers a promising approach to solving many open questions in heavyion physics, proposing a universal form of matter describing high-energy hadrons, its existence and properties are still controversial and require experimental investigation.

The parton distribution is however not only a function of the previously discussed Bjorken x, but also the momentum transfer Q. The evolution of PDFs at fixed Bjorken x and increasing Q is called the Bjorken limit and corresponds to the horizontal arrow in Figure 1.2b. This evolution of PDFs with the probed momentum scale is described by the so-called Dokshitzer-Gribov-Lipatov-Alterelli-Parisi (DGLAP) equations [AP77]. The momentum scale dependence in the DGLAP equation manifests in the form of dependence on the running coupling constant of QCD $\alpha_{\rm S}(Q^2)$, which will be briefly discussed in the following, leading to the phase diagram of QCD.

1.2.2 Phase Diagram of QCD

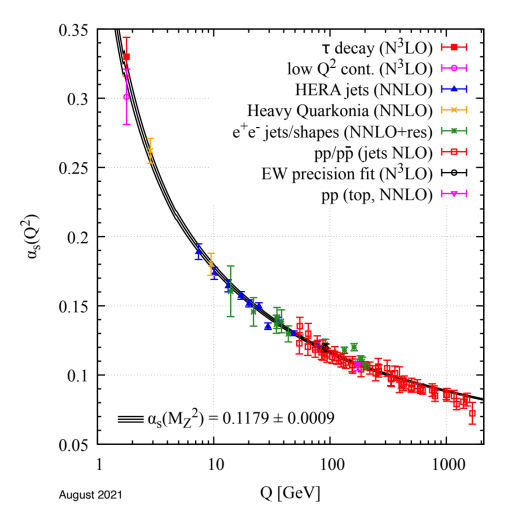
At the heart of QCD lies its coupling constant $\alpha_S(Q^2)$, which, unlike the name would suggest, exhibits a pronounced dependence on the probed momentum scale Q. A compilation of $\alpha_S(Q^2)$ measurements using various probes is shown in figure 1.3a.

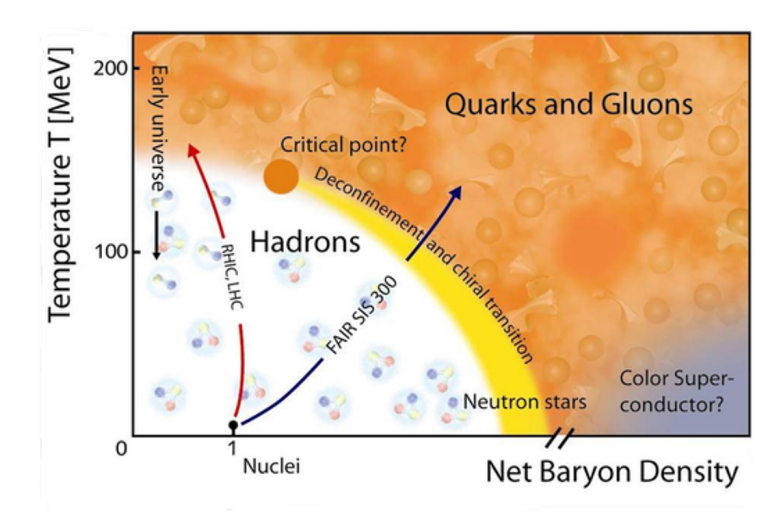
The Q dependence of the coupling constant can be approximated at leading order by the following equation [Bü21]:

$$\alpha_{\rm S}(Q^2) = \frac{\alpha_{\rm S}(Q_0^2)}{1 + B\alpha_{\rm S}(Q_0^2) \ln(Q^2/Q_0^2)},$$
(1.5)

where $\alpha_S(Q_0^2)$ is the coupling constant at a reference scale Q_0 and B is a theory dependent constant. As a probe's spatial resolution is inversely proportional to its momentum Q, the very large coupling constant at small Q can also be understood as strong coupling at large distances. This large coupling stems from the linear potential of QCD and leads to confinement, preventing free color charges.

Both the theoretical description by equation 1.5 as well as the measurements shown in figure 1.3a indicate a decreasing coupling strength when probing very large momentum scales Q. In a large multibody system, this weakening of the strong coupling is expected to cause deconfinement, where the quarks and gluons are not bound in hadrons anymore but instead traverse such a medium quasi-free. Such a state of deconfined quarks and gluons is called a Quark Gluon Plasma (QGP). Within a QGP, one also expects the restoration of chiral symmetry, whose breaking in vacuum is responsible for a large fraction of the mass of hadronic matter [DGH94]. Experimentally, the QGP was found to behave like a perfect fluid with negligible viscosity [Esk19].





- (a) Measurements of the QCD coupling constant $\alpha_S(Q^2)$ [Pdg22]
- (b) Phasediagram of QCD containing the hadronic and the QGP phase [Phi20]

Figure 1.3: The coupling constant α_S decreases with rising Q (left), which in case of a large many-body system can lead to deconfinement and consequently the QGP, that can be achieved at large temperature or net baryon density (right).

The necessary momentum scale for such a state of matter can be reached by reducing the distance of the quarks and gluons through increasing the net baryon density or the temperature. This motivates the construction of a phase diagram for strongly interacting matter representing the phase as a function of temperature and net baryon density. Figure 1.3b shows our current understanding of the phase diagram of strongly interacting matter. It depicts the separation of the hadronic phase at low temperatures and baryonic densities to the QGP phase at large temperatures and densities.

The transition between the two phases is believed to be a crossover at small baryon densities up to a critical point followed by a first-order phase transition at large net baryon densities. While the existence of a QGP at large energy density is established both in theory and experiments [Alib], the existence and precise location of a critical point within the phase transition remain active areas of research.

Nature is thought to provide two examples of environment with the necessary extreme properties for the formation of a QGP. According to our current scientific understanding, the Big Bang created immensely hot matter and antimatter in equal proportions, equivalent to a net baryon density of zero. The cooling of the QGP during the universe's first milliseconds is indicated by an arrow along the temperature axis in figure 1.3b. Moreover, a QGP is speculated to be present within neutron stars [AGK20] despite their moderate temperatures, due to their characteristically high baryonic densities, when the Fermi pressure of the neutrons is not strong enough to counter gravitation, leading to their wavefunctions to overlap. The phase diagram shown in figure 1.3b also illustrates how heavy-ion collisions, varying in energies and collision systems, aim to probe different

regions of the phase transition. For instance, measurements at the Large Hadron Collider LHC explore high temperatures at negligible baryon densities, similar to post-Big Bang conditions, while experiments at facilities like the Facility for Antiproton and Ion Research (FAIR) aim to investigate the QGP at large baryonic densities, similar to the conditions found in neutron stars.

Insights to the QGP and other QCD properties stem from the compilation of many different probes from various collision systems, where each collision system offers complementary information on a different aspect, as described in the following section.

1.3 INVESTIGATING QCD THROUGH PARTICLE COLLISIONS

In order to resolve the quarks and gluons within hadrons, collisions of highly energetic particles are used, as the resolution of a probe is proportional to its wavelength, which itself is inversely proportional to its energy. Our current understanding of Quantum Chromodynamics is therefore largely based on experimental evidence from analyzing the aftermath of particle collisions. This section describes the benefits of the three most commonly used collision systems at the LHC: Proton-Proton (pp), Proton-Lead (p-Pb), and Lead-Lead (Pb-Pb).

1.3.1 Proton-Proton Collisions

Protons in the LHC move with speeds very close to the speed of light, causing an extreme Lorentz time contraction for the partons within. Collisions of these highly energetic protons can, therefore, be described as individual collisions of partons, which are frozen in time [Hor21]. The production of particles in these collisions is commonly factorized into the different steps of such a collision to separate the different energy scales. The following equation describes this factorization for the example of the ω meson production cross section in pp collisions:

$$E\frac{d^{3}\sigma^{pp\to\omega X}}{d\vec{p}} = \sum_{a,b,c} PDF_{a} \otimes PDF_{b} \otimes d\sigma_{ab\to cX} \otimes FF_{c}^{\omega}, \tag{1.6}$$

where the left side represents the Lorentz invariant production cross-section of ω mesons, as measured in the analysis presented in this thesis. The right side of the equation consists of a sum of the contributions of the three components, which describes the distribution of the initial partons a and b, their collision, and the subsequent fragmentation of the produced parton c into the ω meson.

PDF The Parton Distribution Function (PDF), as introduced in section 1.2, describes the distribution of partons within nucleons as a function of x and Q and can be understood

as setting the initial conditions of a collision. The final particle production in equation 1.6 is a sum over the products of all pairings of partons a and b. Most data on PDFs comes from deep inelastic electron-nucleon scattering experiments as they involve only one PDF.

 $d\sigma$ The elementary partonic cross-section $d\sigma$ contains the probability with which the partons a and b scatter and produce particle c and some remainder X. As the relevant momentum scale of this primary collision is typically very large, this cross-section can be determined from perturbative QCD (pQCD) calculations.

The fragmentation of an intermediate parton c produced in the primary collision is quantified by the Fragmentation Function (FF). As these processes occur with small momentum transfers, they cannot be calculated from pQCD, and their description is largely based on experimental input.

Both PDFs and FFs can therefore be constrained through measurements of particle production, such as the ω meson, helping further our understanding of the different QCD processes involved. Additionally, measurements in pp collisions serve as reference for Pb-Pb and p-Pb collisions, as outlined in the next two sections.

1.3.2 Lead-Lead Collisions

The extreme energy density reached in Lead–Lead (Pb–Pb) collisions at the LHC is believed to lead to temperatures greater than a critical temperature $T_{\rm c} \approx 155\,{\rm MeV}$, necessary for the creation of a QGP [Baz+14].

At the LHC, matter and antimatter being produced in equal proportions far outweigh the incoming nucleons and therefore lead to minuscule net baryon density. The evolution of the QCD matter from nuclei to QGP in these high-energy Pb-Pb collisions is depicted in figure 1.3b with a red arrow. The produced QGP then cools off rapidly during its expansion, with an expected lifetime of only $10 \, fm/c$ [Alib].

Due to its short lifetime, the existence and properties of a possible QGP have to be investigated using information conveyed by the long-lived particles reaching the detectors. One of the most common probes of the QGP is its modification of the transverse momentum spectra of the particles produced in the collision. This modification is quantified using the nuclear modification factor R_{PbPb} :

$$R_{\text{PbPb}} = \frac{1}{T_{\text{PbPb}}} \frac{d^2 N_{\text{PbPb}} / dp_{\text{T}} dy}{d^2 \sigma_{\text{pp}} / dp_{\text{T}} dy},$$
(1.7)

where d^2N_{PbPb}/dp_Tdy denotes the p_T dependent number of produced particles of a given type in Pb-Pb collisions, normalized by the respective transverse momentum (dp_T) and rapidity (dy) interval. The corresponding denominator $d^2\sigma_{pp}/dp_Tdy$ contains the

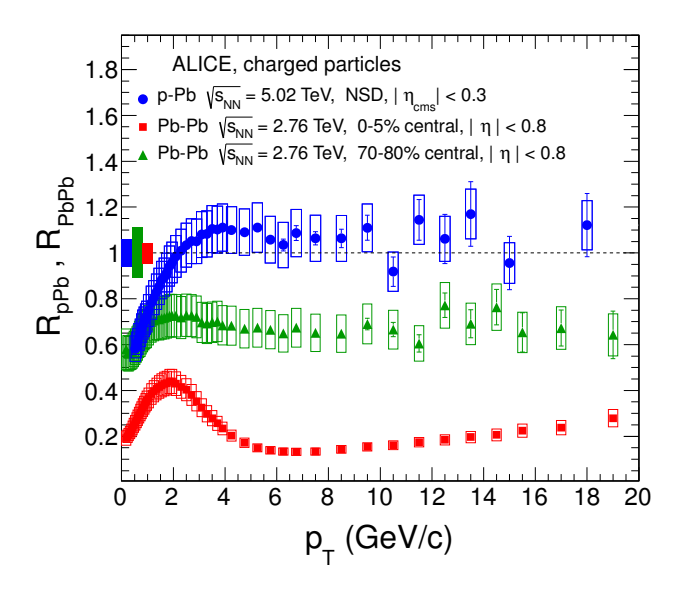


Figure 1.4: Measurements of the nuclear modification factors R_{PbPb} and R_{pPb} quantifying the modification of the charged particle production in Pb-Pb and p-Pb collisions compared to pp collisions [Abe+13]

production cross-section for the same particle in pp collisions, including the same normalizations. Assuming a Pb–Pb collision is a superposition of many binary pp collisions, the production ratio is normalized by the nuclear overlap function T_{PbPb} , quantifying the overlap between the two colliding nuclei.

The nuclear modification factor is often measured as a function of centrality, to observe the increase of QGP effects in more central collisions. Figure 1.4 shows measurements of the nuclear modification factor $R_{\rm PbPb}$ of charged particles for central Pb-Pb collisions in red and peripheral Pb-Pb collisions in green. In the absence of any nuclear modification, the $R_{\rm PbPb}$ would be equal to unity. The $R_{\rm PbPb}$ is however significantly below unity for both centralities, corresponding to a suppression of the measured particle production in Pb-Pb collisions. This suppression at large transverse momenta, which increases for more central collisions (red), is called jet quenching and can be explained by a QGP, which the particles have to traverse, losing energy in the process.

Pb–Pb collisions however do not only contain these so-called *final-state* effects caused by the QGP, but also some unrelated *initial-state* effects, caused by the nucleons being bound within nuclei. Therefore, the suppression seen in figure 1.4 alone cannot be directly attributed to the formation of a QGP. To isolate *final-state* effects of the QGP and disentangle them from the *initial-state*, one utilizes p–Pb collisions, where the energy density is believed not to be high enough for the formation of a QGP, allowing for an isolated study of the *initial-state* effects [Sal+11].

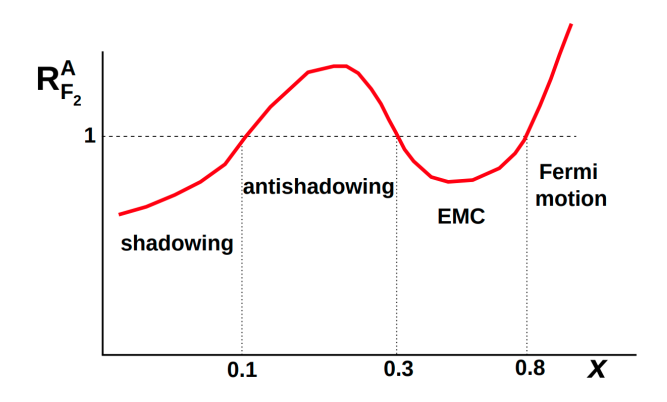


Figure 1.5: Schematic representation of the ratio $R_{F_2}^A(x, Q_0^2)$ of the structure function of a nucleus to that of a single nucleon given by equation 1.8, for a fixed Q^2 [Armo6]

1.3.3 Proton-Lead Collisions

Particle production in Proton–Lead (p–Pb) and Pb–Pb collisions can be modified by so-called Cold Nuclear Matter (CNM) effects. These describe modifications of the momentum distribution of partons contained in a nucleon, caused by their proximity to other nucleons. The term *cold* differentiates these effects caused by the surrounding *cold* nuclear matter, from those caused by the *hot* QGP predominantly present in Pb–Pb collisions. As the temperatures in p–Pb collisions are expected to stay below the critical temperature T_c necessary for the formation of a QGP, p–Pb collisions enable the investigation of CNM effects. The modification caused by CNM effects can be described using the ratio $R_{F_2}^A$ of the structure functions $F_2^{A/N}$ of nucleus A to that of a single nucleon, normalized by the number of nucleons in the nucleus A [Armo6]

$$R_{F_2}^{A}(x,Q^2) = \frac{1}{A} \frac{F_2^{A}(x,Q^2)}{F_2^{P}(x,Q^2)}.$$
 (1.8)

While the structure functions and, consequently, the ratio depend on both the momentum scale Q^2 and the relative momentum x, it is often discussed at fixed $Q = Q_0$, as schematically shown in figure 1.5. The modification caused by CNM effects seen in this figure can be split into four regions, based on the probed relative momentum, and whether the structure function shows an enhancement or a suppression in the respective region.

Beginning the discussion at small $x \lesssim 0.1$, one observes a suppression of the structure function in the nucleus, commonly described as nuclear **shadowing**. Interactions with nucleons in the center of the nucleus are often said to be *shielded* by the outer nucleons [Jon23]. Within the CGC model, this suppression is explained by the larger saturation momentum Q_{sat} , described in section 1.2.1 [McLo8a]. As this corresponds to a larger momentum region in which gluons are saturated in the nucleus, the structure function would be suppressed compared to a single nucleon.

When probing higher x one observes an increase of the ratio with an enhancement in the so-called **antishadowing** region at $0.1 \lesssim x \lesssim 0.3$. This region is usually discussed as compensating the preceding shadowing region by satisfying the sum rule for momentum [Armo6; Kla23].

Next comes the **EMC** effect in the region $0.3 \lesssim x \lesssim 0.8$, named after the European Muon Collaboration (EMC) that first observed this suppression in 1983 [Aub+83]. Today, 40 years after its discovery, different theoretical models try to explain the suppression; however, there is no consensus on any of the explanations [Wik; Noro3; Hen+17].

The final modification region present at large relative momentum $x \gtrsim 0.8$ shows again an enhancement of the structure function in the nucleus, caused by the **fermi motion** of the nucleons [Armo6].

While the particle production in high energy collisions is strongly influenced by these modifications of the structure function, the structure function cannot be measured directly in p-Pb collisions. Similar to Pb-Pb collisions, the nuclear modification in p-Pb collisions is therefore also commonly quantified using the nuclear modification factor

$$R_{\text{pPb}}(p_{\text{T}}) = \frac{1}{A_{\text{pPb}}} \frac{d^2 \sigma_{\text{pPb}} / dp_{\text{T}} dy}{d^2 \sigma_{\text{pp}} / dp_{\text{T}} dy},$$
(1.9)

with the $p_{\rm T}$ dependent production cross sections ${\rm d}^2\sigma/{\rm d}p_{\rm T}{\rm d}y$ in pp and p-Pb collisions and the normalization by the mass number $A_{\rm pPb}=208$. Deviations of $R_{\rm pPb}$ from unity can be interpreted as modifications of particle production due to CNM effects. In the late 70's, the so-called Cronin effect was discovered, where an enhanced particle production at $p_{\rm T}\approx 3 GeV$ was observed in proton-nucleus collisions. This effect is explained by multiple scatterings between the partons of the proton and the partons of the nucleus, as these scatterings result in a transverse momentum kick, increasing the momenta of the partons, hardening the $p_{\rm T}$ spectrum [BGVo4]. A measurement of the nuclear modification factor $R_{\rm pPb}$ of charged particles is shown in figure 1.4. In contrast to measurements at lower center of mass energies ($\sqrt{s_{\rm NN}}\approx 200\,{\rm GeV}$) [MPCo4], there is no significant Cronin effect visible at LHC energies. This disappearance of the Cronin effect is also described in the CGC theory [Alb12]. At large transverse momenta, the $R_{\rm pPb}$ in figure 1.4 is compatible with unity, while the red and green data points show a very clear discrepancy from unity, suggesting additional effects, likely by a QGP.

To bring together such measurements of the $R_{\rm pPb}$ ($p_{\rm T}$) (eq. 1.4 and the modification factor $R_{F_2}^{\rm A}(x)$ (eq. 1.5, one can use the approximate connection between x and $p_{\rm T}$, valid for vanishing rapidity [Bü21]

$$x = \frac{2p_{\rm T}}{\sqrt{s}}$$
, given $y = 0$. (1.10)

Using this equation, one can convert p_T regions of the R_{pPb} into x regions of the $R_{F_2}^A(x)$ and therefore correlate nuclear modifications observed in R_{pPb} measurements to the CNM effects depicted in figure 1.5.

1.4 MONTE CARLO EVENT GENERATORS

Analyses of particle production in collisions, such as the ones in the previous sections, require the use of MC event generators to quantify and correct detector effects like the spatial coverage and efficiency of the detector. Predictions of MC event generators can furthermore be compared to measurements in order to test their predictive power and the models used within. For the measurement of ω meson production presented in this thesis, three different MC event generators are utilized:

- PYTHIA 8.2 serves as a general purpose MC event generator, describing highenergy particle collisions by hard and soft interactions, parton distributions, parton showers, and hadronization based on the Lund string model [And+83]. Within the Monash 2013 tune, which is utilized in the pp simulation for this analysis, many free parameters are adjusted using parametrizations of available experimental data to best reproduce the properties of such collisions [Bie+22].
- DPMJET is a MC event generator based on the Dual-Parton-Modell (DPM) [RER01]. It uses pQCD to describe hard processes, while soft processes are described using Gribov's reggeon field theory [Gri67]. The hadronization within DPMJET is simulated according to the Lund model as implemented in PYTHIA [RER01]. DPMJET is implemented in this analysis for the simulation of the p-Pb collisions.
- EPOS¹ is a MC event generator that describes different hadronic interactions from cosmic ray showers to heavy ion collisions following a quantum mechanical multiple scattering approach based on partons and strings [PPW10]. The hadronization in EPOS is done through collective hadronization [Pie+15]. Simulations of pp and p-Pb collisions are used in this analysis to coherently test predictions in both collision systems. The employed tune, EPOS LHC, was introduced in 2012 and used first results from the LHC, tuning the model to describe these high-energy collisions of different sizes [Pie+15].

1.5 RELATED WORK

Since the conjecture of the ω meson in 1957 [Nam57] it has been measured in many different facilities around the world. While early works of the 60s and 70s focused on its properties like mass and width [Kra+64; Gel+63], first measurements of its production cross section came in the 80s at Fermilab [Don+80] and the ISR²[Bre+89]. A compilation of cross-section measurements relevant to the analysis presented in this thesis is given in table 1.2. Jumping forward by 30 years of measurements and advances in accelerator

¹ Energy conserving quantum mechanical approach, based on Partons, parton ladders, strings, Off-shell remnants, and Splitting of parton ladders

² Intersecting Storage Rings (ISR) at CERN

| Meson | $\sqrt{s_{\rm NN}}$ (TeV) | System | $p_{\rm T}~({\rm GeV}/c^2)$ | | Reference | |
|----------|---------------------------|--------|-----------------------------|---|-----------|-----------|
| | 0.015 | р-Ве | > 2.2 | | | [Don+8o] |
| | 0.062 | pp | > 3 | | | [Bre+89] |
| ω | 0.2 | pp | 0 | - | 13.5 | [Ada+11a] |
| ω | 0.2 | d-Au | 0 | - | 13.5 | [Ada+11b] |
| | 7 | pp | 2 | - | 17 | [Ach+20] |
| | 13 | pp | 1.6 | - | 50 | [Lü23] |
| π^0 | 5.02 | pp | 0.4 | - | 30 | [Sas19] |
| /ί | 5.02 | p–Pb | 0.3 | - | 20 | [Ach+18b] |

Table 1.2: Compilation of previous ω and π^0 measurements relevant to the results of this thesis

and detector development, the PHENIX³ collaboration measured the ω meson at $\sqrt{s_{\text{NN}}}$ = 200 GeV in a large variety of collision systems [Ada+11b].

The ALICE collaboration to this date published one measurement of the ω meson production at $\sqrt{s}=7\,\text{TeV}$ [Ach+20], and has conducted another, currently *preliminary*, pp analysis at $\sqrt{s}=13\,\text{TeV}$ [Lü23]. In contrast to only two ω meson analyses, the π^0 and η have been measured at all available LHC energies [Abe+12; Ach+17; Koc11; Ach+18c] and collision systems [Ach+22; Ach+18b; Abe+14b]. This expertise in π^0 reconstruction within the collaboration facilitates precise ω meson measurements using the three-pion decay channel. The two π^0 analyses at $\sqrt{s_{\text{NN}}}=5.02\,\text{TeV}$ in pp and p-Pb collisions are furthermore used as references for the calculation of the ω/π^0 ratio [Sas19; Ach+18b].

Recently, both experimental and theoretical physicists have expressed their interest in precise ω meson measurements:

While direct photons are one of the most promising QGP observables, their measurement requires a precise description of the decay photon background, to which the ω meson is the third largest contributor [Ada+16]. Precise ω meson measurements, therefore, also indirectly help to reduce the uncertainties on our knowledge of QGP properties, like its temperature.

Theoretical physicists aim to describe the ω meson fragmentation through the use of FF's, as described in section 1.3.1 [Ma+19]. As these involve soft QCD processes and are therefore dependent on experimental constraints, the limited data was commented in one publication as "No such considerable interest has been shown towards vector meson production due to the scarcity of the data available so far" [SI17].

This considerable interest from both the theoretical and the experimental side, combined with the lack of high energy ω meson measurements, motivate their analysis as presented in this thesis, offering first constraints on the production and modification of ω mesons in

³ Pioneering High Energy Nuclear Interaction eXperiment (PHENIX)

p–Pb collisions. The measurement is performed at $\sqrt{s_{\text{NN}}} = 5.02 \,\text{TeV}$, as this is the highest energy ever recorded in all collision systems (pp, p–Pb and Pb–Pb).

First studies on the background and signal extraction of the ω meson have already been conducted in the author's bachelor's thesis [Str21], from which certain portions have been referenced for the background description employed in this analysis.

EXPERIMENT

The analysis presented in this thesis builds upon remarkable achievements of engineering, namely the accelerators and detectors available at the European Organization for Nuclear Research (CERN¹). Since its foundation in 1954, the variety of accelerators spanning both sides of the French-Swiss border near Geneva enabled many scientific breakthroughs in particle physics: From the verification of V–A coupling in 1962 [Fid15], to the discovery of the W and Z bosons in 1983 [DLR15], to the completion of the standard model by the Higgs boson in 2012 [Atl]. The latter was produced at the largest and most powerful of CERN's accelerators, the Large Hadron Collider (LHC), which also provides collisions to the ALICE experiment, supplying the data on which the herein-presented analysis is based.

This chapter provides a description of the particle acceleration followed by an outline of the ALICE experiment and its sub-detectors that are relevant to the measurement of ω mesons presented in this thesis.

2.1 PARTICLE ACCELERATION AT CERN

The Large Hadron Collider (LHC) at CERN accelerates protons and ions to the highest energies worldwide, allowing the four large experiments to examine their collisions and investigate the underlying laws of QCD, as described in section 1.3. However, the LHC is only the last piece of a larger accelerator chain, as depicted in figure 2.1. The following paragraphs outline the pre-acceleration of protons and ions before their injection into the LHC, involving a total of six accelerators, going from Linear Accelerators (LINACs) to circular accelerators of increasing size.

Hydrogen atoms are taken from a gas bottle and stripped of their electrons in a duo-plasmatron [Hon79]. The resulting protons are then accelerated in CERN's 80 meter long LINAC 2 up to $E_{\rm kin} = 50\,{\rm MeV}$ [Bol+79], before being injected into the Proton Synchrotron Booster (PSB). The PSB consists of four superimposed rings with a circumference of 157 m that accelerate the protons up to $E_{\rm kin} = 1.4\,{\rm GeV}$ [Rei69] before injecting them into the Proton Synchrotron (PS).

The lead ions, on the other hand, are evaporated off of a solid strip within the so-called Electron Cyclotron Resonance Ion Source (ECRIS) and then injected into the 8 m long LINAC 3 [Ang+93]. During the acceleration process, the lead ions get successively stripped off all of their electrons to maximize the charge-to-mass ratio and, therefore, allow for

¹ Conseil Européen pour la Recherche Nucléaire (CERN)

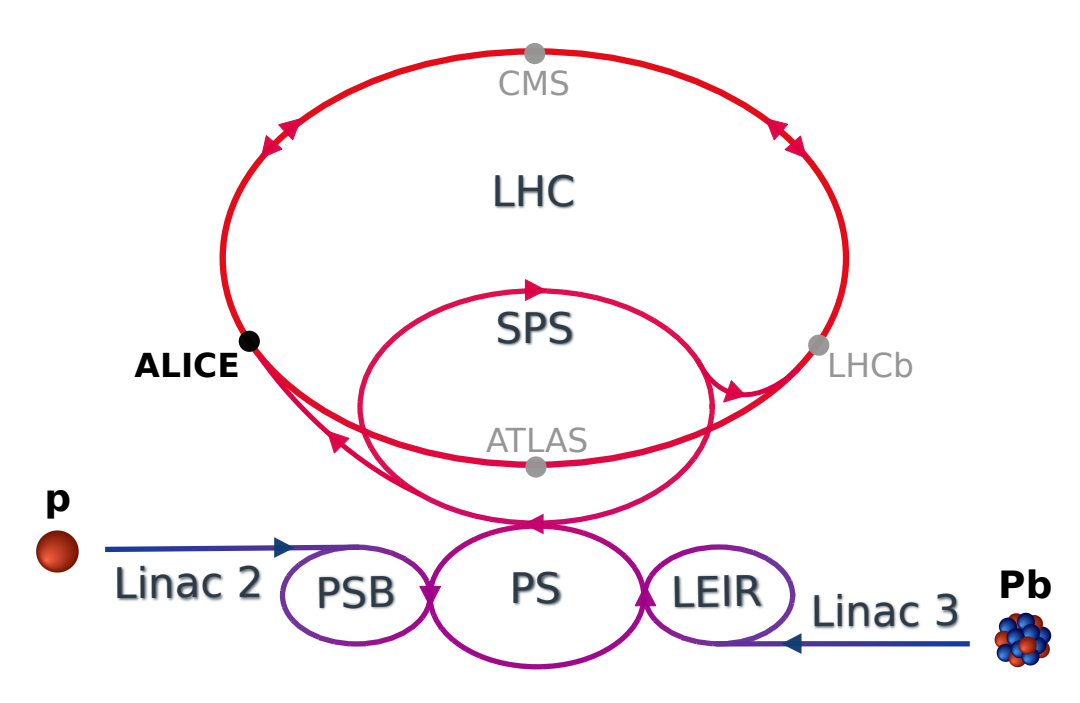


Figure 2.1: Schematic drawing of the accelerator chain with which protons and ions are accelerated at CERN, culminating in the LHC and the four connected experiments

maximum acceleration. From here, they are fed into the Low Energy Ion Ring (LEIR) (80 m in circumference), in which the ions are both cooled and accelerated up to $E_{\rm kin} = 72.2 \, {\rm MeV}$ per nucleon before being injected into the PS.

Once the protons or ions are injected into the PS from the PSB and LEIR respectively, they follow the same acceleration chain. Within the 628 m circumference of the PS, the protons (lead ions) are accelerated up to $E_{\rm kin} = 25\,{\rm GeV}$ (5 GeV per nucleon) [Reg62]. From the PS, the protons and ions are passed on to the Super Proton Synchrotron (SPS) with a circumference of 6.9 km, in which the protons (ions) up to $E_{\rm kin} = 450\,{\rm GeV}$ (176.4 GeV per nucleon), before they are finally injected into the LHC.

The LARGE HADRON COLLIDER The LHC consists of two parallel beam pipes, in which particles are accelerated close to the speed of light, in opposite directions along its 26.7 km circumference. Unlike the name suggests, the LHC not only accelerates protons but also heavier nuclei like lead ions (208 Pb). Using magnetic fields of up to 8.33 T, the LHC can accelerate protons (lead ions) up to $E_{\rm kin}=7\,{\rm TeV}$ (2.76 TeV per nucleon), making it not only the largest but also the most powerful accelerator on earth [Bru+o4]. The particles are kept in the ring by 1232 superconducting dipole magnets, each 15 meters long and weighing around 35 tonnes [Bru+o4]. At four so-called interaction points, the two beam lines intersect, where the particles of the two beams can be brought to collisions, which are recorded by four large experiments built around these interaction points.

The two experiments ATLAS² and CMS³ are multipurpose detectors designed to measure highly energetic final state particles and thereby test the standard model of elementary particle physics and search for possible physics beyond the standard model. Their greatest success to date lies in the detection of the Higgs boson in 2012. The LHCb⁴ experiment, on the other hand, studies CP violation via decays of B mesons. Unlike ATLAS and CMS, LHCb is not centered around the collision vertex but instead, the detectors are placed in the forward direction with a focus on good reconstruction of secondary vertices from B meson decays. As the only one of the four experiments at the LHC, the ALICE⁵ experiment was initially designed to study heavy-ion collisions. Since data from this experiment form the basis for the measurement of ω mesons in this work, the ALICE experiment together with the detectors relevant to the analysis, will be described in more detail in the following section.

2.2 A LARGE ION COLLIDER EXPERIMENT

Located 50 meters underneath the French village of *Saint-Genis-Pouilly* lies the ALICE experiment. A schematic layout of the 16 meter tall ALICE experiment, including all of its subdetectors, is shown in figure 2.2.

As the name suggests, ALICE primarily investigates heavy-ion collisions to study the properties of both hot and cold partonic matter in extreme conditions, as introduced in section 1.2. To measure probes of such heavy-ion collisions, the detectors of the ALICE experiment are designed to provide good Particle Identification (PID) and resolution down to low transverse momenta and up to high particle multiplicities created in heavy-ion collisions.

The large red solenoid L3 magnet has an inner radius of 5.9 m at a length of 12 m and provides a magnetic field of 0.5 T within, where the so-called *central-barrel* detectors utilize the induced curvatures of particle tracks to determine their momenta [Gli+19]. ALICE's *central-barrel* is supplemented in the forward direction by the so-called *muon-arm*, shown on the right hand side in figure 2.2. This muon spectrometer allows for the investigation of quarkonia and heavy flavor particles via their muon decays in the forward region [Bal15].

The ALICE experiment started taking data in 2010 until 2013, when the LHC went into a long shutdown, during which the ALICE experiment was upgraded, leading to the detector-setup shown in figure 2.2, which was available for the second operational run of the LHC starting in 2015. The analysis presented in this thesis reconstructs the ω meson using this setup via its decay into three pions and the subsequent decay of the neutral

² A Toroidal LHC ApparatuS (ATLAS)

³ Compact Muon Solenoid (CMS)

⁴ LHC beauty (LHCb)

⁵ A Large Ion Collider Experiment (ALICE)

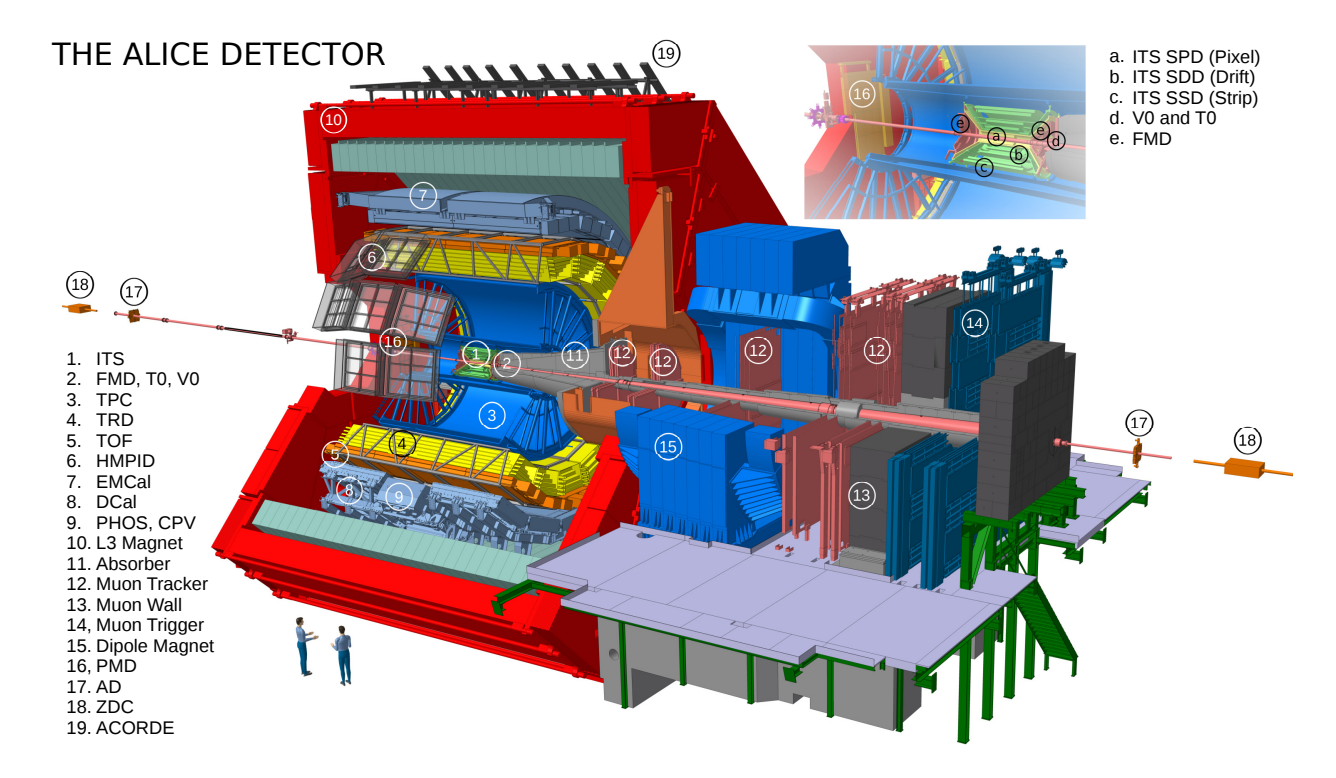


Figure 2.2: Schematics of the ALICE experiment for the second run of the LHC [Alib]

pion into two photons ($\omega \to \pi^+\pi^-\pi^0 \to \pi^+\pi^-\gamma\gamma$). This analysis, therefore, makes use of a number of ALICE's subdetectors for PID and momentum measurement of both charged and neutral particles, which are introduced in the following sections going from the inside to the outside of the experiment.

2.2.1 Inner Tracking System (ITS)

The Inner Tracking System (ITS) consists of six cylindrical layers around the beam pipe, covering the full azimuth angle and a pseudorapidity range of $|\eta| < 0.9$ [ALI99].

At a radial distance of 3.9 and 7.6 cm from the interaction point are the two innermost layers, which are made up of silicon pixels and are therefore referred to as Silicon Pixel Detector (SPD). As the particle density in the innermost layers can reach up to 50 particles per cm², the SPD has a very high granularity of $50 \times 425 \mu m$ per cell. Because of the SPD's close proximity to the interaction point, its signals are used to locate the collision vertex and to provide the innermost points for the tracking of charged particles [Aam+o8].

Going outward, the two intermediate layers form the so-called Silicon Drift Detector (SDD). As this drift detector comes with comparatively large busy times, reducing the number of available events, it is disregarded for the analysis presented herein.

The two outermost layers of the ITS make up the Silicon Strip Detector (SSD), where the particle density is expected to be below one particle per cm². Therefore, the granularity in these layers is not as high to reduce the used material and therefore, reduce multiple

scatterings while still providing crucial localization of charged particles, with a special focus on matching their tracks to the next tracking detector, the TPC [Aam+08].

2.2.2 *Forward Trigger Detectors* (V0 and T0)

Disks surrounding the beam pipe in either direction along the beam axis contain the two trigger detectors V0 and T0, used in the herein presented analysis and shown in figure 2.2 in red labeled as 2*d*.

VO DETECTOR Two scintillation counters V0A and V0C together form the V0 detector, covering the full azimuth angle for $2.8 < \eta < 5.1$ as well as $-3.7 < \eta < -1.7$ [Abb+13]. In heavy-ion collisions, the V0 detector is commonly used to estimate the centrality of an event, while in pp and p-Pb collisions, the total charge in the V0 detector is used as a Minimum Bias (MB) trigger for the other ALICE detectors. For the datasets investigated in this analysis, a coincident signal above a given threshold in V0A and V0C is required to trigger the readout of an event.

TO DETECTOR Like the V0 detector, the T0 detector comprises two subdetectors, T0A and T0C. Each subdetector consists of an array of 12 Cherenkov radiators, which are optically coupled to photo–multiplier tubes. While the T0 also covers the full azimuth angle, compared to the V0, the T0 has a reduced pseudorapidity coverage of only $4.5 < \eta < 5.0$ as well as $-3.3 < \eta < -2.9$. With a timing resolution of around 50 ps, the T0 detector allows for an accurate collision time determination, which is then used by other detectors, such as the Time Of Flight (TOF) detector [Bon+o5].

2.2.3 Time Projection Chamber (TPC)

The Time Projection Chamber (TPC) is ALICE's main tracking detector, providing momentum measurement through their curvature by the magnetic field, as well as PID via their specific energy loss within the detector. Figure 2.2 shows the blue TPC barrel surrounding the ITS in green, which itself contains the beam pipe.

With a length and outer diameter of 5 meters each, the TPC covers a pseudorapidity range of $|\eta| < 0.9$ with full azimuth coverage. It consists of a gas-filled cylindrical field cage with an electric field of $4000\,\mathrm{V/cm}$ along the beam axis from the central electrode to the endcaps in either direction. When charged particles traverse the TPC, they ionize gas atoms along the way, leaving a trail of positively charged ions and free electrons. While the electric field draws the positively charged ions toward the central electrode, the electrons, with their much smaller mass, quickly move toward the endcaps. After a maximum drift time of 92 μ s, the freed electrons reach the endcaps, which house the readout of the TPC. The electron charge is then multiplied using Multi Wire Proportional

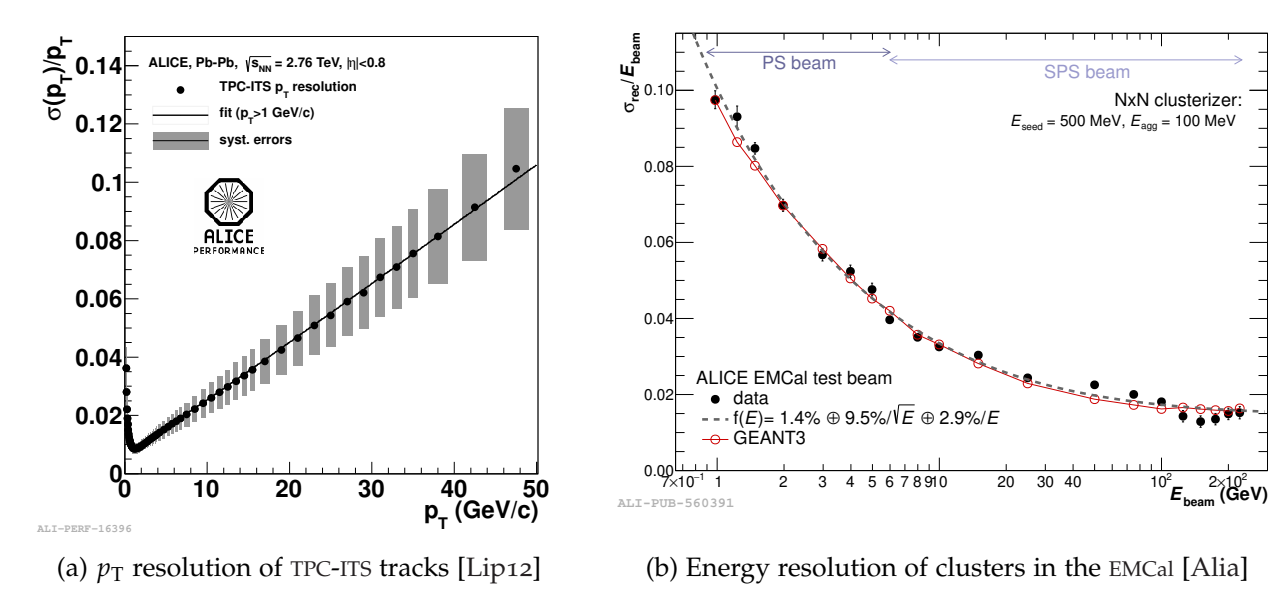


Figure 2.3: Relative resolution of reconstructed tracks and clusters

Chambers (MWPCs) before the signals are read out using cathode pads [Alm+10]. The combination of the location and time of this electron impact allows the reconstruction of the three-dimensional distribution of clusters left by the ionizing particle.

The individual clusters from the TPC and the ITS are combined to form so-called global tracks. The curvature of these tracks is then used to calculate the momentum of the ionizing particle. The relative transverse momentum resolution via these TPC-ITS tracks is shown in figure 2.3a. A remarkable resolution of about 1% can be observed for $p_{\rm T} \approx 2~{\rm GeV}/c$. At the same time, the resolution decreases for very low and high transverse momenta because, at low $p_{\rm T}$, the particles don't travel far enough into the TPC volume, and at high $p_{\rm T}$, their curvature gets too small.

In addition to their momentum, the TPC can also help to identify charged particles based on their specific energy loss per path length dE/dx. This identification is also employed in the selection of charged pions as outlined in section 4.1. The PID of the TPC in this analysis is further enhanced using the TOF detector, as introduced in the following section.

2.2.4 Time Of Flight (TOF) Detector

At a distance of about 3.7 m from the beam axis, the Time Of Flight (TOF) detector, shown in figure 2.2 in orange, covers the full azimuth region of $|\eta|$ < 0.9 with a cylindrical array of approximately 141 m² [Car19]. The array consists of 1593 Multigap Resistive Plate Chamber (MRPC) strips, which, in combination with the collision time given by the T0 detector, measure the time of flight of charged particles with a precision of 56 ps [Del+oo]. From there, the velocity β is calculated and matched to the momentum of

the corresponding TPC-ITS track to calculate the mass and identify the particle. This complementary PID method is used to enhance the purity of the selection of charged pions, especially in the intermediate momentum region, as discussed in section 4.1.

Charged particles can be accurately measured and identified using ITS, TPC, and TOF. Neutral particles, such as photons, however, do not ionize the TPC gas and can, therefore, not be tracked the same way. To reconstruct such neutral particles, ALICE offers two electromagnetic calorimeters located just behind the TOF. One of these two is the so-called Photon Spectrometer (PHOS) [Man+99], which is a highly granular lead-tungstate calorimeter, resulting in good energy resolution down to low $p_{\rm T}$. Unfortunately, this high granularity comes with a very limited acceptance of $|\eta| < 0.125$ in pseudorapidity and 70° in azimuth. Following exploratory studies showing a lack of statistics when using the PHOS for the ω reconstruction, only the other electromagnetic calorimeter, the EMCal, was further pursued for the direct measurement of photons.

2.2.5 Electromagnetic Calorimeter (EMCal)

At a distance of 4.4 meters from the beam axis lies the Electromagnetic Calorimeter (EMCal), which is designed to measure electromagnetic observables such as photons and electrons within the acceptance of $80^{\circ} < \phi < 187^{\circ}$ and $|\eta| < 0.7$ [Cor+o8]. During the LHC shutdown between 2013 and 2015, the EMCal was extended by the so-called Di-Jet Calorimeter (DCal) on the opposite side in azimuth, covering $261^{\circ} < \phi < 319^{\circ}$, with a recess in the center, where the PHOS is located. As the EMCal and DCal are identical in detector design, they are used together in this work, and their combination will in the following be simply referred to as EMCal. The EMCal is a sampling calorimeter with alternating layers of lead and scintillation material segmented into 6×6 cm cells. When an incident particle reaches the EMCal, it forms an electromagnetic cascade, which converts the energy of the incident particle into that of low-energy photons in the scintillation layers, which are then read out using photo-multipliers [Cor+08]. Signals from neighboring cells are then clustered together into clusters, which can be interpreted as a measured electromagnetic particle. Figure 2.3b shows the relative energy resolution of the EMCal for different energies of the incoming particle. While the resolution saturates at around 2% for very large p_T , the resolution decreases rapidly when measuring lower p_T particles. For incoming particles with an energy of $E \approx 2$ GeV, the relative resolution is already around 7 %. The minimum cluster energy for calibrated photon measurements was found to be around $E_{\min} = 0.7$ GeV [Alia].

2.3 ANALYSIS FRAMEWORK

In addition to the detector hardware described in the previous section, the analysis presented in this thesis also heavily builds upon different analysis frameworks, as outlined in the following. Data recorded by the ALICE experiment is distributed across a network of 174 data centers around the world [Bir11]. The code underlying the analysis presented in this thesis is a subset of the publicly accessible analysis frameworks *AliRoot*⁶ and *AliPhysics*⁷, maintained by the ALICE collaboration. The subsequent post-processing is largely inspired by the existing so-called *Afterburner*⁸ framework, developed by the ALICE photon conversion group. While the herein presented analysis profits strongly from the existing frameworks, a number of changes and additions have also been made to these frameworks, which are now being used for other analyses.

⁶ https://github.com/alisw/AliRoot

⁷ https://github.com/alisw/AliPhysics

⁸ https://gitlab.cern.ch/alice-pcg/AnalysisSoftware

DATASETS AND EVENT SELECTION

The analysis presented in this thesis covers the production of ω mesons in pp and p-Pb collisions at a center of mass energy of $\sqrt{s_{\rm NN}}=5.02$ TeV, which is the largest center of mass energy with measurements in the three collision systems (pp, p-Pb, Pb-Pb). This analysis uses all available datasets of pp and p-Pb collisions from the second run of the LHC at this energy. Data recorded by the ALICE experiment is cataloged in so-called periods, during which the collision system, energy, and the utilized trigger are not changed.

In November 2015 and 2017, ALICE recorded the periods LHC15n, LHC17p, and LHC17q, which contain pp collisions at $\sqrt{s}=5.02$ TeV. Between these pp periods, in late November 2016, ALICE recorded four periods of p-Pb data, two of which (LHC16q and LHC16t) were recorded at $\sqrt{s_{\rm NN}}=5.02$ TeV. ALICE further divides these periods into so-called runs, which describe a time span of continuous data taking with steady detector status, usually containing a few hours of recorded collisions. The quality of these runs, based on the performance of the different detectors, is then individually assured in a centralized Quality Assurance (QA) effort. These checks and calibrations were already performed before this analysis, as both the pp and the p-Pb dataset have previously been investigated among preliminary π^0 analyses [SS19; BSS21]. The list of runs contained in these datasets that passed the centralized QA and were therefore used in this analysis can be found in section A.1 of the appendix.

For the ω reconstruction using the so-called Photon Conversion Method (PCM) method, as described in section 4.2, the tracking detectors (ITS and TPC) as well as the trigger are required to have been in good condition. This requirement is extended to include the EMCal, when using it for the reconstruction of the decay photons, such as in the EMCal or PCM-EMCal π^0 reconstruction methods, outlined in section 4.3. This additional detector requirement results in minor differences between the included runs and, therefore available number of events for the different reconstruction methods. As the Silicon Drift Detector (SDD) layers of the ITS are not available for a large fraction of the recorded events due to their drift time [Kha2o], only the SPD and SSD layers of the ITS are utilized in this analysis. Even when the SDD was active for a given event, its signals are excluded in the tracking to ensure a consistent detector response while optimizing the efficiency of the analysis.

The analysis presented in this thesis considers only collisions that were triggered by the V0AND MB trigger, which requires coincident signals above a given threshold in both V0 detectors, in an effort to record Non Single Diffractive (NSD) events while introducing as little bias as possible, as the name suggests. For an event to be included in this analysis, they furthermore have to fulfill the following three criteria:

- 1. Events must include exactly one reconstructed primary vertex in the SPD. By excluding all events, in which more than one vertex was reconstructed, the background from pile-up events can be reduced.
- 2. A minimum number of SPD tracklets in relation to the number of SPD clusters is required in each event, as described by the following equation:

$$N_{\text{tracklets}} > \frac{N_{\text{clusters}} - 65}{4}.$$
 (3.1)

This is done to further reduce the contamination by background events, as a large number of clusters without tracklets indicate that the event does not correspond to a real collision and should, therefore, not be included in the analysis.

3. The collision's primary vertex must be less than 10 cm away from the collision point in the beam direction. Additionally, a small fraction of the events, around 1%, is excluded from the analysis as no vertex could be reconstructed in these events. The total number of events used for the normalization ($N_{\text{Norm, evt}}$) has to account for the number of events without a vertex ($N_{\text{no vtx}}$). This is done by assuming that the fraction of events within $|z_{\text{vtx}}| > 10 \, \text{cm}$ in events without a reconstructable vertex is the same as in events where the vertex can be reconstructed:

$$N_{\text{evt}} = N_{|z_{\text{vtx}}| < 10 \text{ cm}} + \frac{N_{|z_{\text{vtx}}| < 10 \text{ cm}}}{N_{|z_{\text{vtx}}| < 10 \text{ cm}} + N_{|z_{\text{vtx}}| > 10 \text{ cm}}} N_{\text{no vtx}}$$
(3.2)

The remaining number of available events for the analysis after this event selection is listed in table 3.1 for the different datasets and reconstruction methods. Table 3.1 furthermore lists the corresponding integrated luminosity $\mathcal{L} = N_{\rm evt.}/\sigma_{\rm MB}$ which was inspected. The visible MB trigger cross-section $\sigma_{\rm MB}$ was measured via van der Meer scans [Mee68] in both collision systems [Abe+14a; Ach+18a].

High-energy physics analyses rely on Monte-Carlo (MC) simulations, mimicking the production of particles and the detector response, to correct the raw spectra extracted in data for efficiency and acceptance losses. These effects are quantified by the ratio of ω mesons generated in the MC to the number of ω mesons that are reconstructed in the MC. Already in the step of the event selection, it has to be ensured that ω mesons, produced in collisions not triggered by the MB trigger, are included in the number of generated ω mesons. This way, the very high, but not perfect, trigger efficiency of the V0AND trigger is being accounted for. To quantify these effects coming from both the detector response but also the analysis procedure, the analysis steps presented in the following sections are applied analogously to the recorded data and the MC simulated data so that the spectra can be corrected as described in section 6.1.

| System | | Dataset | Method | $N_{ m evt}$ (×10 ⁶) | $\mathcal{L}_{\mathrm{int}}$ (n b^{-1}) |
|--------|------|--------------------------------|--------------|----------------------------------|--|
| | Data | LHC15n | PCM | 83 | 1.63 |
| | | | PCM-EMCal | 83 | 1.63 |
| | | | EMCal | 83 | 1.63 |
| | Data | LHC17pq | PCM | 861 | 16.93 |
| | | | PCM-EMCal | 787 | 15.47 |
| nn | | | EMCal | 787 | 15.47 |
| pp | MC | PYTHIA: LHC17e2 LHC18j3 | PCM | 86 | - |
| | | | PCM-EMCal | 84 | - |
| | | | EMCal | 87 | - |
| | MC | PYTHIA: LHC17l3b LHC18j2 | PCM | 844 | - |
| | | | PCM-EMCal | 707 | - |
| | | | EMCal | 768 | - |
| | Data | LHC16qt | PCM | 568 | 0.27 |
| | | | PCM-EMCal | 500 | 0.24 |
| n Dh | | | EMCal | 500 | 0.24 |
| p–Pb | MC | DPMJET: LHC18f3 | PCM | 573 | - |
| | | | PCM-EMCal | 509 | - |
| | | | EMCal | 524 | |
| | | | | | |

Table 3.1: Compilation of the datasets and MC simulations used in this analysis as well as the respective number N_{evt} of analyzed events following the definition in equation 3.2

The ALICE collaboration centrally simulated MC datasets with similar numbers of events for each of the analyzed datasets using the MC event generators introduced in section 1.4. For the simulation of pp collisions, the PYTHIA 8.2 MC event generator was used with the Monash 2013 tune for the production of the periods LHC17e2/18j3 anchored to LHC15n and the periods LHC17l3b/18j2, which are anchored to LHC17pq. The p-Pb collisions were simulated with the DPMJET MC event generator, leading to the production LHC18f3. The events generated by PYTHIA and DPMJET are coupled with the GEANT 3 [Bru+87] software package, which simulates the interactions of the particles with the detector.

To reduce systematic uncertainties on the nuclear modification factor, the analysis steps presented in the following sections are performed coherently for the pp and the p-Pb data, including all presented selection criteria. This is possible, as many observables used for these selections are approximately independent of the collision system. In the following, distributions of these observables are shown as found in p-Pb collisions; the corresponding distributions in pp collisions are listed in section A.3 of the appendix.

PION RECONSTRUCTION

As the ω meson is an unstable particle with a lifetime of $\tau = 7.7 \times 10^{-23}\,\mathrm{s}$ [Pdg22], it decays within the collision vertex, and therefore, its production can only be measured by reconstructing it from its decay products. The large branching ratio of the ω meson into three pions ($\mathcal{B}(\omega \to \pi^+\pi^-\pi^0) = 89.2\,\%$ [Pdg22]) motivates its reconstruction via these three pions. Before the ω mesons can be reconstructed, as described in chapter 5, the momenta and energy of the three decay pions have to be measured.

This chapter explains the reconstruction of these decay pions with the first section 4.1 describing the direct measurement and identification of the charged pions. Neutral pions, on the other hand, are unstable and almost instantly decay into two photons with a branching ratio of $\mathcal{B}(\pi^0 \to \gamma \gamma) = 98.8 \%$ [Pdg22]. This necessitates the measurement of the two decay photons as described in section 4.2. These decay photons are then combined to form π^0 candidates (section 4.3) before they are combined with the charged pions to form ω candidates in chapter 5.

4.1 CHARGED PION RECONSTRUCTION

Momenta of charged particles, like the π^\pm , can be measured from their curved tracks in the TPC and the ITS. The track selection is based on the *global constrained hybrid track* sample, as defined in [Tra]. These tracks were furthermore required to have a transverse momentum of at least $p_T > 100\,\mathrm{MeV}$, contain at least one hit in the SPD, and involve at least 80 clusters within the TPC, to ensure a good track quality. To select charged particles coming from the primary collision and not weak decays, the maximum Distance of Closest Approach (DCA) to the collision vertex of the tracks was set to 3.2 cm in the transverse x and y direction, and 2.4 cm in the z direction. These relatively large margins were chosen to optimize the efficiency of the analysis by including all pions that come from within the vertex within the finite vertex resolution of ALICE. Following these track requirements, compiled in table 4.1, signals from the TPC and TOF detector were used for the identification of pions within the tracks.

The energy loss per unit length of charged particles within the TPC volume is characteristic for each particle species and can be used for PID. Figure 4.1a shows the distribution of momentum-dependent energy loss of all charged particles in the p-Pb dataset. Accumulations along bands corresponding to the different particle species are observed. These bands are parameterized with splines (combinations of polynomials) based on the Bethe Bloch equation for a particle's energy loss within a medium, as shown with labeled lines

| Quantity | Setting |
|----------------------|---|
| ITS clusters | ≥ 1 hit in SPD |
| TPC clusters | min 80 clusters |
| $p_{ m T}$ | $p_{\mathrm{T}} > 100\mathrm{MeV}$ |
| DCA | $DCA_{xy} < 3.2 cm \& DCA_z < 2.4 cm$ |
| TPC PID | $n\sigma^{\pi} < 3$ |
| TOF (when available) | $n\sigma^{\pi} < 5 \text{ or } n\sigma^{K/p} > 3$ |

Table 4.1: Selection criteria applied to the ITS-TPC tracks to select charged pions

in figure 4.1a. The identification of pions is then performed based on the deviation of the measured energy loss to the expected energy loss in terms of the detector resolution $\sigma(\langle dE/dx \rangle)$:

$$n\sigma^{\pi} = \frac{\langle dE/dx \rangle^{\text{measured}} - \langle dE/dx \rangle^{\pi - \text{spline}}}{\sigma(\langle dE/dx \rangle)}.$$
 (4.1)

Using the energy loss in the TPC, charged tracks within three σ of the pion spline were selected as candidates for ω decay pions.

While this selection has high discriminatory power in the low transverse momentum region around $p \approx 400$ MeV/c, the kaon and proton splines cross the pion spline at $p \approx 1$ GeV/c and $p \approx 1.5$ GeV/c respectively, as depicted in figure 4.1a.

To compensate for this reduction in discriminatory power of the TPC dE/dx, the time signal provided by the TOF detector is utilized to improve the pion identification in this momentum regime. Figure 4.1b shows the measured velocity β measured by the TOF and the momentum p extracted from the corresponding track for all charged particle hits in the TOF. Similar to the TPC PID via the particle's energy loss, the momentum-dependent velocity shows bands according to the mass of the different particle species. The relation between momentum p and velocity β is connected via a particle's invariant mass $m_{\rm inv}$, as described by the following equation.

$$p = mv = \frac{m_{\text{inv}}}{\sqrt{1 - \beta^2}} \beta c \Rightarrow \beta = \left(\frac{m_{\text{inv}}c}{p} + 1\right)^{-1/2}$$
(4.2)

These calculated velocities for different particle species, depicted in figure 4.1b as black lines, show good agreement with the measured accumulations. While similar to the TPC dE/dx, the pion band merges with the kaon and the proton band at higher momentum, however, at slightly higher momentum than for the dE/dx at $p \approx 2$ GeV/c for the kaons and $p \approx 3.5$ GeV/c for the protons. As this corresponds to twice the momentum, at which the bands in the TPC dE/dx merged, the TOF is expected to improve the pion PID in this momentum region of 1 GeV/c <math>GeV/c.

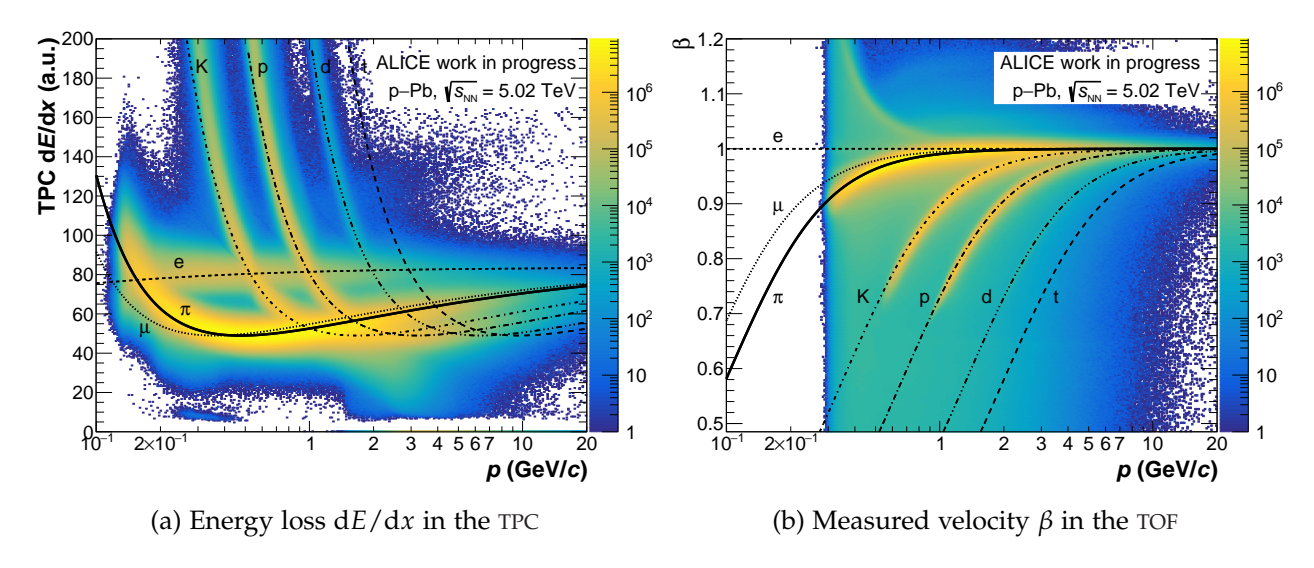


Figure 4.1: Energy loss and velocity measured by the TPC and TOF for all charged particles in the p-Pb dataset (analogous in pp). Labeled lines represent calculated expectation values for different particle species used for the PID.

Besides the expected calculated and labeled lines, unexpected shapes can be observed at velocities larger than the speed of light ($\beta > 1$), which are attributed to mismatches and pile-up of pion tracks, as derived in section A.2 of the appendix. Apart from these accumulations, a significant continuous background of measured velocities is found not being described by 4.2 for the mass of any known particle. These TOF signals are therefore assumed to come from mismatches between ITS-TPC tracks and the TOF cluster. As pions are the most abundant charged particles produced in high-energy collisions, these mismatches contain a significant fraction of pions. They should, therefore, not be excluded in the reconstruction of ω mesons. To retain this background of mismatched particles, the TOF is used to reject tracks likely to come from a kaon or proton. Also, since the TOF timing information is only available for around one third of all reconstructed tracks, this rejection only serves as a veto when a TOF time is available. Studies of different selection criteria show that the optimal balance between purity improvement and efficiency retainment is achieved when discarding tracks within three sigma of either the kaon or the proton band while being farther than five sigma from the pion band. In other words, a charged particle is identified as a pion if it is either within five sigma of the pion band or more than three sigma from the kaon and proton band.

The quality of the applied selection criteria can be judged by calculating the purity P and efficiency ε of reconstructed pions when applying the criteria to MC simulated data, as shown in figure 4.2. The purity quantifies how pure the sample of reconstructed pions is via the ratio of pions that were reconstructed and validated by the MC to be a true π^{\pm} , to all reconstructed pions. The efficiency quantifies how many true pions are lost in the reconstruction process and is defined as the ratio of validated, reconstructed pions to the total number of pions generated in the MC. The efficiency increases at low

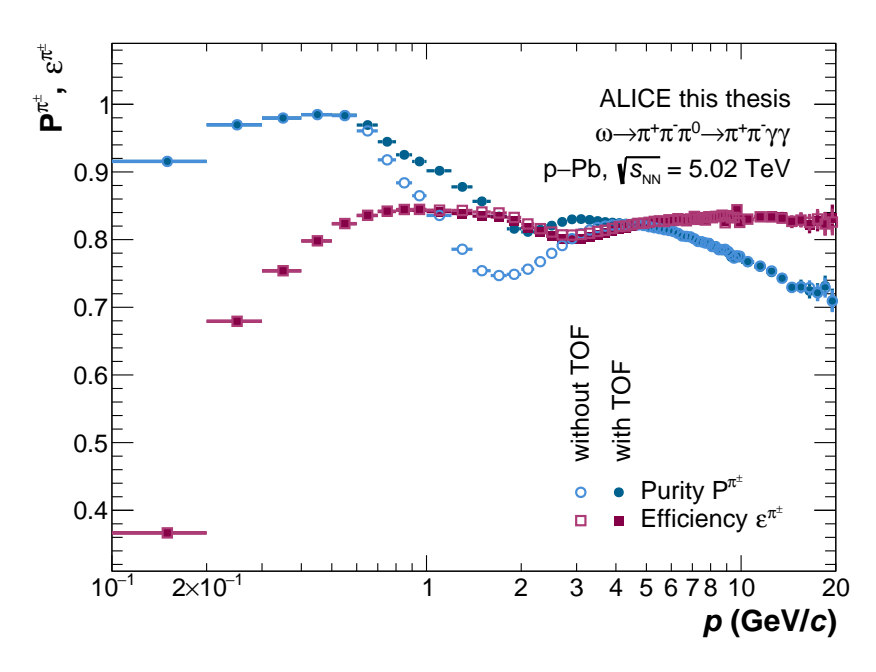


Figure 4.2: Efficiency and purity of the reconstructed charged pions in p-Pb collisions

momentum up to around 80%, where it saturates and is only decreased by around 1% by the TOF rejection for 1 $GeV/c \lesssim p \lesssim 4$ GeV/c. On the other hand, an overall decrease of the purity is observed with increasing momentum as the bands of more and more particles in both the TPC dE/dx and the TOF velocity merge with the band of the pions, therefore impeding effective identification in this momentum region. Figure 4.2 shows how the use of the TOF reduces the contamination by kaons and protons that cause the dip in the purity around $p \approx 2GeV/c$ and increase the purity by approximately 15%.

Compared to previous ω analyses [Lü23; Ach+20], this approach of rejecting tracks that are flagged by the TOF to likely stem from protons or kaons significantly increases the charged pion purity in the intermediate momentum region, thereby benefiting the ω reconstruction based on these pions.

4.2 PHOTON RECONSTRUCTION

As the neutral decay pions themselves decay within a few nanometers [Pdg22], they have to be reconstructed (see section 4.3) from their decay photons. The ALICE experiment offers two main ways of reconstructing these photons. Photons that traverse the inner barrel of the experiment and reach the calorimeters, like the EMCal, which is utilized in this analysis, are reconstructed in these calorimeters based on their deposited energy. With a probability of around 8.5%, photons will, however, convert into a dielectron pair before reaching the calorimeters [Abe+14c]. Using the so-called Photon Conversion Method (PCM), these electrons and positrons are identified from their ITS-TPC tracks and then combined to reconstruct the initial photon.

| Quantity | Setting |
|------------------------|--|
| Number of cells | $N_{\mathrm{cell}} \geq 1$ |
| Timing | $-20 \mathrm{ns} < t_{\mathrm{cls.}} < 25 \mathrm{ns}$ |
| Energy | $E_{\rm cls.} > 0.7{ m GeV}$ |
| Exotic clusters | Energy fraction $F_+ < 97 \%$ |
| Shape | $0.1 < \sigma_{ m long}^2 < 0.7$ |
| Track matching | $ \Delta\eta < 0.010 + (p_{\rm T} + 4.07)^{-2.5}$ |
| | $ \Delta \phi < 0.015 + (p_{\rm T} + 3.65)^{-2}$, $E/p < 1.75 c$ |

Table 4.2: Selection criteria used in this analysis for the selection of cluster photons

4.2.1 Photon Measurement with the EMCal

Photons and electrons reaching the EMCal produce electromagnetic showers in the detector, which can lead to their energy being deposited in multiple adjacent cells. A so-called *clusterizer* algorithm recombines these individual cells into clusters, as outlined in section 2.2.5. These clusters are then filtered based on the selection criteria listed in table 4.2. These selections are based mainly on recommendations from the performance report of the EMCal [Alia] and will be briefly reasoned in the following.

While some previous analyses required each cluster to contain at least two cells to reduce the impact of electronic noise [Ach+20; Str21], this is not required in this analysis, as it was since found that this can distort the reconstruction efficiencies, due to inaccurate descriptions in the MC simulations, introducing deviations of the final spectra at low $p_{\rm T}$ of up to 15 % [Alia].

A timing requirement restricts the signal time to be between 20 ns before and 25 ns after the time given by the T0 detector to reduce the influence of clusters from neighboring bunch-crossings.

Furthermore, several cluster observables are used to identify clusters likely to come from MIPs, neutrons, electrons, or other charged particles to exclude these clusters and thereby increase the fraction of clusters caused by a photon. To reduce, for example, the number of clusters from Minimum-Ionizing Particles (MIPs), which typically have an energy below $E_{\rm MIP} \lesssim 300$ MeV [Abe+14c], clusters are required to have a total energy of $E_{\rm cls.} > 700$ MeV. Another source of unwanted background signals comes from so-called exotic clusters. These clusters are suspected to be caused by slow neutrons hitting the cell's photo diode and are therefore characterized by one cell containing much more

energy than its neighboring cells. To identify these exotic clusters, an exoticism parameter F_+ is introduced for each cluster as:

$$F_{+} = 1 - E_{+} / E_{\text{cell}}^{\text{max}}, \tag{4.3}$$

where $E_{\rm cell}^{\rm max}$ is the energy of the cell with the highest energy and E_+ is the total energy of the four adjoining cells, sharing an edge with the maximum energy cell [Alia]. An electromagnetic shower caused by a photon extends to the adjoining cells, thereby reducing the exoticity parameter. Slow neutrons hitting one of the photo diodes on the other hand cause a very large exoticity. Clusters are classified as exotic and therefore discarded from the π^0 reconstruction when one of its cells has an exoticity of more than 97% [Alia].

The curvature of electron trajectories induced by the magnetic field can be used to discriminate their clusters based on the cluster's shape. For this purpose, the parameter $\sigma_{\rm long}^2$ is defined, roughly corresponding to the long axis, when parameterizing the shower as an ellipse [Alia]. As photons are unaffected by the magnetic field, their clusters are expected to be more circular, corresponding to a smaller σ_{long}^2 . At the same time, electron tracks are curved and reach the EMCal at an angle, producing elongated shower ellipses. Furthermore, elongated shower ellipses are often also caused by merging clusters of two incident particles reaching the EMCal close to one another, e.g. decay photons from a high $p_{\rm T} \pi^0$. Figure 4.3a shows the distribution of the shower parameter $\sigma_{\rm long}^2$ for all clusters of the p–Pb dataset, as well as vertical lines representing the limits of $0.1 < \sigma_{\rm long}^2 < 0.7$. The maximum is chosen based on simulation studies [Alia], suggesting that the peak around $\sigma_{\mathrm{long}}^2 \approx 0.6$ contains a larger fraction of photons than the plateau on the right, where the fraction of electrons and high- $p_{\rm T}$ π^{0} 's becomes more significant. Dotted vertical lines represent alternative settings for the maximum, either excluding the peak to the left or including the plateau to the right, which were used to estimate the systematic uncertainties (see 6.3).

A final exclusion of clusters not produced from photon showers is done by considering the distance between the shower and the closest track. The distance between EMCal clusters and their closest track in η and ϕ direction is shown in figure 4.3b. Besides a sizeable blue area corresponding to tracks unrelated to the respective cluster, a peak around $\Delta \eta = \Delta \phi = 0$ can be found corresponding to showers predominantly caused by charged particles. Since the resolution of this matching increases with rising momentum, the criterion for removing clusters with a nearby track is defined $p_{\rm T}$ dependent, as given in table 4.2. As described so far, this approach is susceptible to mismatching low momentum tracks to high-energetic photon clusters, thereby accidentally excluding these valid photons. Therefore, the clusters are only rejected based on matched tracks if the energy of the cluster is not too much higher than the momentum of the corresponding track: $E^{\rm cls}/p^{\rm track} < 1.75~c$ [Alia].

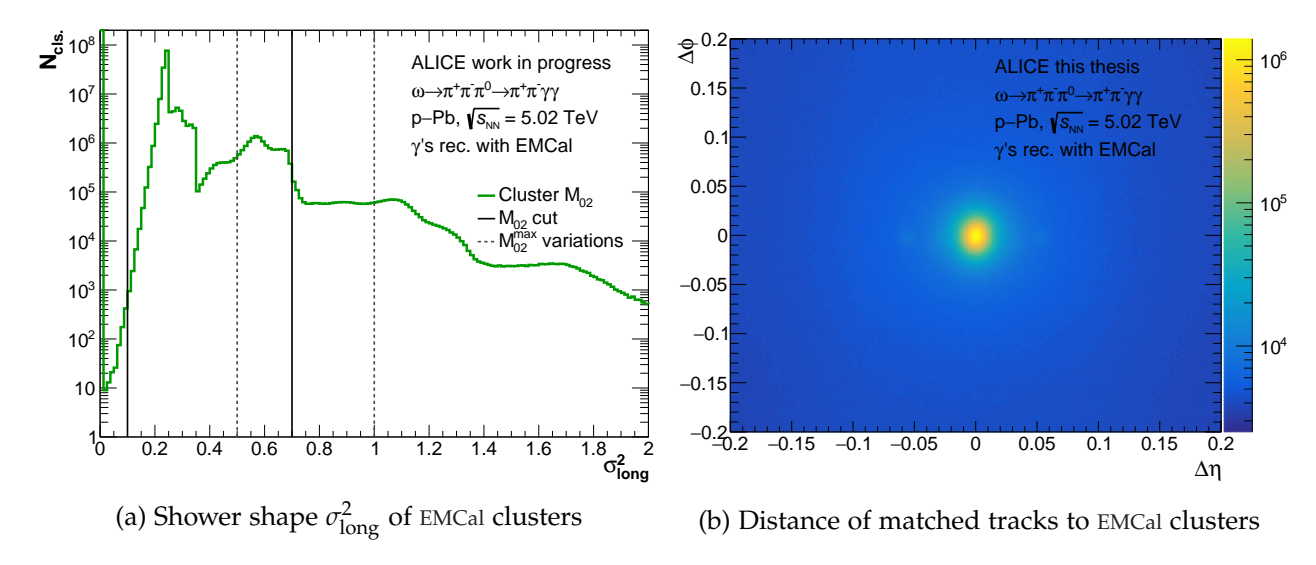


Figure 4.3: The shower shape of EMCal clusters is used to discriminate photons and electron/ π^0 clusters (left). The distance of EMCal clusters from the nearest tracks is used to discard clusters from charged particles (right).

4.2.2 The Photon Conversion Method (PCM)

The Photon Conversion Method (PCM) reconstructs the 8.5% of photons, that convert into e^+e^- pairs in the material of the ITS and TPC [Abe+14c]. Because of momentum and energy conservation, these conversions are only possible close to a nucleus, which can absorb some of the momentum in the reaction. Therefore, the dielectron pairs from these conversions always come from a displaced secondary vertex in the detector material. These secondary vertices are reconstructed from electron-positron tracks using a so-called online V^0 finding algorithm. The constructed photon candidates are then filtered based on the selection criteria compiled in table 4.3. These are primarily inspired by previous PCM analyses [Lü23; Koe22] and will be briefly explained in the following.

Photon candidates are required to have converted within $5\,\mathrm{cm} < R_\mathrm{conv.} < 180\,\mathrm{cm}$, where the lower limit is to prevent electrons and positrons from π^0 and η Dalitz decays to enter the reconstruction, and the upper limit of $180\,\mathrm{cm}$ is chosen to ensure good resolution of the e^+e^- tracks in the TPC. Good track quality is furthermore imposed by requiring a minimum $p_T \geq 40\,\mathrm{MeV/}c$ and for the track to contain a minimum of $60\,\%$ of the theoretically findable TPC clusters. In contrast to the charged pion tracks, where a fixed number of TPC clusters is required, the electron tracks requirement is given relative to a calculated maximum value of clusters that the electron could have created. This is done to account for the variable length of the electron track, depending on where the conversion took place. The $\mathrm{d}E/\mathrm{d}x$ measurement in the TPC is used to enhance the purity of electrons within this sample of charged tracks. First, only tracks are kept, that have an energy loss close to the calculated electron specific energy loss ($-3 < n\sigma^\mathrm{e} < 4$). In the next step, tracks with an energy loss within one sigma of the expected value for pions are

| Quantity | Setting |
|-------------------------------|---|
| Conversion Radius | $5 \text{cm} < R_{\text{conv.}} < 180 \text{cm}$ |
| Track p_{T} | $p_{ m T}~>40{ m MeV}$ |
| TPC clusters | $N_{ m cls.}/N_{ m findable~cls.} >$ 60% |
| Electron PID | $-3 < n\sigma^{\rm e} < 4$ |
| Pion rejection | $n\sigma^{\pi} > 1$ for $p > 0.4$ GeV/c |
| $q_{\mathbf{T}}$ | $q_{ m T}~<0.05{ m GeV}$ and $q_{ m T}~<0.125~p_{ m T}$ |
| $ \psi_{ m pair} $, χ^2 | $ \psi_{\text{pair}} < 0.055 \cdot \exp(0.3 \cdot \chi^2), \chi^2/\text{ndf} < 55$ |
| Pointing angle | $\cos(\theta) > 0.85$ |

Table 4.3: Selection criteria used in this analysis for selecting conversion photons

rejected if they have a momentum p > 0.4 GeV/c. This exception for tracks with very low momenta can be understood by looking at figure 4.1a, where the measured electron band crosses the calculated pion band at very low momenta.

While the previously mentioned cuts focused on the quality of the electron tracks, the following three cuts ensure a good quality of the conversion photon. For this purpose, a new variable q_T is introduced, which describes the momentum a daughter particle has, orthogonal to the momentum of its mother and is defined as follows:

$$q_{\rm T} = p_{\rm daughter} \cdot \sin \theta \text{ (mother-daughter)}.$$
 (4.4)

Here, θ (mother-daughter) described the angle between the momentum vector of the mother particle (photon) and its daughter particle (electron). As the converting photons do not have mass, any electron momentum transverse to the photon's momentum vector must be small and stem from the nucleus of the detector, which enables the conversion, motivating an upper limit for q_T in the selection of conversion photons. A further, more sophisticated combined criterion based on the reduced χ^2 from the fit of the e^+e^- pair and the angle between the conversion pair plane and the magnetic field $|\psi_{pair}|$ reduces the background of combinatorial e^+e^- pairs [Boc17]. Unlike the photon measurement using the EMCal, the PCM method allows for the calculation of the momentum orientation of the photon. From this orientation, the angular deviation θ to the direct path from the primary to the secondary vertex can be calculated. This deviation is expected to be zero for real conversion photons, motivating the final selection criterion of $\cos(\theta) > 0.85$.

Neutral meson analyses performed before 2023 list the material budget as one of their leading systematic uncertainties. However, the analysis presented in this thesis is one of the first to use a recently developed, data-driven correction. By weighting conversions in the MC at different distances in the radial direction according to so-called Material Budget Weights (MBWs), the PCM material uncertainty has been halved to 2.5 % [Ach+23].

4.3 NEUTRAL PION RECONSTRUCTION

Before ω mesons can be reconstructed from their three pion decay (see chapter 5), the intermediate neutral decay pion is reconstructed from its two pion decay with a branching ratio of $\mathcal{B}(\pi^0 \to \gamma \gamma) = 98.8 \%$ [Pdg22]. Given the energies E_i of these two decay photons and the angle $\theta_{\gamma\gamma}$ between them, the invariant mass $M_{\gamma\gamma}$ of their mother particle can be calculated as follows:

$$M_{\gamma\gamma} = \sqrt{2E_1 E_2 (1 - \cos \theta_{\gamma\gamma})}.$$
 (4.5)

When analyzing the photons produced in high-energy particle collisions, it is not known which photons came from a decay, let alone which pairs stem from the same mother particle. This is solved by a statistical approach, in which the invariant masses of all photon pairs within a given event are calculated according to equation 4.5. While these π^0 candidates contain many combinations that do not correspond to any real-world mother particle, this background is expected to be continuous, compared to an excess around masses of possible mother particles, where these correct combinations add to the combinatoric background.

From the two different photon reconstruction methods PCM and EMCal discussed in the previous sections, there are three combinations of photon sources, with which π^0 candidates can be formed:

- The PCM method reconstructs π^0 's from two photons that have been reconstructed using PCM.
- The PCM-EMCal method is a hybrid method using one photon reconstructed by PCM and another one measured in the EMCal
- The EMCal method reconstructs the π^0 's from pairs of photons that are both measured in the EMCal

Figure 4.4 shows the number of π^0 candidates as a function of their invariant mass and their transverse momentum for each of the abovementioned methods. For all three methods, a background of combinatoric photon pairs is observed, not belonging to the same mother particle. Above this background, there is an excess around the invariant mass of the neutral pion: $M_{\pi^0} \approx 135 \text{ MeV/}c^2$ [Pdg22].

To reduce the background of combinatoric photon pairs, π^0 candidates with an invariant mass far from the expected π^0 value are removed and not considered for the subsequent reconstruction of ω mesons. As detector-calibration effects have been shown to affect both the position and the width of the measured π^0 mass [Koe22], the mass selection windows are based on the width and mass of the π^0 as measured with the respective method. For this purpose, the p_T dependent width and mass of the π^0 , measured for the three reconstruction methods at $\sqrt{s}=13$ TeV [Koe22], was parameterized using polynomials. While the reconstructed π^0 mass has been calibrated on the detector

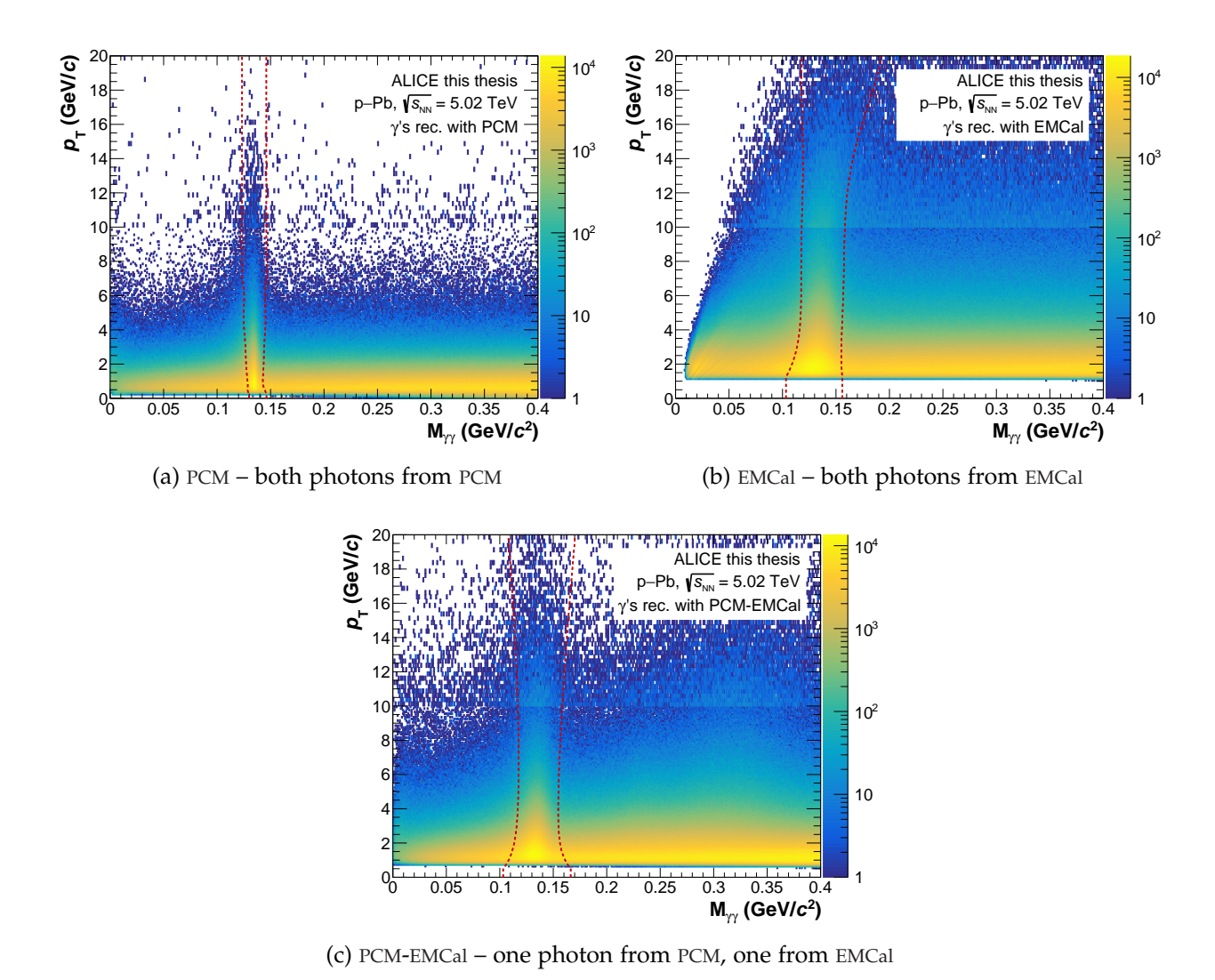


Figure 4.4: Invariant mass distributions of all photon pairs in each event of the p-Pb dataset as a function of transverse momentum for the three different reconstruction methods. For the subsequent ω meson reconstruction, only pion candidates in the $p_{\rm T}$ dependent mass range between the red, dotted lines were selected.

level to be similar between the three methods, the width differs severely, as it is largely influenced by the resolution of the involved detectors. This can also be observed in the distributions presented in figure 4.4, where the π^0 excess has a much smaller width when reconstructed with PCM than with the EMCal, thanks to the remarkable momentum resolution of the TPC, especially at low $p_{\rm T}$ (see 2.3a).

The different advantages and disadvantages of the three methods motivate slightly different strictness on the mass selection criterion to account for these differences.

While PCM, for example, benefits from its good energy resolution, its reconstruction requires both photons to convert, which only happens for $8.5^2~\%=0.7~\%$ of the neutral pions [Abe+14c]. To compensate for this reduced number of π^0 's, the mass of the pions is only required to be within $3\sigma_{\pi^0}$ of the expected value to prevent a further efficiency reduction: $|M_{\gamma\gamma}-M_{\pi^0}|<3\sigma_{\pi^0}$, where M_π^0 and σ_{π^0} represent the p_T dependent parametrizations of the measured width and mass of the neutral pion, and $M_{\gamma\gamma}$ the mass of the π^0 candidate in question. For the EMCal, on the other hand, the small signal-to-background ratio caused by the lower energy resolution is the primary concern. Therefore, a tighter mass requirement of $|M_{\gamma\gamma}-M_{\pi^0}|<2\sigma_{\pi^0}$ is applied to select a mass region with a higher signal-to-background ratio.

When combining one photon reconstructed with PCM, with one from the EMCal to one π^0 (PCM-EMCal), the mass requirement was selected to be between the individual methods to balance efficiency and of the signal-to-background ratio: $M_{\gamma\gamma} - M_{\pi^0} < 2.5\sigma_{\pi^0}$.

As a final step in preparing pions for the subsequent ω reconstruction, it is insightful to understand how the transverse momentum of reconstructed ω mesons is distributed in its decay into the three pions. One could naively assume that the ω mesons symmetric decay into three pions means that the transverse momentum of the three reconstructed pions forming one true ω meson is on average the same, with each pion on average contributing one third to the total transverse momentum of the ω . However, the reconstruction efficiency of the different pions results in an uneven distribution of the transverse momenta among the pions. Figure 4.5 shows what fraction of the omegas transverse momentum $p_{\rm T}^{\omega}$ the neutral pion holds on average $\langle p_{\rm T}^{\pi} \rangle$ for the different methods, as a function of the ω mesons transverse momentum. This depiction shows that even for reconstructed ω mesons with large transverse momentum, the neutral pion, on average, carries around half of the momentum of the ω , instead of the naive assumption of $\langle p_{\rm T}^{\pi} \rangle/p_{\rm T}^{\omega} \sim 1/3$.

This large momentum fraction that the π^0 carries is explained by the increase of its reconstruction efficiency with larger p_T [Koe22], while the reconstruction efficiency of the charged pions saturates around $p_T \approx 1$ GeV/c. This increases the likelihood of reconstruction for ω mesons that decay into a π^0 with large transverse momentum. Furthermore, it is found that at low p_T , this bias towards the reconstruction of ω mesons with high- p_T decay π^0 's increases, caused by the minimum energy requirements for

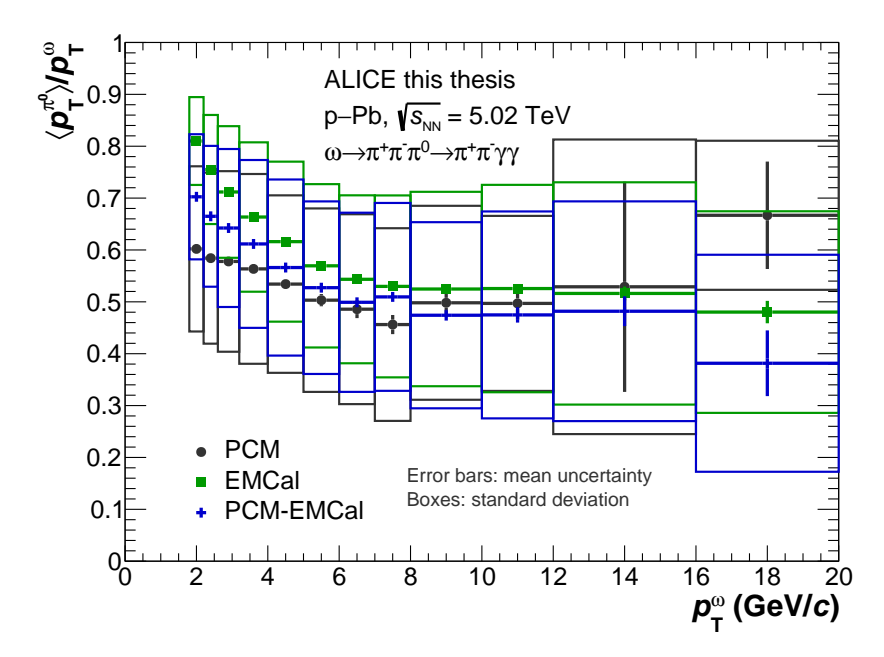


Figure 4.5: Fraction of the ω mesons transverse momentum, that its decay π^0 carries on average. Extracted from the properties of the generated ω mesons and their decay pions in the p-Pb MC simulation.

the decay photons, especially involving the EMCal. Understanding how the transverse momentum of reconstructed ω mesons is correlated to the transverse momenta of its decay pions is crucial in studying the limitations and possible improvements of the presented analysis.

OMEGA MESON RECONSTRUCTION

This chapter is dedicated to how ω meson candidates are reconstructed from the charged and neutral pions of the previous sections. The reconstruction points out the primary concern in this analysis being the relatively small signal smeared by the detector resolution, in contrast to the large combinatoric background. A novel method of enhancing the limited mass resolution is therefore explained in section 5.1, followed by a detailed study of the background contributions and possible approaches to reducing it in section 5.2. The final section 5.3 then covers how a raw yield of ω mesons is extracted from the ω candidates.

Similar to the reconstruction of neutral pions presented in section 4.3, ω mesons are extracted using a statistical approach from all π^+ $\pi^ \pi^0$ combinations within each event. From the four-momenta of the measured charged and reconstructed neutral pions, the mass and transverse momentum of these π^+ $\pi^ \pi^0$ combinations are reconstructed. The resulting two-dimensional $M_{\pi^+\pi^-\pi^0}$ - $p_{\rm T}$ distributions are then projected in $p_{\rm T}$ intervals, leading to invariant-mass distributions like the one shown in blue in figure 5.1. A small excess of these ω meson candidates is observed above the large combinatoric background around $M_{\omega} \approx 782 \text{ MeV/}c^2$ [Pdg22]. As will be explained in detail in section 5.3, the background, described by a third-order polynomial, is subtracted, revealing the raw signal of ω mesons. For better visibility, the data points representing this signal in figure 5.1 are scaled by a factor of five. By parameterizing this signal with a Gaussian, the width (FWHM) of the signal can be extracted, which in the case of the example bin shown in figure 5.1 is found to be $\Gamma_{\omega} \approx 48 \text{ MeV/}c^2$. This measured width is much larger than the natural decay width of the ω meson of $\Gamma_{\omega}=8.49\,\mathrm{MeV}/c^2$ [Pdg22]. This observed broadening of the ω signal can be traced back to the finite resolution of the detectors involved in the reconstruction. The following section introduces a new mass-resolution correction that was developed to reduce the impact of the limited detector resolution.

5.1 MASS RESOLUTION CORRECTION

To investigate possible corrections for the observed smearing, it has to be traced back from where it predominantly originates. This is done by considering the concrete example distribution for the transverse momentum range of $5 < p_T$ (GeV/c) < 6 shown in figure 5.1. As shown in figure 4.5, neutral pions coming from a decay of ω mesons at these transverse momenta carry on average around 60% of the ω mesons transverse momentum. This transverse momentum is then split between the two photons, leaving each with around

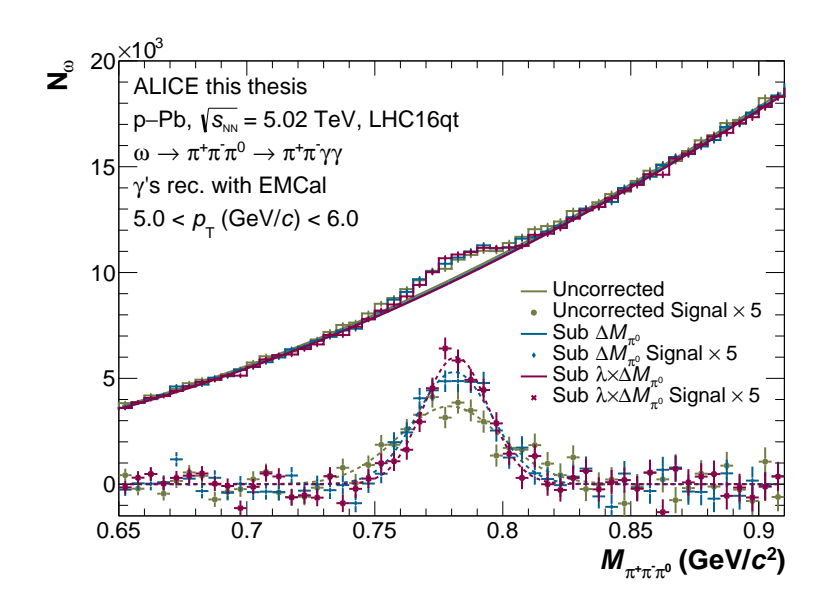


Figure 5.1: Example invariant-mass distribution of ω meson candidates with photons reconstructed with the EMCal. While the blue distribution corresponds to uncorrected candidates, the green and red distribution have been corrected as described in section 5.1.

 $\langle p_{\rm T}^{\gamma} \rangle \approx 1.5$ GeV/c. The charged pions each have, on average, a transverse momentum around $\langle p_{\rm T}^{\pi^{\pm}} \rangle \approx 1$ GeV/c. When referring to the resolution of the ITS-TPC tracking and that of the EMCal shown in figure 2.3, it can be estimated that the charged decay pions are measured with a resolution of around 1%, while the energy of the two photons is resolved with a precision of around 8%. While the mentioned numbers are all specific to the example reconstruction method and $p_{\rm T}$ range presented in figure 5.1, the conclusion holds true for all methods and $p_{\rm T}$ intervals that the smearing of the ω meson signal is mainly caused by the resolution of the π^0 reconstruction.

The smearing by the EMCal can, however, be reduced by utilizing the known mass of the π^0 in the decay chain $\omega \to \pi^+ \pi^- \pi^0 \to \pi^+ \pi^0 \gamma \gamma$. As the lifetime of neutral pions is 10^6 times larger than that of the ω mesons [Pdg22], the π^0 's decay width is one million times smaller and therefore negligible. Preceding analyses with similar decay channels developed a few different methods to exploit the known π^0 mass, such as adjusting the momentum or the energy [Hem21] of the π^0 to align its reconstructed mass with the literary value. The established method for ω measurements by ALICE, as used in the pp analyses at $\sqrt{s}=7$ TeV [Ach+20] and $\sqrt{s}=13$ TeV [Lü23] is the subtraction of the measurement error ΔM_{π^0} of the π^0 mass from the mass $M_{\pi^0}^{PDG}$ published by the Particle Data Group (PDG) [Pdg22], from the reconstructed ω mass M_{ω}^{rec} .

$$M_{\omega} = M_{\omega}^{\text{rec}} - \underbrace{\left(M_{\pi^0}^{\text{rec}} - M_{\pi^0}^{\text{PDG}}\right)}_{\Delta M_{\pi^0}} \tag{5.1}$$

The underlying idea behind this correction is that an energy smearing increasing the π^0 mass by ΔM_{π^0} propagates to an equally increased ω mass ΔM_{ω} . Going back to the example shown in figure 5.1, the effect of applying the correction described by equation 5.1 to all ω meson candidates (π^+ $\pi^ \pi^0$ -pairs) is depicted by the green invariant-mass distribution. Especially when looking at the signal after the background subtraction, a much sharper peak appears than for the uncorrected distribution in blue. While equation 5.1 offers an effective correction to mitigate the smearing of the ω signal, this approach falsely treats invariant masses as additive quantities by subtracting the measurement error for a daughter particle from the mass of its mother particle.

As this established method can, therefore, not be an exact solution and it is furthermore neither motivated by any data nor MC input, a new method was developed for this analysis, building upon the established approach, in an effort further to reduce the smearing of the ω signal. Similar to the established method described by equation 5.1, this new lambda-correction also consists of a small shift ΔM_{ω} to the mass of each reconstructed ω meson. The new lambda-correction, however, does not assume that a measurement error of the π^0 mass directly propagates into a measurement error of equal strength in the mass of the ω , but instead, a new MC driven parameter λ is introduced to quantify this correlation. This λ parameter quantifies the correlation between the deviation of the reconstructed to the true ω mass ΔM_{ω} and the deviation of the reconstructed π^0 mass to the literary value ΔM_{π^0} . It is extracted from MC simulations by compiling the relation between ΔM_{ω} and ΔM_{π^0} for all reconstructed and by the MC validated ω mesons. This correlation for a combined pp and p-Pb dataset is shown in figure 5.2 for the three different photon reconstruction methods. Furthermore, the correlations are extracted individually for different π^0 opening angles $\theta_{\gamma\gamma}$, as explained in a later paragraph.

The horizontal axis in figure 5.2 depicts the difference between the invariant mass of reconstructed neutral pions to their literary value of $M_{\pi^0}^{PDG}=134.98\,\text{MeV}/c^2$ [Pdg22]. The vertical axis, on the other hand, shows the difference between the reconstructed and the true mass of the ω meson that decayed into the respective π^0 . A diagonal dotted line corresponds to the method described by equation 5.1, which assumes $\Delta M_{\omega}=\Delta M_{\pi^0}$. As this assumption does not describe the observed correlation, another linear parameterization is used to quantify the averaged correlation. This linear parameterization of the correlation is shown in figure 5.2 as red lines. The gradient of this parameterization is called λ and describes the averaged ratio of the measurement error of the ω mass to that of its corresponding π^0 , as shown in equation 5.2.

$$\lambda = \left\langle \frac{\Delta M_{\omega}}{\Delta M_{\pi^0}} \right\rangle = \left\langle \frac{M_{\omega}^{\text{rec}} - M_{\omega}^{\text{true}}}{M_{\pi^0}^{\text{rec}} - M_{\pi^0}^{\text{PDG}}} \right\rangle \tag{5.2}$$

Suppose the dimensionless λ factor is, for example, $\lambda \approx 2$ as for the EMCal in figure 5.2f. In that case, the error of the reconstructed ω mass is, on average, twice as large as the discrepancy between the measured π^0 mass and the literary value.

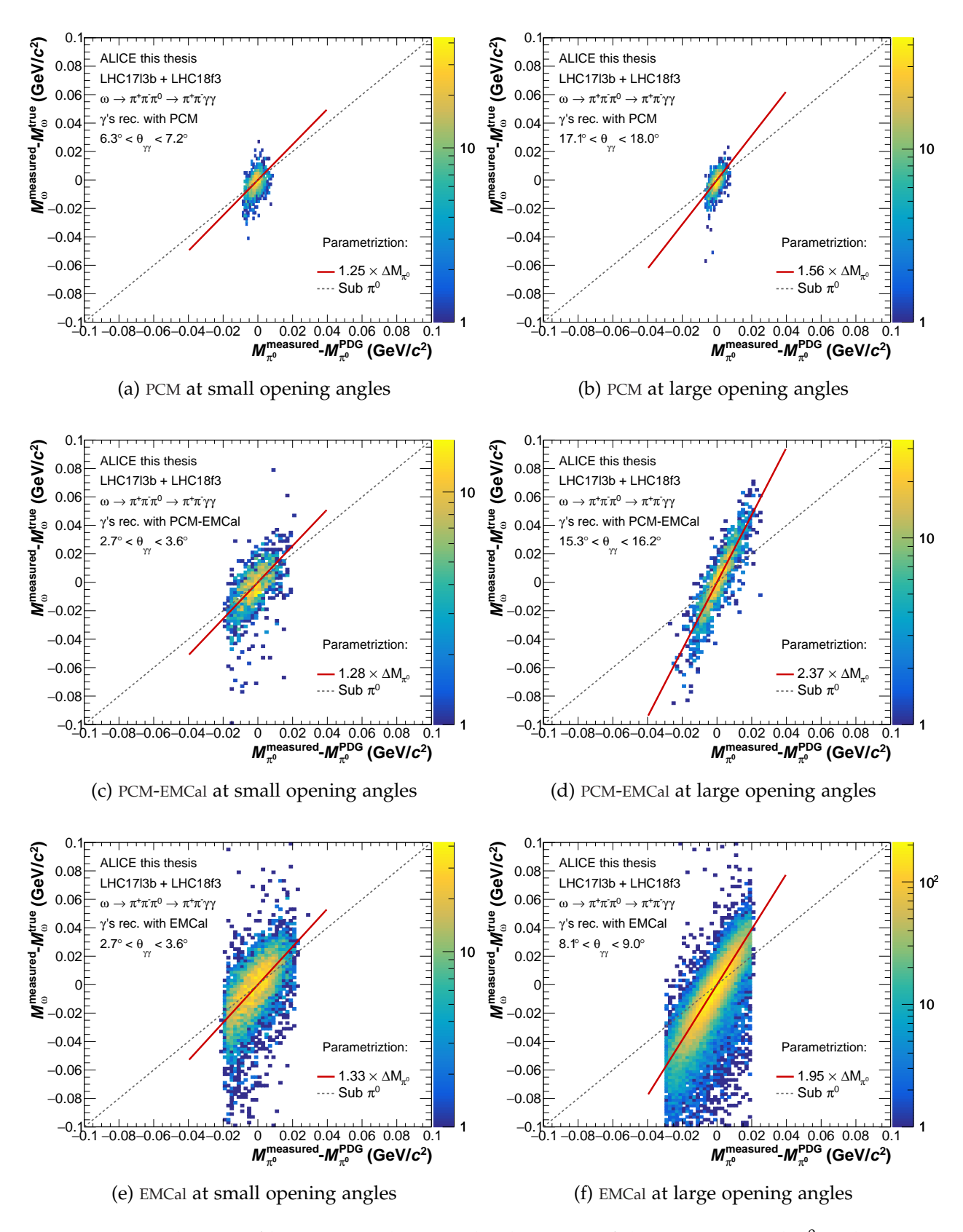
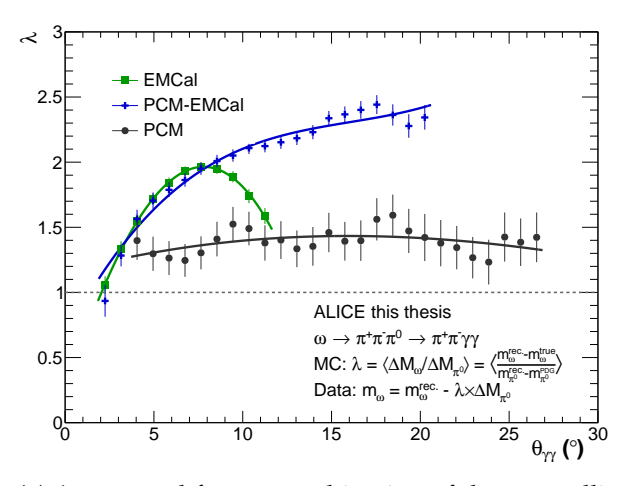
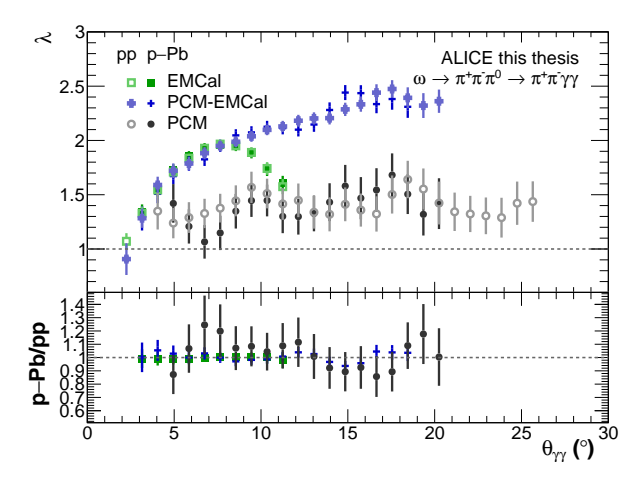


Figure 5.2: A selection of histograms showing the deviation of the reconstructed π^0 and ω mass for true ω mesons and their respective decay π^0 . From top to bottom, the three different reconstruction methods are shown with an example bin at small opening angles $\theta_{\gamma\gamma}$ on the left and larger π^0 opening angles on the right. The gradient of the linear fit function, shown in red, is extracted for each method and $\theta_{\gamma\gamma}$ -interval and compiled in figure 5.3a.



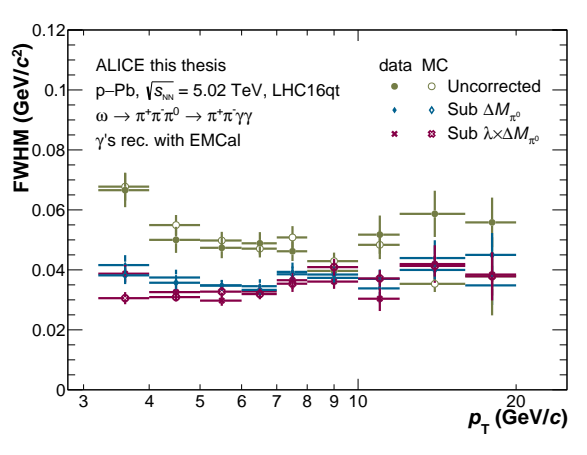


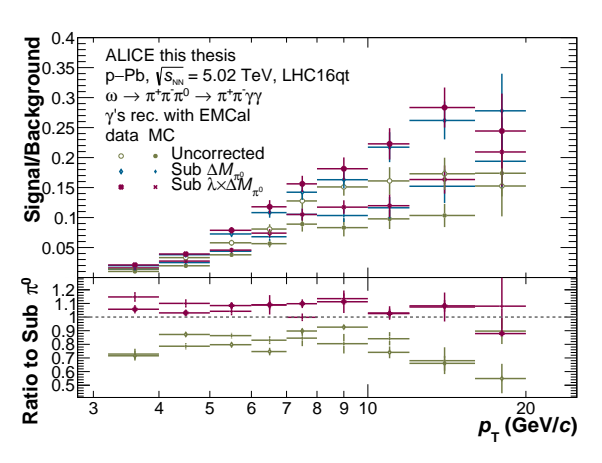
- (a) λ extracted from a combination of the two collision systems parameterized by a polynomial
- (b) Comparison of λ 's in pp and p-Pb showing good agreement between the collision systems

Figure 5.3: Opening angle dependent λ parameter extracted from the pp and p-Pb MC simulations for the three photon reconstruction methods

As can be seen in figure 5.2, the correlation between the error of the reconstructed ω and π^0 masses is not the same when looking at different π^0 opening angles $\theta_{\gamma\gamma}$. This opening angle dependence is accounted for by extracting λ in different $\theta_{\gamma\gamma}$ intervals in an effort to enhance the correlation, as a more direct correlation between the two mass measurement errors allows for a more effective correction. Smaller studies were also performed in which the correlation was extracted differential in other parameters, such as the transverse momentum of the π^0 or the ω . However, the correlation and, therefore, the correction's usefulness were very similar. The resulting $\lambda(\theta_{\gamma\gamma})$ distribution is shown in figure 5.3a, in which each data point corresponds to the gradient of the linear parameterization to a distribution, such as the ones shown in figure 5.2. The intuitive reason for this opening angle dependence is understood to come from the fact that the limited energy resolution of the TPC and EMCal not only smear the energy of the π^0 and therefore the ω , but since the two decay photons are smeared independently, the spacial resolution is also impacted. If, for example, only one of the decay photons' energy is smeared to a higher energy, then the reconstructed π^0 momentum vector will be shifted towards that photon. As the invariant mass of the ω meson is calculated from the sum of the four-momenta of the three decay pions, such a rotation of the π^0 directly influences the reconstructed mass. While this shift is limited for small π^0 opening angles $\theta_{\gamma\gamma}$, this effect becomes more critical for larger opening angles. Comparing again to the established method, that would correspond to the black dotted line at $\lambda = 1$ in figure 5.2 and thereby underestimates this correlation factor for all reconstruction methods.

The correlation parameter λ has to be individually determined for the different photon methods since the energy and space resolutions differ drastically. However, λ has been found to be universal between different collision systems, which is expected since it stems from decay dynamics and detector effects, both of which are independent of the





- (a) Widths extracted in data and MC
- (b) Signal to background ratios and their ratios to the established method

Figure 5.4: Width (left) and signal to background ratio (right) of the ω signal extracted with EMCal in p-Pb. Blue markers show them without any correction, the green ones show the currently established correction, and the red ones show the new λ correction.

collision system. This can be observed in figure 5.3b, where the λ parameter has been extracted in pp and p-Pb collisions individually. The ratio of λ parameters in the two collision systems shows no significant deviation from unity for any photon reconstruction methods. To decrease fluctuations in the λ extraction, the correlations in pp and p-Pb were therefore combined for the extraction of the $\lambda(\theta_{\gamma\gamma})$ parameters shown in figure 5.3a. The extracted correlations $\lambda(\theta_{\gamma\gamma})$ are parameterized by a third-order polynomial to provide a continuous correlation parameter for use in the reconstruction.

In order to apply this correction in the ω meson reconstruction, equation 5.2 can be rearranged to calculate M_{ω}^{true} , which is used as the reconstructed ω mass in data M_{ω} :

$$M_{\omega} = M_{\omega}^{\text{rec}} - \lambda(\theta_{\gamma\gamma}) \times \left(M_{\pi^0}^{\text{rec}} - M_{\pi^0}^{\text{PDG}}\right). \tag{5.3}$$

The presented *lambda-correction* is applied for the reconstruction of ω mesons in this analysis by correcting the mass of every ω using equation 5.3, taking the third-order polynomial shown in 5.3a as input.

The distribution shown with red markers in figure 5.1, and especially the signal after background subtraction, show how this new correction produces a sharper ω peak than the old, established method in blue, which already had a much smaller width than the uncorrected signal in green. The effects of this new correction are furthermore displayed in figure 5.4, with a decrease of the width accompanied by an increase of the signal-to-background ratio in almost every $p_{\rm T}$ -interval.

When using such a MC-driven correction for the reconstruction in data and MC, effects of a possible MC-bias have to be carefully monitored. This possible bias is accounted for in the systematic uncertainties by using the old resolution correction as a variation, as described in section 6.3.

An exact analytic solution to revert the smearing is believed to be impossible since the two free parameters (ΔE_{γ}^{1} , ΔE_{γ}^{2}) cannot be determined using only one known input ($M_{\pi^{0}}^{PDG}$). The presented λ correction (equation 5.3) provides a new, MC-driven approach that is able to mitigate the effects of limited detector resolution. The use of this correction is, however, not limited to this analysis or even ω analyses. As such, the presented correction is already applied to an η' analysis in ALICE [Gli].

5.2 BACKGROUND STUDIES

Compared to the reconstruction of other neutral mesons like the π^0 or η [Koe22], the signal extraction of the ω meson suffers from a much smaller signal-to-background ratio. This not only reduces the $p_{\rm T}$ reach of the analysis but also increases both the statistical and the systematic uncertainties. Therefore, understanding the background in the invariant mass distribution is an important aspect of ω meson analyses.

5.2.1 Background Contributions

A breakdown of the contributions to the ω meson background given by MC is shown in figure 5.5a for the example of the EMCal method in p-Pb at relatively low p_T , where the signal to background ratio is the smallest. The background contributions for other p_T intervals, reconstruction methods, and collision systems can be found in the appendix in figures A.13, A.14 and A.15. The distribution of all ω candidates in figure 5.5 displays small peaks at the η and the ω mass on top of a very large background. All the other (colored) contributions summed together yield the black invariant mass distribution. Two background contributions are much more significant than the others: One is shown in yellow and corresponds to ω candidates reconstructed from a photon pair that does not come from a true π^0 . As the π^0 identification is only based on the invariant mass of the pair, many wrong combinatoric photon pairs enter the ω reconstruction. One option for reducing the contribution of π^0 contamination is to apply stricter mass cuts on the photon pairs. However, this not only reduces the efficiency but also increases the dependence on a good description of the distributions by the MC and is therefore not further pursued. The other dominant background source is depicted in pink and describes ω candidates whose reconstructed pions have been correctly identified but have three different mother particles. This means they are completely uncorrelated, and reducing this type of background is very challenging. It could mainly be accomplished by removing pions identified as coming from a particle other than an ω . Such a prefilter was investigated and will be discussed in the following paragraph. The next largest background contribution is already much smaller and describes ω meson candidates, for which all pions were correctly identified, and two pions come from the same mother, but not an ω . This can either mean that the two charged pions came from the same mother (e.g. from a K_s^0) or one

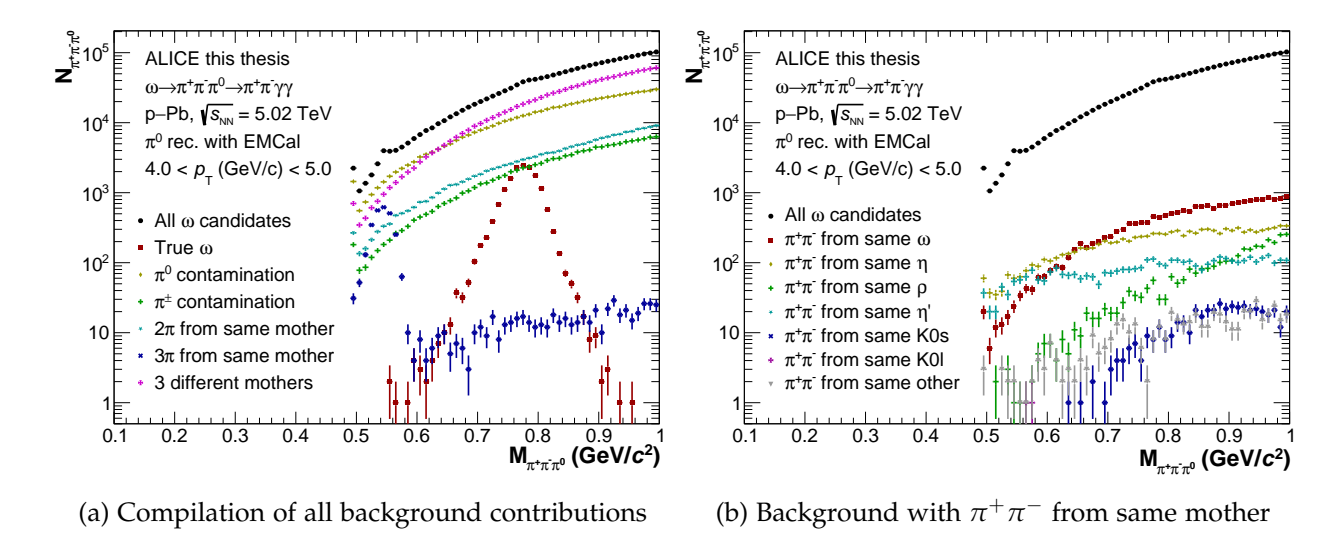


Figure 5.5: Breakdown of the contributions to the invariant-mass distributions of ω candidates within $4~{\rm GeV/}c < p_{\rm T}^{\pi^+\pi^-} < 5~{\rm GeV/}c$ using the EMCal in the p–Pb MC

charged pion and the neutral pion. The composition of which mother particles cause this background contribution is shown for the example of $\pi^+\pi^-$ from the same mother in figure 5.5b. The contribution from three pions from the same mother is negligible in the mass region above the η peak at $M_{\pi^+\pi^-\pi^0} > 0.6\,\text{GeV/}c$. The final contribution comes from wrongly identified charged pions shown as green markers. As discussed in section 4.1, the purity of charged pions in ALICE has been optimized in this analysis by using a combination of the TPC dE/dx and the time of flight from the TOF detector and saturates around 80%.

5.2.2 *Feasibility of a ρ Prefilter*

In order to reduce the background underneath the ω meson signal, the feasibility of a ρ prefilter was investigated. In its simplest form, the invariant mass of all $\pi^+\pi^-$ pairs would be calculated. If this mass was close to the ρ^0 mass of $m_{\rho^0}^{PDG}$ = 770 MeV/ c^2 [Pdg22], these charged pions would be assumed to have originated from a $\rho^0 \to \pi^+\pi^-$ decay and would therefore not be considered for the reconstruction of ω mesons. The motivation behind such a prefilter is to reduce the number of combinatorial ω candidates by removing charged pions that do not come from ω meson decays.

The feasibility of such a prefilter can be discussed based on figure 5.6, which shows the invariant-mass distribution of all $\pi^+\pi^-$ combinations with a transverse momentum within 4 GeV/c $< p_{\rm T}^{\pi^+\pi^-} < 5$ GeV/c for the example of using the EMCal in the p-Pb MC. The figures A.16, A.17 and A.18 in the appendix show the distributions for all $p_{\rm T}$ regions, reconstruction methods, and collision systems. The black distribution shows all possible pairs from reconstructed pions; in red, only those where both pions were

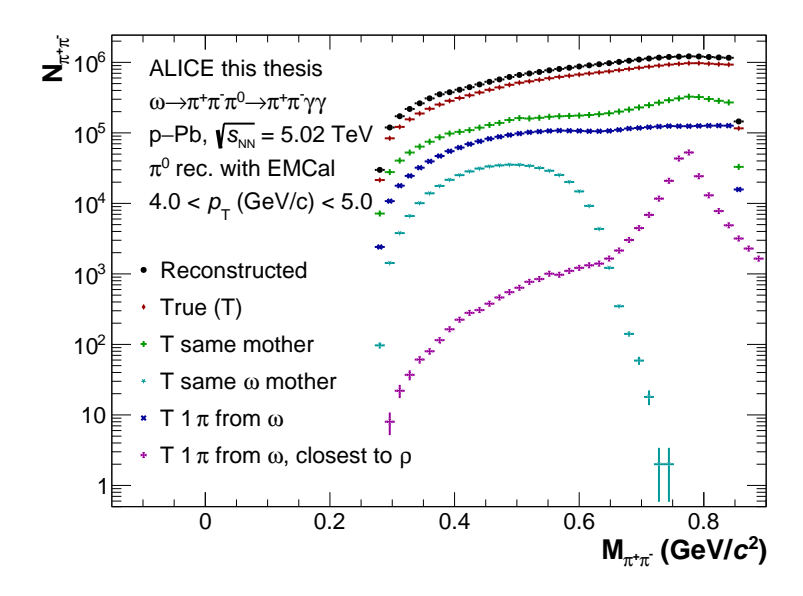


Figure 5.6: Breakdown of the contributions to the invariant mass distributions of all reconstructed $\pi^+\pi^-$ pairs within $4~{\rm GeV/}c < p_{\rm T}^{\pi^+\pi^-} < 5~{\rm GeV/}c$ in the p-Pb MC

correctly identified. The subsample of $\pi^+\pi^-$ pairs from the same mother is shown in green. Around the ρ mass, a small peak is observed: the target of a possible prefilter. $\pi^+\pi^-$ pairs that come from the same ω meson are shown in cyan and can be found at much smaller masses since the third pion (π^0) of the ω decay is not included in the mass on the horizontal axis. Using a prefilter, all charged pions would be removed that have a partner with which they have a combined invariant mass close to the ρ mass. This motivates the blue distribution, which depicts all $\pi^+\pi^-$ pairs, of which at least one of the pions comes from an ω . This distribution is much larger than the cyan distribution, as there are many more wrong combinations than correct ones. When considering the efficiency of a possible prefilter, it is important to note that if only one of the pions is removed by the prefilter, the corresponding ω meson is not reconstructable anymore. The purple distribution is filled once for every true ω meson with the mass of its decay pions and any other pion if it is closest to the ρ mass. This is thereby the $\pi^+\pi^-$ combination, which is the most likely to cause the corresponding ω meson to be removed by a prefilter. As there are so many combinatoric wrong combinations of pions, with one of them coming from an ω (blue), most ω mesons also have a pion, which pairs close to the ρ mass with another pion. This results in the peak around the ρ mass. When implementing a prefilter above a given mass, e.g. $M_{\pi^+\pi^-} > 0.7 \,\text{GeV}/c^2$, the fraction of the purple distribution above this mass would correspond to the loss in efficiency. As can be seen, this efficiency loss would be very large (> 90 %), and therefore a prefilter was found not to be feasible.

5.2.3 *Impact of Possible DCA Restrictions*

As introduced in section 4.1, the Distance of Closest Approach (DCA) of charged particles from the vertex is restricted to be within DCA_{xy} < 3.2 cm and DCA_z < 2.4 cm, thereby mitigating background contributions from weak decays. In an effort to further reduce the background from displaced decay vertices, variations of tighter DCA restrictions were studied. The significances achieved with and without stricter DCA restrictions are shown in the appendix in figure A.12. All studied DCA restrictions caused a reduction of the significance of the extracted signal. This can be explained using figure 5.5b, which shows that the only weak decays contributing to the π^+ π^- background of the ω meson are those of K_s^0 mesons. This background contribution is, however, negligible compared to other particle decays. This is also the case for the other p_T bins, reconstruction methods, and collision systems, as can be seen in figures A.13, A.14 and A.15. The Kaon contribution is considered small because it is already Lorentz-boosted considerably at the considered transverse momenta. Therefore, only a tiny fraction of them decay within the inner barrel. Stricter DCA restrictions, therefore, do not significantly reduce the background while reducing the efficiency by cutting into the DCA resolution. For this reason, the DCA requirement was set to the relatively loose setting of DCA_{xy} < 3.2 cm and DCA_z < 2.4 cm.

5.3 SIGNAL EXTRACTION

With this knowledge about the sources of the background as well as the signal smearing and how to reduce their effects, this section discusses how the raw yield of ω mesons is extracted from the reconstructed ω meson candidates. As explained at the beginning of this chapter, the mass and transverse momentum of all combinations of $\pi^+\pi^-\pi^0$ within each event is calculated, where the mass of these ω candidates is then corrected using the mass resolution correction described by equation 5.3 from the previous section. These two-dimensional $p_{\rm T}$ - $M_{\pi^+\pi^-\pi^0}$ distributions are then projected in the following $p_{\rm T}$ intervals, which are chosen to ensure aligning interval edges with the π^0 analyses at $\sqrt{s_{\rm NN}}=5.02$ TeV [SS19; Ach+18b], thereby allowing for a direct calculation of the ω/π^0 ratio in a later stage of the analysis.

$$p_{\mathrm{T}}^{\mathrm{edges}}(\mathrm{GeV}/c): 1.8 \mid 2.2 \mid 2.6 \mid 3.2 \mid 4.0 \mid 5.0 \mid 6.0 \mid 7.0 \mid 8.0 \mid 10.0 \mid 12.0 \mid 16.0 \mid 20.0 \mid 10.0 \mid$$

The resulting invariant-mass distributions of these ω candidates are shown in figure 5.7 for an example p_T interval of each reconstruction method and both collision systems. The subsequent extraction of the ω meson signal consists of the following steps, which are performed on the ω candidates in every p_T interval, reconstruction method, and for both data and MC in both collision systems:

- 1. The background is parameterized with a third-order polynomial excluding the signal region ($M_{\omega} \pm 3\sigma_{\omega}$) with the masses and widths taken from table 5.1. Using a third-order polynomial is based on extensive studies of different background descriptions (e.g. event mixing, rotation- and like sign method) [Str21], where the third-order polynomial was found to describe the combinatoric background best [Lü23; Str21]. This background description is shown as a blue curve in the invariant mass distributions in figure 5.7.
- 2. The polynomial describing the background is subtracted from the ω candidates, resulting in the signal distribution shown in figure 5.7 in red. The observed compatibility of the signal with zero outside of the signal region underlines the quality of the background description by the third-order polynomial.
- 3. The width and mass of the ω meson are extracted from the parameters of a Gaussian parameterization to the signal.
- 4. The raw number of ω mesons within a given p_T interval is calculated by subtracting the integrated background of the third-order polynomial within the signal region $(M_\omega \pm 3\sigma_\omega)$ from the summed up number of ω meson candidates in the same region. This leads to the raw yield of ω mesons shown in figure 5.9.

The previously described signal extraction is performed in two iterations. The first of these iterations is performed to define the signal region used for the exclusion

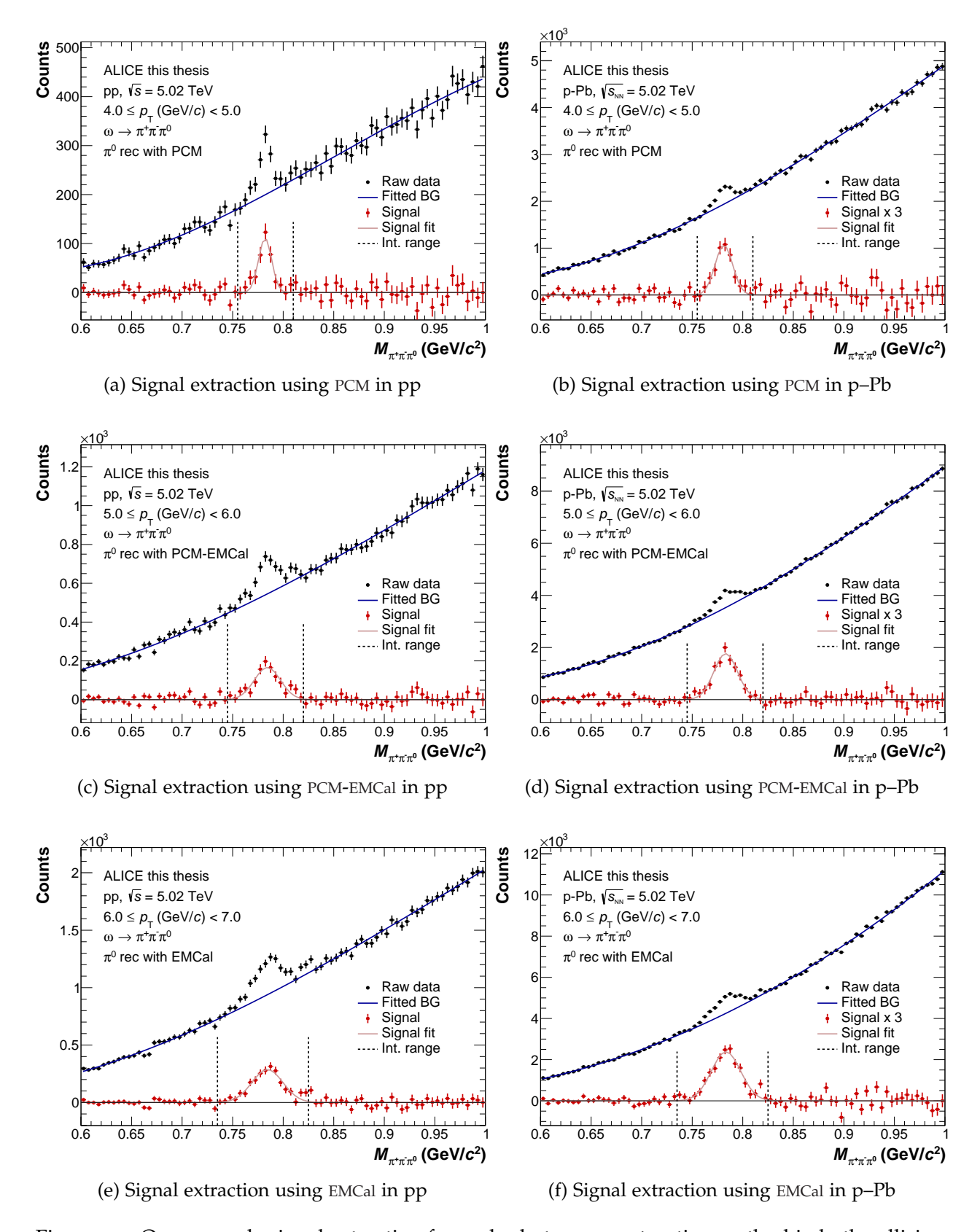


Figure 5.7: One example signal extraction for each photon reconstruction method in both collision systems. A compilation of all p_T bins in data and MC is shown in the appendix in figures A.6-A.11.

| | | | | $p_{\rm T}$ range | e (GeV/c) |
|-----------|----------------------------|--|-----------|-------------------|-----------|
| | M_{ω} (MeV/ c^2) | $\sigma_{\omega} \text{ (MeV/}c^2\text{)}$ | | pp | p–Pb |
| PCM | 782.5 ± 0.7 | 7.8 ± 0.7 | PCM | 1.8 – 10. | 2.2 – 12. |
| PCM-EMCal | 782.8 ± 0.6 | 12.2 ± 0.7 | PCM-EMCal | 2.2 – 12. | 2.6 – 16. |
| EMCal | 782.2 ± 0.5 | 14.0 ± 0.5 | EMCal | 2.6 – 20. | 3.2 – 20. |

Table 5.1: Extracted masses and widths defining the signal region

Table 5.2: Transerve momentum covered by the three π^0 reconstruction methods

during the parametrization and the integration of the signal for the second iteration. This first iteration uses a preliminary signal region of $M_{\omega}^{\rm PDG}\pm30\,{\rm MeV}/c^2$ to extract the mass and width of the ω meson for all $p_{\rm T}$ intervals, π^0 reconstruction methods, and both collision systems. Considering both the π^0 and the ω analyses at $\sqrt{s}=13\,{\rm TeV}$, with smaller statistical fluctuations, no large $p_{\rm T}$ dependence of the width or mass is expected in the covered $p_{\rm T}$ range [Koe20; Lue22]. Therefore, the extracted mass and width in all available $p_{\rm T}$ intervals and both collision systems were averaged for every reconstruction method. The mass and width extracted via this weighted average for the three reconstruction methods are compiled in table 5.1. These extracted properties are then used to define the signal region for the second iteration of the signal iteration as $M_{\omega}\pm3\sigma_{\omega}$ with variations to 2.5 and 3.5 σ for the systematic uncertainty estimation. The raw spectra from the second iteration of the signal extraction are shown in figure 5.9 and still have to be corrected for multiple effects like the efficiency and acceptance, as will be explained in section 6.1.

As the signal extraction introduces a few free parameters to be chosen by the analyzer, these are varied within a reasonable range to estimate the systematic uncertainties as described in section 6.3. This includes the description of the background using a fourth-order polynomial and restrictions of the fit range on the right ($m_{\pi^+\pi^-\pi^0} > 0.65\,\text{GeV/c}$) and on the left ($m_{\pi^+\pi^-\pi^0} < 0.95\,\text{GeV/c}$) side of the invariant mass distribution. Furthermore, variations were performed in which the signal region was not excluded but instead described by either a Gaussian with or with exponential tails on top of the polynomial describing the background.

The $p_{\rm T}$ range, in which the signal was extracted for a given collision system and reconstruction method was decided from the mass distributions shown in figures A.6 to A.11, where the main criteria were comparisons between the shape of the data and MC signal as well as the difference between the reconstructed and true ω signal in the MC. *True* signal in the context of this analysis corresponds to those ω mesons, that have been reconstructed in the MC and then validated to correspond to a simulated ω meson. The transverse momentum ranges, in which the signal extractions are performed for the different π^0 reconstruction methods, are shown in table 5.2.

The second iteration of the extraction enables the evaluation of the reconstructed p_T

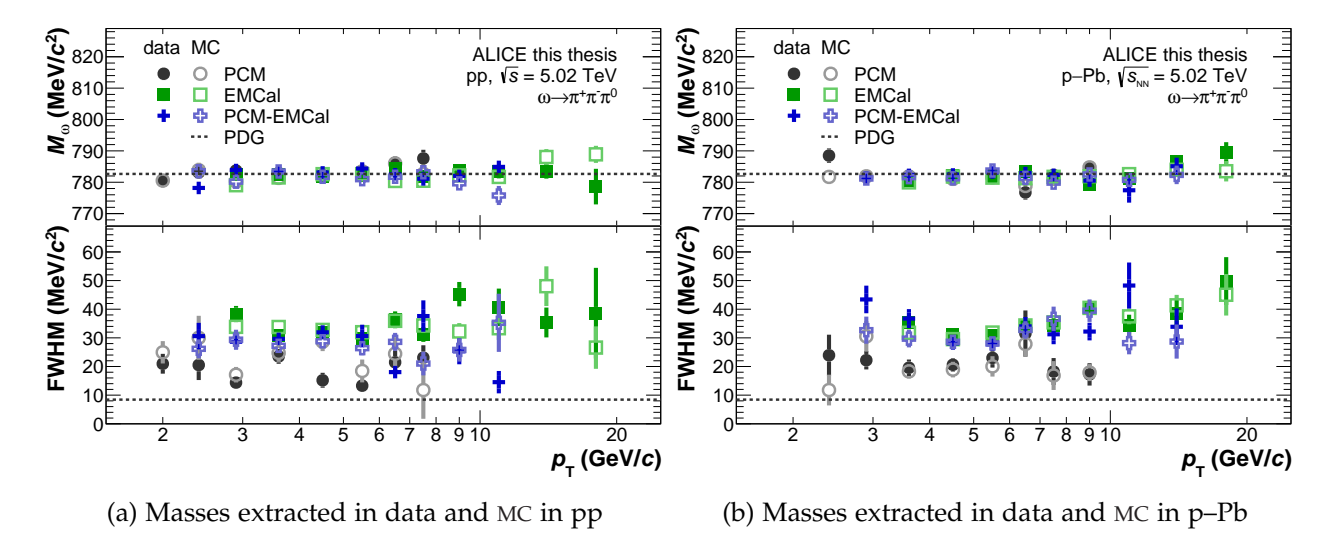


Figure 5.8: Reconstructed mass and width of the ω meson in data and MC

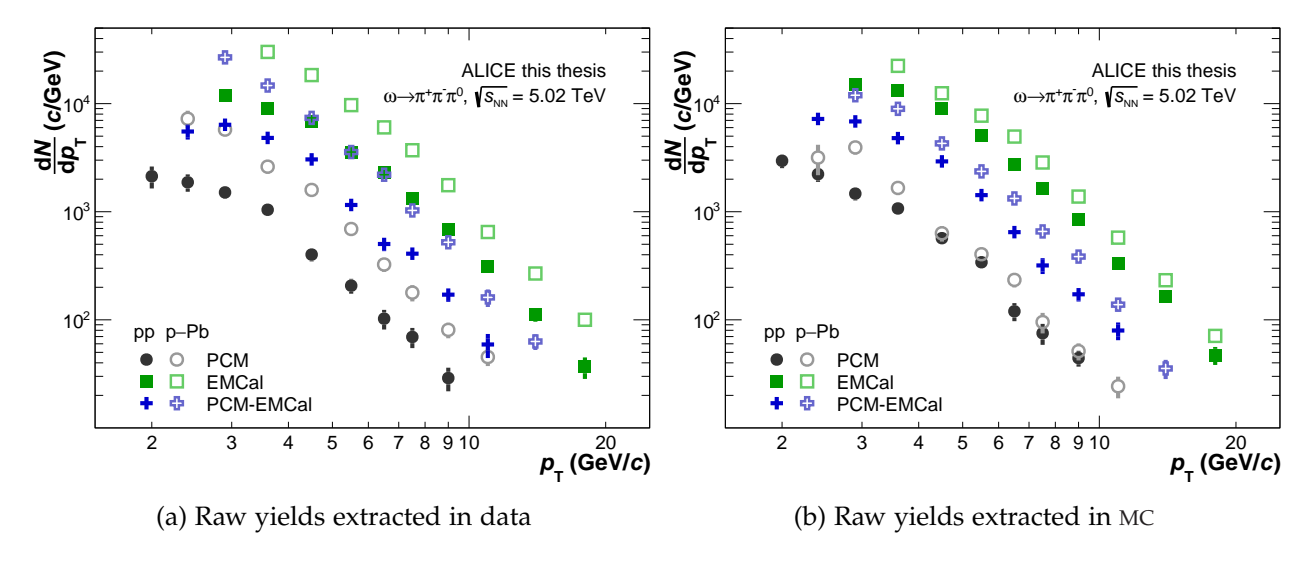


Figure 5.9: Raw ω meson yields extracted in data and MC for the three π^0 reconstruction methods

dependant properties of the ω mesons, as shown in figure 5.8. The reconstructed masses are all compatible with each other and also agree with the PDG value [Pdg22] within their statistical uncertainties. Especially the good agreement of the properties between data and MC is an important validation, as an accurate description of the extracted ω signal properties is a vital requirement for the efficiency correction, as described in the following section. As discussed in section 5.1, the reconstructed width is much larger than the natural width of the ω given in the literature. Furthermore, the expected ordering of widths is observed, with the EMCal reconstructing the largest width and PCM reconstructing the smallest width due to its superior resolution. While the extracted masses and widths serve as valuable cross-checks for the use of the MC to ensure the validity of the MC, the extracted raw yields shown in figure 5.9 represent the main result of this chapter, that will be further processed in the following chapter.

SIGNAL PROCESSING

This chapter describes how the raw yields from the previous section are corrected and combined to calculate the ω meson production cross section in pp and p-Pb collisions. The cross-sections are furthermore utilized to calculate both the nuclear modification factor $R_{\rm pPb}$ and the ω/π^0 production ratio.

6.1 SPECTRA CORRECTIONS

The raw yields of produced ω mesons N^{ω} , extracted in section 5.3 for the three reconstruction methods, can be converted into a Lorentz invariant cross-sections by applying the corrections described in the following equation, which will be explained in the subsequent paragraphs.

$$E\frac{d^{3}\sigma_{\omega}}{d^{3}p} = \frac{1}{\mathcal{L}_{\text{int}}} \frac{1}{2\pi p_{T}} \frac{1}{\mathcal{B}A\epsilon_{\text{true}}} \frac{N^{\omega}}{\Delta p_{T}\Delta y}$$
(6.1)

 \mathcal{L}_{INT} - INTEGRATED LUMINOSITY From the visible cross section $\sigma_{\text{INT}7}$ of the utilized INT7 MB trigger and the number of minimum bias events $N_{\text{evt.}}$, the inspected luminosity of the different reconstruction methods and collision systems can be calculated as $\mathcal{L}_{\text{int}} = \sigma_{\text{INT}7}/N_{\text{evt.}}$. The luminosities inspected in this analysis are listed in table 3.1.

 $\sigma_{\rm INT_7}$ - visible minimum bias cross section — The ALICE collaboration measured the visible cross-section of the INT7 MB trigger through Van der Meer scans and found the cross-sections to be (50.87 ± 0.92) mb in pp [Ach+18a], and (2.08 ± 0.07) b in p-Pb collisions [Abe+14a].

 $N_{\text{EVT.}}$ - Number of events The cross-section is normalized with the number of recorded MB events $N_{\text{evt.}}$, which is corrected for events in which no vertex is reconstructed, as described by equation 3.2.

 $2\pi\Delta y$ - solid angle. The normalization toward a Lorentz invariant cross-section includes the division by the solid angle, in which ω mesons are generated in the MC simulations. 2π represents the full ϕ coverage and Δy the rapidity range, which for this analysis is defined in the lab system as $|y_{\rm lab}| < 0.85$ resulting in $\Delta y = 1.7$.

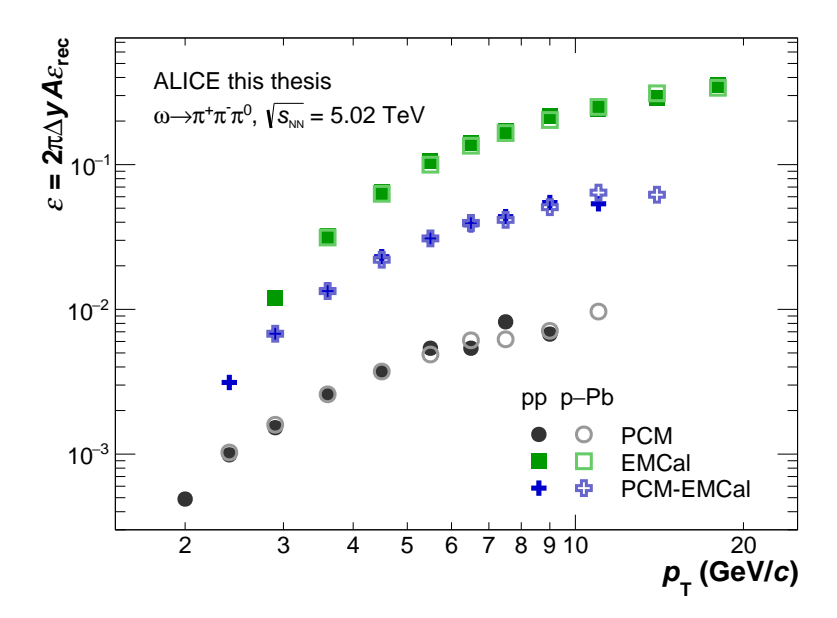


Figure 6.1: Total correction factors ϵ including acceptance A and true efficiency ϵ_{true}

 $p_{\rm T}\Delta p_{\rm T}$ - Transverse momentum The raw yields are normalized by the width of each extracted $p_{\rm T}$ interval $\Delta p_{\rm T}$, as well as the $p_{\rm T}$ of the respective interval itself.

 ${\cal B}$ - Branching ratio To take into account that not all ω mesons decay in the three pion decay channel and not all neutral pions then decay into two photons, the yield is divided by the branching ratio of the full decay $\omega \to \pi^+\pi^-\gamma\gamma$, which is calculated as the product of the two individual branching ratios:

$$\mathcal{B}(\omega\to\pi^+\pi^-\gamma\gamma)=\mathcal{B}(\omega\to\pi^+\pi^-\pi^0)\times\mathcal{B}(\pi^0\to\gamma\gamma)=(88.15\pm0.69)\,\%\text{ [Pdg22]}.$$

A - ACCEPTANCE The acceptance A quantifies the spatial coverage of the detectors. It is calculated via MC simulations as the ratio of ω mesons, whose decay products hit the detectors, to all ω mesons that were generated within $|y_{lab}| < 0.85$.

 ϵ_{TRUE} - EFFICIENCY The efficiency accounts for losses in the signal extraction, detector efficiencies, or signal losses from the applied cuts. It is defined as the ratio of reconstructed ω mesons to those whose decay products hit the detectors. The reconstruction efficiency $\epsilon_{\text{rec.}}$ is calculated by extracting a signal in the MC and comparing the resulting raw yield (see figure 5.9b) with the number of ω mesons that have been accepted (all decay products on the detectors). The statistical uncertainty on the final cross-section can, however, be reduced by using the so-called true efficiency ϵ_{true} . For its calculation, the set of MC-validated (true) ω mesons are directly integrated without performing a background fit or subtraction, removing the uncertainties coming from the combinatoric background. This reduction of the statistical uncertainties is only viable if the true and reconstruction efficiency agree within their uncertainties, which also speaks for a robust signal extraction. Figure 6.2 shows the two efficiencies and their agreement, which motivates the use of

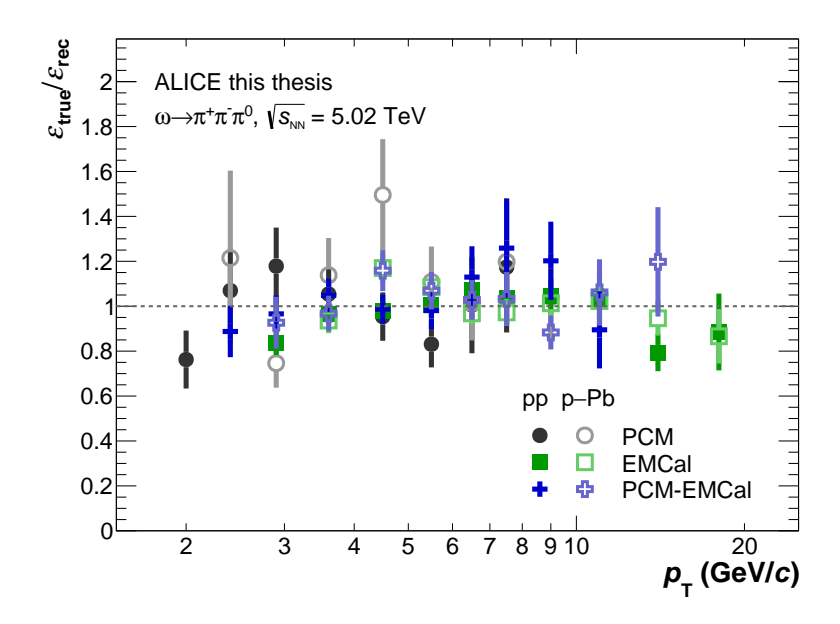


Figure 6.2: Ratio of the true efficiency ϵ_{true} to the reconstruction efficiency ϵ_{rec}

the true efficiency. To account for possible biases from the use of the true efficiency, correction of the spectra using the reconstruction efficiency is used in the estimation of the systematic uncertainties, as described in section 6.3.

The combined correction factor ϵ of acceptance, efficiency, and solid angle normalization can be seen in figure 6.1. While the factors are similar for the different collision systems, they differ drastically between different photon reconstruction methods. This is mainly because, for each photon reconstructed using PCM, the efficiency is reduced by the conversion probability of around 8.5%.

6.2 CALCULATION OF THE NUCLEAR MODIFICATION FACTOR

As introduced in section 1.3, the nuclear modification factor R_{pPb} quantifies the modification of particle production through the following equation:

$$R_{\rm pPb} = \frac{1}{A_{\rm Pb}} \frac{\mathrm{d}^2 \sigma_{\rm pPb} / \mathrm{d} p_{\rm T} \mathrm{d} y}{\mathrm{d}^2 \sigma_{\rm pp} / \mathrm{d} p_{\rm T} \mathrm{d} y}, \tag{6.2}$$

where $A_{\rm Pb}=208$ is the nuclear mass number of lead, and ${\rm d}^2\sigma_{\rm x}/{\rm d}p_{\rm T}{\rm d}y$ corresponds to the production cross-sections derived in the previous section. In order to compare particle production in this way, the production cross-sections have to not only originate from collisions with the same center of mass energy $\sqrt{s_{\rm NN}}=5.02$ TeV, but crucially, they are also required to cover the same rapidity interval in their center of mass system. While the center of mass in pp collisions is stationary, corresponding to a rapidity of $y_{\rm cm}^{\rm pp}=0$, the center of mass in p-Pb collisions is not stationary, caused by the protons and lead ions being bent by the same magnetic field in the LHC, while having a different

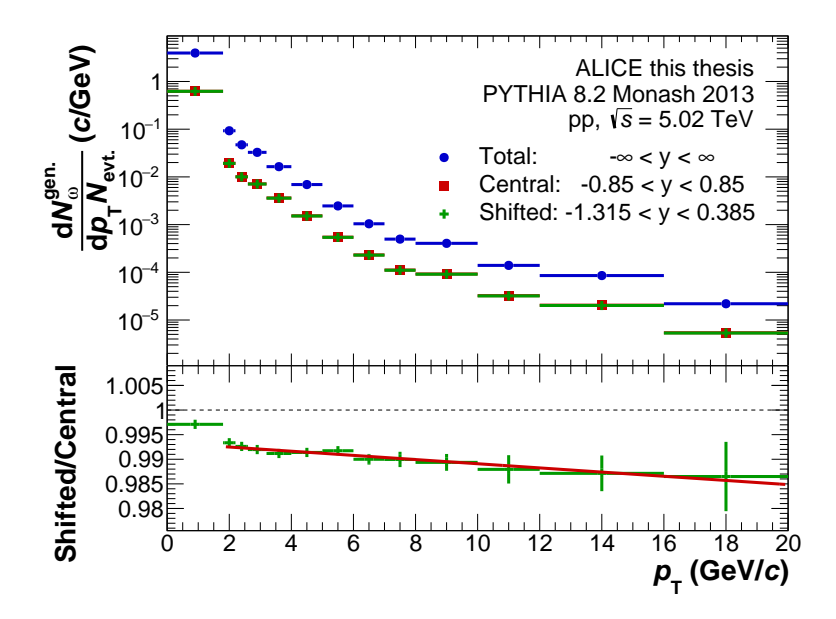


Figure 6.3: Simulated ω meson yields in different rapidity intervals in pp collisions at $\sqrt{s_{\rm NN}} = 5.02$ TeV using PYTHIA 8.2 with the Monash 2013 tune. The ratio in the bottom panel shows an approximately one percent decrease in the number of produced ω mesons for the shifted rapidity region covered in p–Pb collisions.

charge-to-mass ratio. This leads to a rapidity of $y_{\rm cm}$ = 0.465 [Ach+18b], and therefore the rapidity covered by ALICE in the lab frame of $|y_{\rm lab}|$ < 0.85 corresponds to a rapidity coverage of $-1.315 < y_{\rm cm} < 0.385$ in the center of mass system of a p-Pb collision. When comparing the two cross sections in a $R_{\rm pPb}$, this different measurement region has to be accounted for and corrected.

This is done using a PYTHIA 8.2 MC Simulation with the Monash 2013 tune. 2 billion pp events were simulated, and the number of ω mesons in the central and the shifted rapidity region were counted. The total yield integrated over the full rapidity, as well as the yield in the two rapidity regions, is shown in figure 6.3. The total yield is around five times larger than the yield in both the central and shifted rapidity regions. To examine the difference between these very similar yields, the lower panel shows the ratio of ω mesons produced in the shifted rapidity region to those in the central region. A decrease in the number of produced ω mesons is observed in the more forward direction by around 1%. The ratio was parameterized using a linear function in the $p_{\rm T}$ region used for the ω analysis in pp collisions. The decrease in the number of produced mesons for the shifted rapidities is similar in magnitude to the one in the π^0 -analysis at $\sqrt{s_{\rm NN}} = 5.02$ TeV, which also sees an increasing effect with rising $p_{\rm T}$ [Ach+18b].

This linear fit function is used to correct the pp cross-sections in order to shift it to the same rapidity region as the p-Pb measurement and enable the comparison between the two through the R_{pPb} , as described by equation 6.2.

6.3 SYSTEMATIC UNCERTAINTIES

Statistical uncertainties of counted values N are estimated by their square root \sqrt{N} , following the central limit theorem and assuming an underlying Poisson distribution.

Systematic uncertainties, on the other hand, stem from the inherent effects of the detector or the analysis itself and must be carefully estimated on a case-to-case basis. Certain sources of systematic uncertainty only affect specific π^0 reconstruction methods, such as the minimum cluster energy of the EMCal, which leaves the ω measurement using PCM unaffected. Furthermore, some uncertainties do not impact a specific type of resulting spectrum, such as the branching ratio uncertainty canceling out in calculating the nuclear modification factor. For the total systematic uncertainty of a given reconstruction method, the contributions by all sources relevant to the respective method and spectrum are added in quadrature, as they are assumed to be uncorrelated. The following paragraphs outline sources of systematic uncertainty and are grouped within three sections, which separate the three main methods of estimating these uncertainties.

6.3.1 *p*_T *Independent Uncertainties*

This section describes uncertainty sources that are independent of the transverse momentum and which were adopted from dedicated analyses on the respective correction, which induces the uncertainty.

BRANCHING RATIO This analysis only includes ω mesons that decay into three pions with the π^0 then decaying further into two photons. The measured yields are, therefore, scaled by the inverse branching ratios of the two decays, as described in section 6.1. The two branching ratios published by the PDG, however, come with relative uncertainties of 0.7 % and 0.034 % for the ω and π^0 decay [Pdg22]. While the uncertainty from the π^0 decay is almost negligible, the branching ratios introduce a combined uncertainty of 0.7 % in all $p_{\rm T}$ intervals and reconstruction methods. As this uncertainty is fully correlated between pp and p-Pb, it does not propagate into the $R_{\rm pPb}$.

CROSS SECTION The visible MB cross sections used to calculate the ω production cross sections from the yields, as introduced in section 6.1, also come with measurement uncertainties. The pp measurement reports a relative uncertainty of 4.4% [Ach+18a] and the p-Pb measurement a relative uncertainty of 3.4% [Abe+14a]. Therefore, the measured ω meson cross sections inherit these respective cross-section uncertainties, while they cancel out in the ω/π^0 ratios. For the calculation of the nuclear modification factor, the two uncertainties are added in quadrature.

| Method | Uncertainty (%) | | | |
|-----------|-----------------|------------|-------|--|
| Metriou | γ_1 | γ_2 | Total | |
| PCM | 2.5 | 2.5 | 5 | |
| PCM-EMCal | 2.5 | 2.12 | 3.28 | |
| EMCal | 2.12 | 2.12 | 4.24 | |

Table 6.1: Relative systematic uncertainty due to the material budget [Ach+23; Ach+18c]

MATERIAL BUDGET The implementation of the material within the ALICE experiment in the GEANT 3 simulation is crucial for the accurate description of interactions between the decay products and the detector material. Therefore, discrepancies in the amount or composition of this material have to be accounted for. To better estimate the material relevant for PCM photons, the ALICE collaboration developed a data-driven approach using Material Budget Weights (MBWs). This analysis quotes the remaining uncertainty per conversion photon to be 2.5 % [Ach+23]. Around 50 % of photons convert before reaching the EMCal, predominantly in the TRD and TOF. In an analysis of π^0 production of a dataset at $\sqrt{s} = 8$ TeV, only parts of the TRD were installed, allowing for the influence of the TRD material on the π^0 reconstruction efficiency to be studied. This study quotes the TRD material uncertainty to be around 1.5 %, with the uncertainty of the TOF assumed to be similar [Ach+18c]. As these two material uncertainties are uncorrelated, the total material budget uncertainty per EMCal photon is calculated as the quadratic sum to be 2.12%. As for each ω meson, two photons are reconstructed, the systematic uncertainty caused by the material budget is a sum of the uncertainties of the two photons used for the respective reconstruction method. This is shown in table 6.1, where the uncertainty for π^{0} 's reconstructed with PCM and EMCal is twice that of each photon, as the uncertainty of both photons is fully correlated. The total material budget uncertainty of PCM-EMCal on the other hand, assumes the two different material budget uncertainties to be uncorrelated to each other and is therefore calculated as a quadratic sum.

RAPIDITY SHIFT The rapidity shift, as explained in section 6.2 shifts the $R_{\rm pPb}$ by approximately 1%. From the statistical uncertainty of the parametrization in figure 6.3 and the systematic uncertainty that comes from the choice of the fit function, the relative uncertainty of this shift is estimated to be 10%. This results in a total uncertainty contribution of 0.1% to the nuclear modification factor $R_{\rm pPb}$.

| Setting | Standard | Variation 1 | Variation 2 |
|-------------------------------------|-----------|----------------|-------------------|
| Resolution correction | Sub λ | Sub π^0 | |
| Background description | Pol3 | Pol4 | |
| Parametrization range (GeV/ c^2) | [0.6, 1] | [0.6, 0.95] | [0.65, 1] |
| Signal description | Exclusion | Gaus | Gaus + exp. tails |
| Integration range | 3 σ | 2.5σ | 3.5σ |
| Efficiency | True | Reconstruction | |

Table 6.2: Signal extraction settings and variations used to estimate the systematic uncertainties

6.3.2 Uncertainties from the Signal Extraction

The signal extraction described in section 5.3 contains free parameters, potentially impacting the resulting spectra, but could have been chosen differently by another analyzer. These free parameters are the used resolution correction, the background and signal descriptions, the parametrization and integration range, as well as the use of the true efficiency. These parameters are listed in table 6.2, together with the standard value that was used in this analysis, as well as one or two reasonable variations. The two previous ω meson analyses within the ALICE collaboration [Ach+20; Lü23] both cite the signal extraction as their dominant source of uncertainty for all reconstruction methods. In an effort to estimate this source of systematic uncertainty more precisely, a more sophisticated procedure was chosen compared to previous neutral meson analyses in ALICE. In contrast to these previous analyses, the variations listed in table 6.2 were, for this reason, not only performed individually but instead, the signal extraction was carried out for all combinations of reasonable settings. This new approach of combining different variations comes with two main advantages. The first is that possible correlations between the variations are now included, such as a variation of the signal and the background description simultaneously, which could reduce or enhance the difference. Additionally, these combinations of variations allow for the extraction of $2 \times 2 \times 3 \times 3 \times 3 \times 2 = 216$ yields and R_{pPb} 's, instead of the eight independent variations performed in previous analyses [Ach+20; Lü23]. This can mitigate the effect of statistical fluctuations on individual extracted spectra, which would otherwise propagate statistical uncertainty to the extracted systematic uncertainties.

In order to include only results from meaningful variations of the signal extraction parameters, they were investigated for possible unsuccessful parametrizations before including them in the calculation of the systematic uncertainty. For this purpose, every variation must have a $\chi^2_{max}/ndf < 2.5$ for the background parametrization for all reconstruction methods and both collision systems, thereby ensuring a stable analysis in all

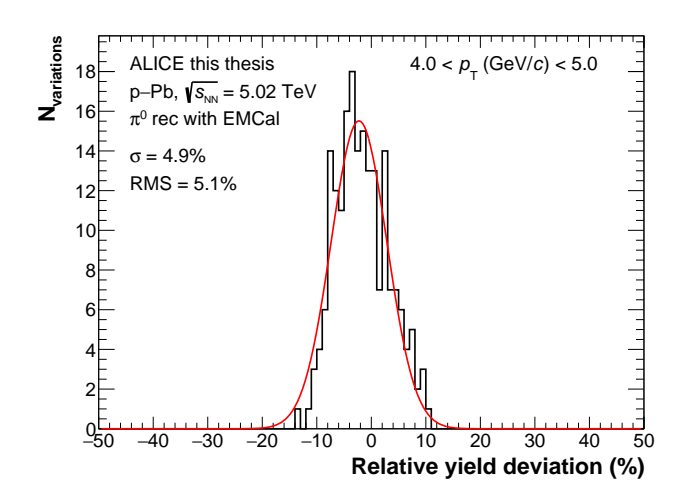


Figure 6.4: Relative deviations of the signal extraction variations listed in table 6.2 with the EMCal in p-Pb collisions

cases. This requirement is fulfilled by 198 of the variations, while the 18 variations that do not meet the requirement all have a $\chi^2/ndf > 5$ and were therefore excluded. For the remaining 198 variations, the yield and the $R_{\rm pPb}$ are extracted, and subsequently, their deviation to the relative deviation to the *standard* selection is calculated. An example distribution of the deviations of the signal extraction variations for the EMCal reconstruction in p-Pb is shown in figure 6.4 for $4 < p_{\rm T} (GeV/c) < 5$. The systematic uncertainty caused by the signal extraction corresponds to the spread of the deviation distribution, which is found to be approximately normally distributed.

The relative deviation distribution can be parameterized by a Gaussian function, whose standard deviation σ then quantifies the width of the underlying distribution. However, this method only describes the width of the distribution but neglects a possible systematic offset of the mean and, therefore, underestimates the total systematic uncertainty. Using the Root Mean Square Value (RMS), on the other hand, describes the width of a distribution while considering a possible offset of the mean. The RMS is therefore calculated individually for all $p_{\rm T}$ intervals and then smoothed over the $p_{\rm T}$ region using the 353QH algorithm [Fri] in order to further reduce the impact of statistical fluctuations. This was done for the yield and the $R_{\rm pPb}$ individually, as this greatly reduced the systematic uncertainty to the $R_{\rm pPb}$ by removing effects from correlated uncertainties affecting the yield equally in both collision systems.

In summary, this new approach estimates the systematic uncertainty caused by the signal extraction by considering all combinations of possible variations in the signal extraction, thereby not only considering cross-correlations but also mitigating the propagation of statistical fluctuations into the extracted systematic uncertainty. It has, therefore, also been adapted in other analyses, such as a measurement of neutral mesons in jets [Kö23], and the first extraction of the η' meson in ALICE [Gli].

6.3.3 Uncertainties from the Selection Criteria

The selection of the applied cuts explained in chapter 4 comes with systematic uncertainties that are estimated by varying these cuts within a reasonable range and investigating the changes in the spectra that these variations cause. Table 6.3 shows the cuts that were varied for systematic uncertainty extraction and the respective values that they were varied to. Four main groups of systematic uncertainties were identified. They describe the uncertainty due to the selection of the charged pion, the neutral pion, conversion photons (PCM), and cluster photons (EMCal). The systematic uncertainty coming from the individual cuts is then estimated by taking the difference between the maximum and minimum value (yield or R_{pPb}) and dividing it by 2. This corresponds to the maximum deviation averaged in both directions. If only one variation was performed, the difference between the standard and the variation value was divided by $\sqrt{2}$, as in previous neutral meson analyses [Lue22]. After the systematic uncertainty of each source has been estimated in each $p_{\rm T}$ interval, the relative uncertainties are smoothed utilizing the 353QH algorithm [Fri], as done for the signal extraction uncertainty, to mitigate statistical fluctuations. Some variations describing much stricter requirements than the standard settings drastically decrease the sample of ω meson candidates and are, therefore, substantially influenced by statistical fluctuations. The cut variations most affected by such statistical fluctuations are explained in the following paragraphs, including the methods used to disentangle the systematic uncertainties from these statistical fluctuations.

Number of EMCAL cells Requiring a certain number of cells for a cluster in the EMCal drastically reduces the available ω candidates (\approx 30 %) and therefore induces large statistical fluctuations. Especially in $p_{\rm T}$ intervals, where the statistical uncertainties are relatively large, the extracted systematic uncertainty is expected to be contaminated by these statistical fluctuations. To better estimate this uncertainty, the π^0 analysis at $\sqrt{s}=13$ TeV was consulted [Koe20], where the statistical uncertainties are much smaller both because of the larger dataset and the better signal-to-background ratio for neutral pions. Therefore, the $N_{\rm cell}$ uncertainty is expected to be much less affected by statistical fluctuations. There, the systematic uncertainty of this cut was found to be less than 2% in the entire $p_{\rm T}$ region, which is much larger than the one covered by this ω analysis. Since the uncertainty on the π^0 yield is expected to propagate directly to the yield/ $R_{\rm pA}$ of the ω meson, this upper limit of 2% is assumed to cover the $N_{\rm cell}$ uncertainty in this analysis for the entire $p_{\rm T}$ range.

 $m_{\gamma\gamma}$ SELECTION WINDOW Variations of the mass window, in which π^0 candidates are selected for the ω reconstruction, also cause large statistical fluctuations since these variations have a significant impact on the amount of ω candidates that enter the signal extraction. To disentangle these fluctuations from any possible underlying systematic

 π^{\pm} cuts π^0 cuts Cluster photon cuts Conversion photon cuts $E_{\mathbf{cluster}}$ Fine tuning scheme Quantity TOF (when available) TPC requirement ITS requirement Asymmetry cos(pointing angle)> π rejection **Electron PID** TPC cls./findable cls. > Track $p_{\rm T} >$ NCell ≥ **Exotic clusters** Track matching $t_{
m cluster}$ (ns) TPC PID $n\sigma$ < $|\Delta\eta|<$ selection window $q_{\rm T} <$ DCA_{xy} : < $q_{\rm T} <$ E/p <DCAz: < $|\Delta\phi|$ < $\chi^2/ndf <$ EMCal: PCM-EMCal: $n\sigma$ < PCM: $|\psi_{\mathrm{pair}}| <$ $n\sigma <$ $n\sigma <$ 2.4 cm 2 2.5 $0.125 \, p_{
m T}$ $3.2\,cm$ 0.8560% 97% Standard $n\sigma^{\pi} < 5 \mid\mid n\sigma^{K/p} > 3$ min 80 clusters 1st or 2nd SPD cluster | + min 3 clusters 55 $0.055 \cdot \exp(0.3 \cdot \chi^2)$ $0.05\,\text{GeV/}c$ 50 MeV/c $0.1 < M_{02} < 0.7$ 0.7 GeV 1.75 c $0.015 + (p_{\rm T} + 3.65)^{-2}$ $0.010 + (p_{\rm T} + 4.07)^{-2.5}$ CCRF+CRF 100 MeV/c $850 \, \text{MeV}/c^2$ $-3 < n\sigma < 4$ $-20 < t_{\rm cluster} < 25$ $0.015 + (p_{\rm T} + 3.65)^{-2}$ 0.75 0.05 2 + no shared clusters $\alpha < 0.75$ 1.5 2 55 $0.11\,p_{
m T}$ 35% $0.1 < M_{02} < 0.5$ 2 (EMC corrected) $0.6\,\mathrm{GeV}$ 2.0 c $0.010 + (p_{\rm T} + 4.07)^{-2.5}$ CCRF $800\,\mathrm{MeV/c^2}$ 75 MeV/c $40\,\mathrm{MeV/}c$ Variation 1 $0.03\,\text{GeV/}c$ $n\sigma > 0$ $-4 < n\sigma < 5$ $-30 < t_{\rm cluster}$ ≤ 35 ယ 0.88 $0.25\,p_{
m T}$ $0.8\,\mathrm{GeV}$ 1.5 c $0.015 + (p_{\rm T} + 3.65)^{-2}$ $0.010 + (p_{\rm T} + 4.07)^{-2.5}$ 70% $0.1 < M_{02} < 1.0$ 2 (PCM-EMC corrected) 95% $p_{\rm T}$ dep 3 $\alpha < 0.8$ 2.5 $0.1 \cdot (1 - \chi^2/30)$ CRF $825 \, \text{MeV}/c^2$ $n\sigma^{\pi} < 3 \parallel n\sigma^{K/p} > 3$ $p_{\rm T}$ dep 3 30 $0.04\,\text{GeV/}c$ $75\,\mathrm{MeV}/c$ 125 MeV/ $n\sigma > 2$ Variation 2 $-2.5 < n\sigma < 4$ $-12.5 < t_{\text{cluster}}$ <13 3.5 $0.5\,cm$ $0.5\,cm$ ယ 3.5 3.5 $0.3\,p_{
m T}$ $0.015 + (p_{\rm T} + 3.65)^{-2}$ $n\sigma^\pi < 7$ $\alpha < 0.85$ $0.05 \cdot (1 - \chi^2/20)$ $0.010 + (p_{\rm T} + 4.07)^{-2.5}$ $97\% \& E_{\text{cluster}} > 3 \text{ GeV}$ 150 MeV/c $0.045\,\text{GeV/}c$ $875 \, \text{MeV}/c^2$ 100 MeV/c Variation 3 $-50 < t_{
m cluster}$ **<50** $0.015 + (p_{\rm T} + 3.78)^{-2}$ $0.010 + (p_{\rm T} + 4.37)^{-2.5}$ $0.14\,p_{
m T}$ $900\,\mathrm{MeV/c^2}$ 3.5 $0.065 \cdot \exp(0.18 \cdot \chi^2)$ 1.75 c0.06 GeV/c Variation 4 $-20 < t_{
m cluster}$ <30 $0.015 + (p_{\rm T} + 3.54)^{-2}$ $0.010 + (p_{\rm T} + 3.82)^{-2.5}$ $0.075 \cdot \exp\left(0.2 \cdot \chi^2\right)$ $0.16 p_{\mathrm{T}}$ 1.75 c0.7 GeV/c Variation 5

Table 6.3: Overview of the cuts used in this analysis and the variations used to estimate the systematic uncertainties

effect, the absolute values of the relative deviations from the standard are averaged using a constant parametrization, taking into consideration the statistical uncertainties of the individual variations. The value of this parametrization is then applied to the entire covered $p_{\rm T}$ range, as no significant $p_{\rm T}$ dependence is expected, considering previous neutral meson analyses [Koe22; Lue22].

NUMBER OF ITS CLUSTERS Changing the requirement on the ITS clusters also introduces a sizeable statistical component. Like with the $m_{\gamma\gamma}$ selection window, this systematic uncertainty was extracted by averaging the absolute values of the relative deviations using a constant parametrization. Since only one variation was performed, the systematic uncertainty in each bin corresponds to the value of this constant divided by $\sqrt{2}$.

Through the methods outlined above, the impact of 28 sources of uncertainty is estimated. Out of these, all relevant uncertainties for a given reconstruction method were added in quadrature, as the individual uncertainties are all assumed to be uncorrelated. The relative systematic uncertainty of the different sources are shown in figure 6.5 for the example of the cross-section extracted in p-Pb using PCM-EMCal. The extracted systematic uncertainties for the different reconstruction methods and collision systems are compiled in figures A.4 and A.5 for the cross-section and the $R_{\rm pPb}$. For all reconstruction methods and in both collision systems, the signal extraction uncertainty is observed to be the dominant source of systematic uncertainty. This uncertainty is caused by the small signal-to-background ratio, thereby motivating studies into the smeared signal and large combinatorial background, as presented in chapter 5.

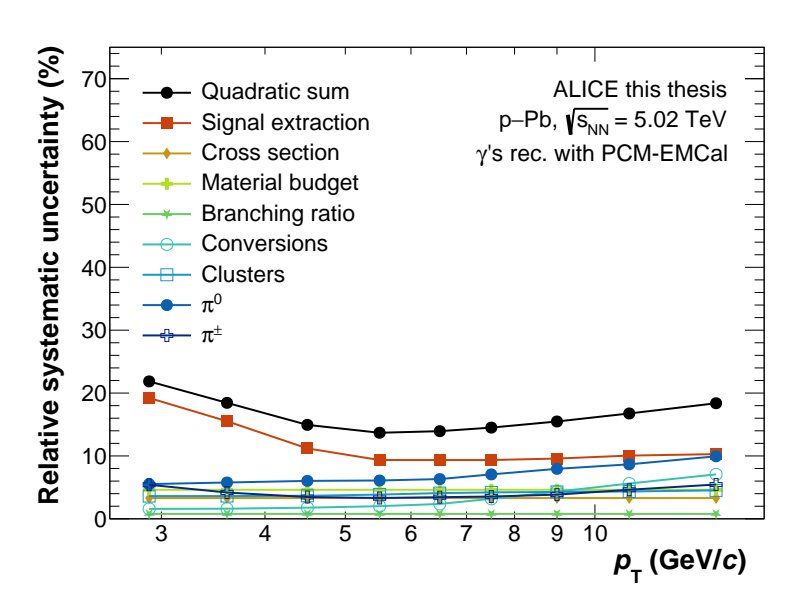
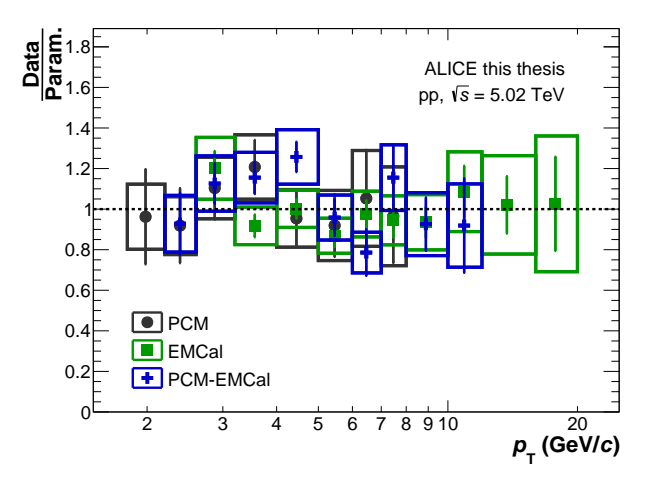
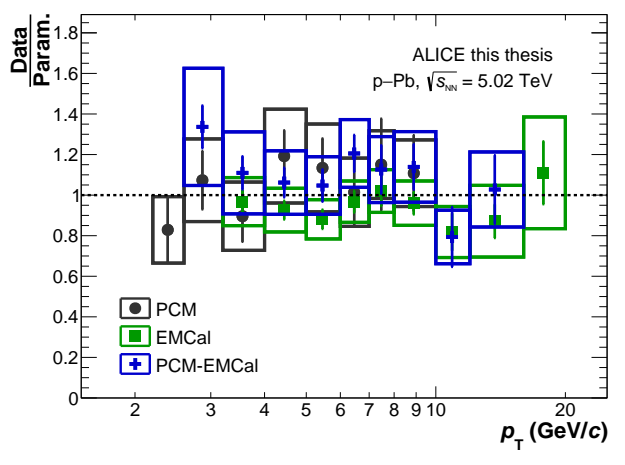


Figure 6.5: Relative systematic uncertainties of different sources for the cross-section in p-Pb measured using PCM-EMCal

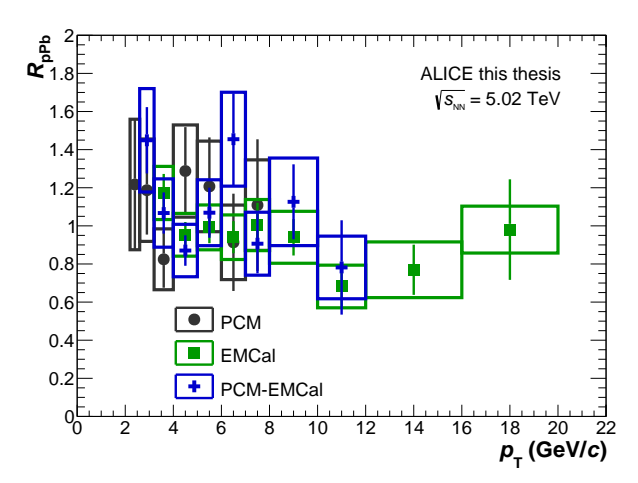
6.4 COMBINATION OF RECONSTRUCTION METHODS

As presented in the previous sections, the production cross sections and nuclear modification factor have been extracted using three partially independent reconstruction methods. This section describes how these spectra are combined, reducing their systematic and statistical uncertainties. Before combining the spectra from the different reconstruction methods, comparing them and ensuring their compatibility is essential. This comparison is shown in figure 6.6, where the extracted cross-sections are shown, divided by a combined Tsallis parametrization of all methods for better comparison. The three independently extracted cross-sections and nuclear modification factors exhibit agreement within their respective statistical and systematic uncertainties.





- (a) Ratios of the cross sections to a combined Tsallis parametrization in pp collisions
- (b) Ratios of the cross sections to a combined Tsallis parametrization in p-Pb collisions



(c) Nuclear modification factor R_{pPb} extracted using the different π^0 reconstruction methods

Figure 6.6: Compilation of the cross-sections and nuclear modification factors extracted using the three partially independent reconstruction methods

Following this assurance that all methods are compatible with one another, they are combined using the BLUE method, following [Lis17]. The data point $\theta_i(p_T)$, where θ is a placeholder for the yield, cross-section, or nuclear modification factor measured using method i, can be written as

$$\theta_i(p_{\rm T}) = \hat{\theta}_i(p_{\rm T}) \pm \sigma_i^{stat}(p_{\rm T})\hat{\theta}_i(p_{\rm T}) \pm \sigma_i^{sys}(p_{\rm T})\hat{\theta}_i(p_{\rm T}). \tag{6.3}$$

In this and all following equations, any uncertainty σ is to be understood as relative uncertainties. In order to perform the combination of $\theta_i(p_T)$, the correlation $\rho_{ij}(p_T)$ between the uncertainties of method i from method j has to be calculated:

$$\rho_{ij}(p_{\mathrm{T}}) = \frac{\sqrt{\left(\sigma_i^{tot}(p_{\mathrm{T}})\right)^2 - \left(\sigma_{ij}^{unc}(p_{\mathrm{T}})\right)^2}}{\sigma_i^{tot}(p_{\mathrm{T}})} \tag{6.4}$$

Here, the uncorrelated uncertainty σ_{ij}^{unc} between method i and j is subtracted from the total uncertainty of method i: $\sigma_i^{tot} = \sqrt{\left(\sigma_i^{stat}\right)^2 + \left(\sigma_i^{sys}\right)^2}$. The uncorrelated uncertainty σ_{ij}^{unc} is itself a quadratic sum of all contributions to the uncertainty of method i, that are not correlated to the uncertainties of method j:

$$\sigma_{ij}^{unc}(p_{\mathrm{T}}) = \sqrt{\sum_{x} \left[\left(1 - c_{ij}^{x} \right) \sigma_{i}^{x}(p_{\mathrm{T}}) \right]^{2}}.$$
 (6.5)

The $p_{\rm T}$ independent factor c_{ij}^x describes to what degree the uncertainty of group x of method i is correlated to that of method j. These correlation factors are summarized in figure 6.7 within 3×3 matrices for the different correlations. These correlations between the reconstruction methods for statistical uncertainties and the systematic uncertainty groups introduced in 6.3, are in the following discussed and assigned one of the correlation matrices given in figure 6.7.

Diagonal elements of the correlation matrices are always 1 since they represent the correlation of a method with itself. The off-diagonal elements contain the correlation between different methods and can differ for different uncertainty sources.

Statistical uncertainties between different methods are fully uncorrelated (6.7a) since no two reconstruction methods can detect the same ω meson.

Systematic uncertainties due to the signal extraction are also assumed to be fully uncorrelated (6.7a), since the energy resolution correction described in 5.1, as well as the background shape and signal to background ratio are very different between the reconstruction methods.

As the same cross-section is used for all reconstruction methods to derive the invariant ω meson cross-section from the yield, any systematic uncertainty from this scaling is fully correlated between the methods(6.7b).

The systematic uncertainty of the branching ratio is also fully correlated (6.7b) since they

$$c^{stat} = c^{extr} = c^{\pi^0} = \begin{pmatrix} 1 & 0 & 0 \\ 0 & 1 & 0 \\ 0 & 0 & 1 \end{pmatrix} \qquad c^{\sigma} = c^{\mathcal{B}} = c^{\mathcal{Y}} = c^{\pi^{\pm}} = \begin{pmatrix} 1 & 1 & 1 \\ 1 & 1 & 1 \\ 1 & 1 & 1 \end{pmatrix}$$
(a) Fully uncorrelated (b) Fully correlated
$$c^{mat} = \begin{pmatrix} 1 & 1 & 0 \\ 0.76 & 1 & 0.64 \\ 0 & 1 & 1 \end{pmatrix} \qquad c^{conv} = \begin{pmatrix} 1 & 1 & 0 \\ 1 & 1 & 0 \\ - & - & - \end{pmatrix} \qquad c^{calo} = \begin{pmatrix} - & - & - \\ 0 & 1 & 1 \\ 0 & 1 & 1 \end{pmatrix}$$
(c) Material budget (d) Conversions (e) Clusters

Figure 6.7: Correlation factors of the different uncertainty sources between the photon reconstruction methods. The source x uncertainty of method i (1 \triangleq PCM, 2 \triangleq PCM-EMCal, 3 \triangleq EMCal) is correlated to that of method j by c_{ij}^x .

all share the same decay channel and therefore branching ratio (uncertainty).

When calculating the nuclear modification factor, a rapidity shift has to be performed as discussed in 6.2. The associated systematic uncertainty estimated in 6.3 is the same for all reconstruction methods and, therefore, fully correlated (6.7b).

The final fully correlated (6.7b) source of uncertainty comes from the cut variations for the charged pions as the same charged pion selection criteria are used, independent of the photon reconstruction method.

The material budget uncertainties for both PCM and EMCal are fully correlated to the PCM-EMCal material budget uncertainty, as both photons used in the two individual methods are also used in the hybrid method. PCM and EMCal do not share any correlation for the material budget uncertainty since their respective uncertainties come from entirely different regions of the material, as described in 6.3. Only the inner material budget uncertainty fraction of PCM-EMCal is correlated to PCM. Therefore, the correlation factor c_{21} has to scale down the PCM-EMCal material budget uncertainty to the inner material budget uncertainty. The correlation is equal to the ratio of the inner material budget uncertainty (2.5%) to the total PCM-EMCal material budget uncertainty (3.28%): $c_{21} = 0.76$. Similarly, only the outer material budget uncertainty fraction of PCM-EMCal is correlated to EMCal. In this case the correlation factor c_{23} has to scale down the PCM-EMCal material budget uncertainty to the outer material budget uncertainty: $c_{23} = 0.64$ All of these correlation factors are summarized in matrix 6.7c.

For the systematic uncertainty from the conversion photon selection, the third row in the correlation matrix is not applicable since the EMCal-method has no conversion uncertainty. This is also the reason why the third column shows no correlation between PCM or PCM-EMCal from EMCal. The conversion uncertainty for PCM is however fully correlated

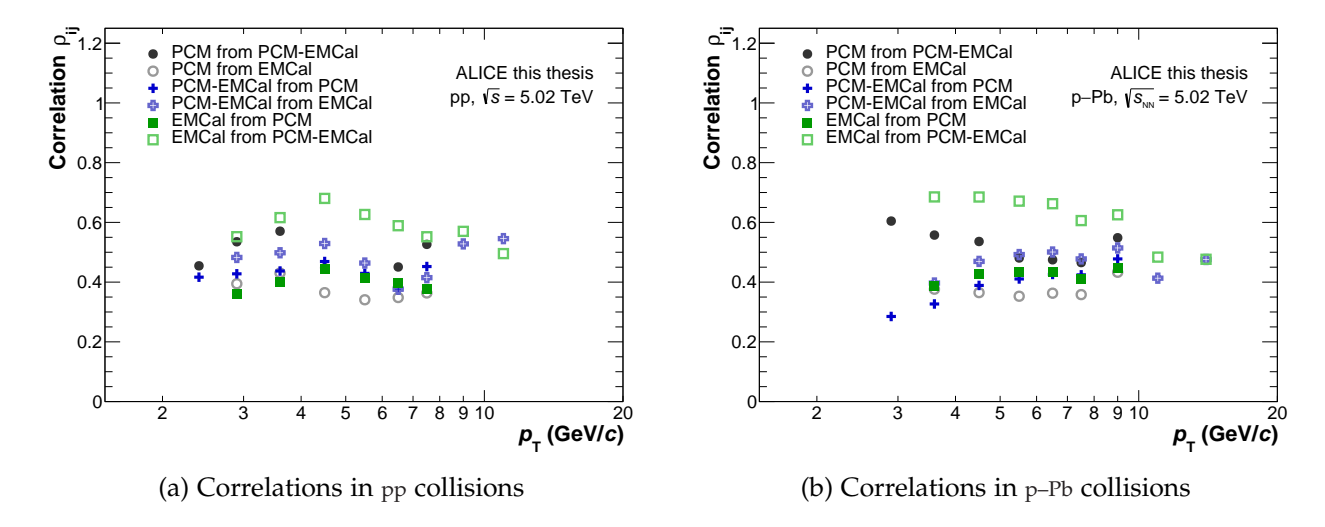


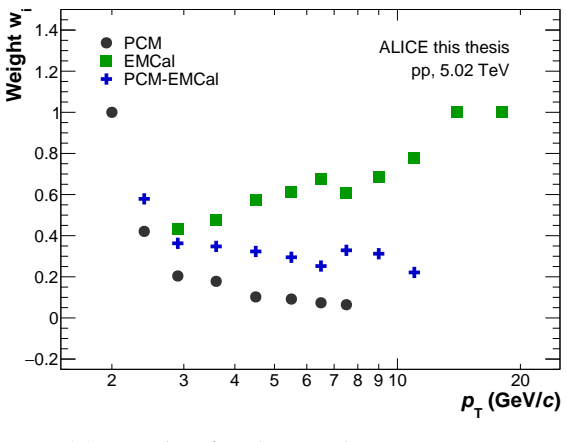
Figure 6.8: Correlations ρ_{ij} of the cross-section uncertainties between the different reconstruction methods

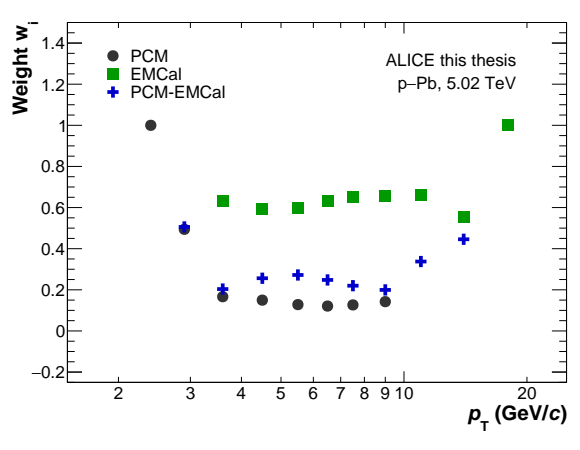
to that of PCM-EMCal and vice versa (6.7d).

The correlation matrix for the cluster uncertainties (6.7e) follows a similar pattern, only that here PCM does not contain the respective uncertainty, and therefore, the other two are not correlated to it. Here, the PCM-EMCal uncertainty is fully correlated to that of the EMCal method.

Finally, the correlation between systematic uncertainties from variations of the requirements for neutral pions is also assumed to be negligible (6.7a). This is because the drastically different energy resolutions of the different methods make the selection criteria for neutral pions, as described in 4.3, incomparable to one another.

The correlations ρ_{ij} between the cross-section measurements i and j, calculated from equations 6.4 and 6.5, using the systematic uncertainty composition as shown in figure A.4, are shown in figure 6.8. The strongest correlation is observed for the EMCal uncertainty from the PCM-EMCal uncertainty. This can be understood by looking at the correlation matrices in figure 6.7, which displays full correlation for this method combination ($c_{3,2}$), except for the fully uncorrelated uncertainties. But as these uncorrelated uncertainties are relatively small for the cross-section extracted with EMCal (see A.4), the correlation from PCM-EMCal, with which it shares many systematic uncertainty sources, is relatively large. One of the smallest correlations is the PCM from EMCal correlation, as the two methods share little common systematic uncertainties, and the PCM method comes with the largest statistical uncertainties. Overall, the correlations are between $0.4 \lesssim \rho_{ii}^{\omega} \lesssim 0.7$, which is comparatively small, when considering correlation factors in recent light neutral meson analyses of $ho_{ij}^{\pi^0} \sim$ 0.9 [Ach+22; Koe22]. This smaller correlation is caused by the uncertainty composition of this analysis, which is dominated by the statistical and signal extraction uncertainty, both of which are uncorrelated between different reconstruction methods. The comparatively small correlation between the reconstruction methods ob-





(a) Weights for the combination in pp

(b) Weights for the combination in p-Pb

Figure 6.9: Weights of the reconstruction methods used to combine the cross-sections, calculated from equation 6.7 using the correlations shown in figure 6.8

served in this analysis allows their combination to reduce the total uncertainties of the measurement. Using the correlations ρ_{ij} the covariance matrix V can be derived:

$$V_{ij} = \sigma_i \sigma_j \rho_{ij} \rho_{ji} / (\hat{\theta}_i \hat{\theta}_j)$$
(6.6)

The dimension of the covariance matrix in each p_T interval is equal to the number of methods used in the respective p_T region. The weights \vec{w} , with which the methods are weighted in the combination, can be calculated from the covariance matrix:

$$\vec{w} = \frac{V^{-1}\vec{u}}{\vec{u}^T V \vec{u}'} \tag{6.7}$$

where \vec{u} is a vector with all elements equal to unity. The calculated weights of the cross sections from the different reconstruction methods in the two collision systems are shown in figure 6.9. For both collision systems, the EMCal reconstruction method has the largest weight in most of the p_T region. Only at very low p_T , where the reconstruction with the EMCal is found not to be viable, do the PCM and PCM-EMCal method gain significant weight. Similar weights were extracted for the combination of yields and nuclear modification factors caused by only minor differences between the correlations and slightly different sources of systematic uncertainties. From these weights, the combined value $\hat{\theta}$ (cross-section, yield or $R_{\rm pPb}$) and its combined uncertainty $\sigma_{\hat{\theta}}$ can be derived using the following equations.

$$\hat{\theta} = \sum_{i=1}^{n} w_i \hat{\theta}_i \qquad \qquad \sigma_{\hat{\theta}} = \hat{\theta} \sqrt{\vec{w}^T V \vec{w}}$$
 (6.8)

This combined total uncertainty can be split into statistical and systematic uncertainty by calculating the fully uncorrelated statistical uncertainty and then subtracting it from the total uncertainty to receive the combined systematic uncertainty, as described by the following two equations.

$$\sigma_{\hat{\theta}}^{stat} = \sqrt{\sum_{i=1}^{n} \frac{w_i}{|w_i|} \left(w_i \sigma_{\hat{\theta}_i}^{stat} \right)^2} \qquad \sigma_{\hat{\theta}}^{sys} = \sqrt{\sigma_{\hat{\theta}}^2 - \left(\sigma_{\hat{\theta}}^{stat} \right)^2}$$
(6.9)

The combined cross-sections and nuclear modification factors, calculated from equations 6.8 and 6.9, are presented in the following chapter 7.

6.5 FINITE BIN WIDTH CORRECTION

While the grouping of reconstructed ω mesons in $p_{\rm T}$ intervals is necessary to accomplish the signal extraction described in section 5.3, the resulting cross-sections have to be interpreted cautiously, specifically, the falling underlying distribution means that the values of the respective intervals do not represent the cross-section at the center of each bin, as described in [LW95]. Therefore, the data points of the measured cross-sections have to be shifted in the horizontal direction, following the approach suggested in [LW95]. This is done by first parameterizing the cross-sections by a Tsallis function $f(p_{\rm T})$ [Tsa88], which is given by:

$$E\frac{d^3\sigma}{dp^3}(p_{\rm T}) = f(p_{\rm T}) = \frac{C}{2\pi} \frac{(n-1)(n-2)}{nT \left[nT + m_{\omega}(n-2)\right]} \left(1 + \frac{\sqrt{m_{\omega}^2 + p_{\rm T}^2} - m_{\omega}}{nT}\right)^{-n}, \quad (6.10)$$

where C, n and T are free parameters in the parametrization. The correct p_T value p_T^{shifted} within the interval from p_T^a to p_T^b is determined by requiring the the following equation:

$$f(p_{\rm T}^{\rm shifted}) = \frac{1}{p_{\rm T}^b - p_{\rm T}^a} \int_{p_{\rm T}^a}^{p_{\rm T}^b} f(p_{\rm T}) \mathrm{d}p_{\rm T}.$$
 (6.11)

This requirement is fulfilled for the value of p_T at which the function value $f(p_T)$ equals the expectation value of $f(p_T)$ in the given p_T interval. As the shape of the underlying distribution is unknown before the shift, and the shift might change the shape of the measured distribution, equation 6.11 is iteratively solved for $p_T^{\rm shifted}$, with new p_T positions and a new parametrization for each iteration. The positions converge after around three iterations with a shift on the order of one percent, as shown in figure 6.10. The relative horizontal shifts of the p_T values given in figure 6.10 are applied to their respective cross-section to correct the preliminary p_T normalization described in section 6.1. Besides correcting the vertical value due to this preliminary normalization, the p_T values of the final cross sections shown in the following chapter are also set to the calculated $p_T^{\rm shifted}$ values.

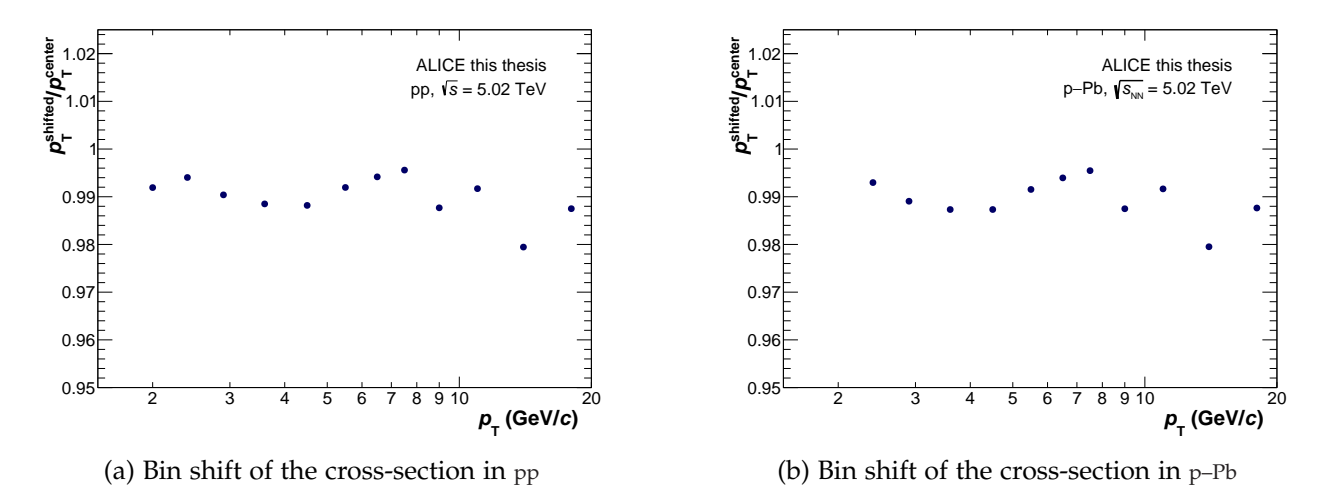


Figure 6.10: Relative p_T shift of the cross sections.

7.1 INVARIANT CROSS-SECTIONS

The $p_{\rm T}$ differential Lorentz-invariant production cross-section of ω mesons is extracted in pp and p-Pb collisions at $\sqrt{s_{\rm NN}}=5.02$ TeV within the transverse momentum range of 1.8 GeV/ $c \le p_{\rm T} < 20$ GeV/c and 2.2 GeV/ $c \le p_{\rm T} < 20$ GeV/c, respectively. The pp and p-Pb measurements covered the rapidity interval of |y| < 0.85 and -1.315 < y < 0.385, respectively. Figure 7.1 shows the extracted cross-sections, four predictions by MC event

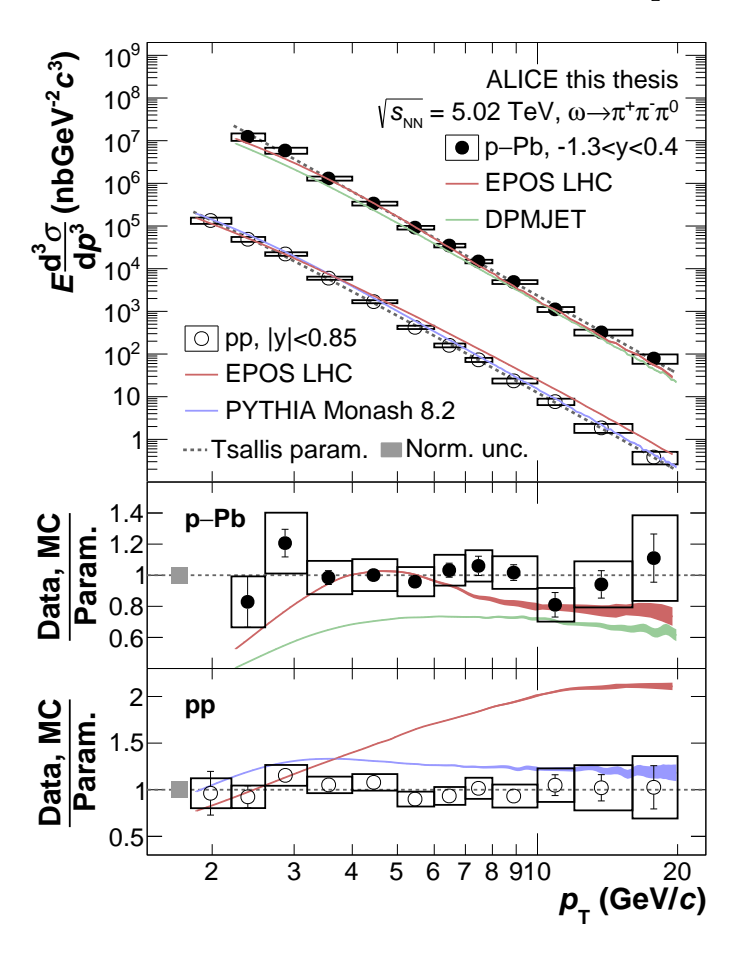


Figure 7.1: Lorentz-invariant cross-section of the ω meson production in pp (open markers) and p-Pb (closed markers). Vertical error bars represent statistical uncertainties, while systematic uncertainties are shown as boxes. Also shown are Tsallis parametrizations (equation 6.10) of the two cross-sections and two predictions of the ω meson production per collision system. The lower panels contain the ratios of the datapoints and MC predictions to the parametrization of the datapoints in the respective collision system.

| | С | T (MeV) | n | χ^2 /ndf | ndf |
|------|--|--|--|---------------------------|-----|
| рр | $57^{\pm 37 \text{ (stat)}}_{\pm 42 \text{ (tot)}} mb$ | $135_{\pm 37 \text{ (tot)}}^{\pm 21 \text{ (stat)}}$ | $6.2^{\pm 0.2 \text{ (stat)}}_{\pm 0.4 \text{ (tot)}}$ | 1.20 (stat) 0.49 (tot) | 9 |
| p–Pb | $25_{\pm 18 \text{ (tot)}}^{\pm 13 \text{ (stat)}} b$ | $113^{\pm 15}_{\pm 23}$ (stat) | $6.2_{\pm 0.8 \text{ (tot)}}^{\pm 0.4 \text{ (stat)}}$ | 0.87 (stat) 0.48 (tot) | 8 |

Table 7.1: Parameters and χ^2/ndf of the Tsallis function describing the measured ω meson production cross-sections in pp and p-Pb, as shown in figure 7.1

generators, and a Tsallis parametrization of the data for each collision system. The ratios of the datapoints to the respective Tsallis parametrization in the lower panels are compatible with unity over the full $p_{\rm T}$ range, demonstrating that the parametrizations well describe the data both in pp and p-Pb collisions. The parameters of the Tsallis functions describing the cross-sections are listed in table 7.1, where the uncertainties of the values are extracted by performing the fit individually on the cross-section with only the statistical uncertainty and then with the statistical and systematic uncertainty added in quadrature.

The lower panels in figure 7.1 depict to what degree the different MC event generators introduced in section 1.4 describe the production of ω mesons. While the DPMJET MC, shown as a green band in figure 7.1 roughly describes the p_T shape of the cross-section in p-Pb, it underestimates the production of ω mesons by approximately 30%. On the other hand, the production of ω mesons in p-Pb collisions is well described by EPOS LHC, depicted in red. The use of the same event generator for the simulation of pp collisions is, however, not able to describe the data, with discrepancies of up to 100% seen in the lower panel between EPOS LHC and the datapoints. While the other pp MC event generator, PYTHIA 8.2 with the Monash 2013 tune, describes the shape of the production cross-section in pp collisions, it overestimates the production of ω mesons by around 30%.

While the production cross-section of the ω mesons has been measured for the first time in p–Pb collisions at the LHC in this analysis, the extracted cross-section in pp collisions joins two previous measurements performed at $\sqrt{s}=7$ TeV [Ach+2o] and $\sqrt{s}=13$ TeV [Lü23]. This increasing number of production measurements cannot only serve as input for direct photon analyses at the respective energies but also facilitates the development of theoretical models and can contribute to future tunes of MC event generators. The measured cross-sections furthermore allow for studies of the energy dependence of particle production. Figure 7.2 shows a compilation of these three measured ω production cross-sections in pp collisions at the LHC, as well as predictions by the PYTHIA 8.2 generator using the Monash tune. A similar deviation between these PYTHIA predictions and the respective measured cross-section is observed in all three ω meson analyses [Ach+2o; Lü23], hinting at a possible energy-independent overestimation of the ω meson production in the Monash 2013 tune of PYTHIA 8.2.

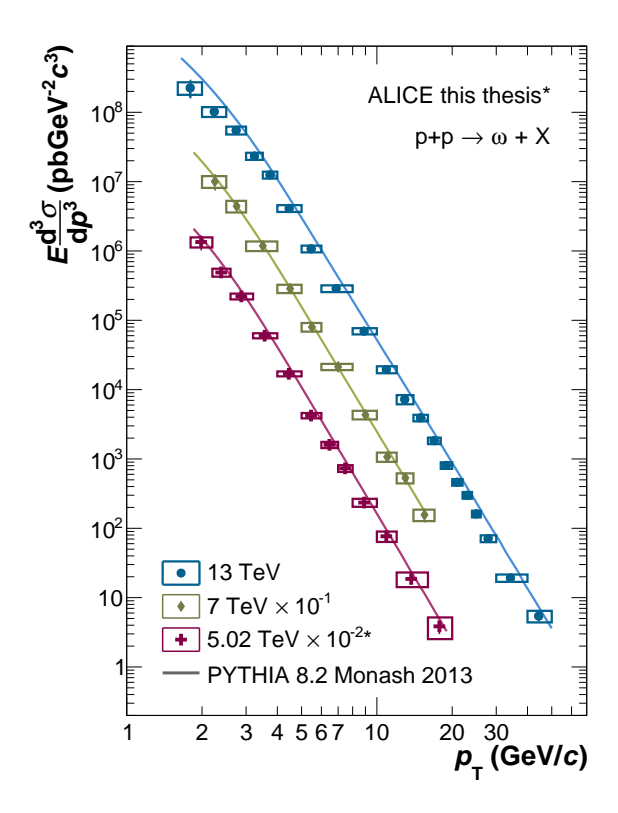


Figure 7.2: Compilation of ω meson production cross-sections in pp collisions measured at LHC energies [Ach+20; Lü23], scaled for better visibility, and the respective predictions by the PYTHIA 8.2 event generator with the Monash 2013 tune [Bie+22]

7.2
$$\omega/\pi^0$$
 ratios

The ratio of produced ω and π^0 mesons is calculated from the measured ω meson cross-sections, shown in figure 7.1, and the corresponding π^0 spectra in pp [Sas19] and p-Pb collisions [Ach+18b]. Figure 7.3 shows the measured ω/π^0 ratio in the two collision systems, both of which do not display a significant p_T dependence. Each of the two production ratios is parameterized with a constant for $p_T > 3.2$ GeV/c; this minimal p_T is chosen to ensure compatibility with previous analyses [Ada+11b]. These parametrizations are shown in figure 7.3 as purple dashed lines, yielding the following high p_T ω/π^0 production ratio constants:

$$C_{\rm pp}^{\omega/\pi^0} = 0.54 \pm 0.01 \, (stat) \pm 0.03 \, (sys)$$
 (7.1)
 $C_{\rm pPb}^{\omega/\pi^0} = 0.54 \pm 0.01 \, (stat) \pm 0.04 \, (sys)$

Within the given uncertainties and $p_{\rm T}$ reach, the ω/π^0 production ratios are in very good agreement with one another. This agreement of the production ratio in pp and p-Pb suggests the production ratio to be independent of CNM effects within the given uncertainties.

The extracted high- $p_{\rm T}$ constants can furthermore be used as input for the transverse mass scaling prediction of the ω/π^0 ratio. This empirical model describes the production

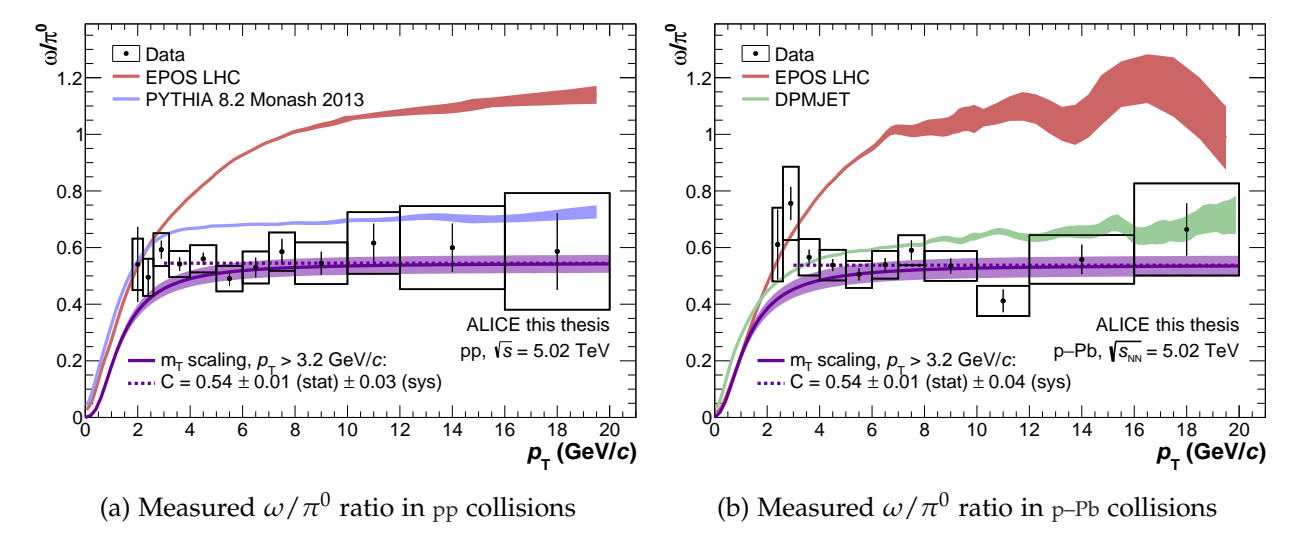
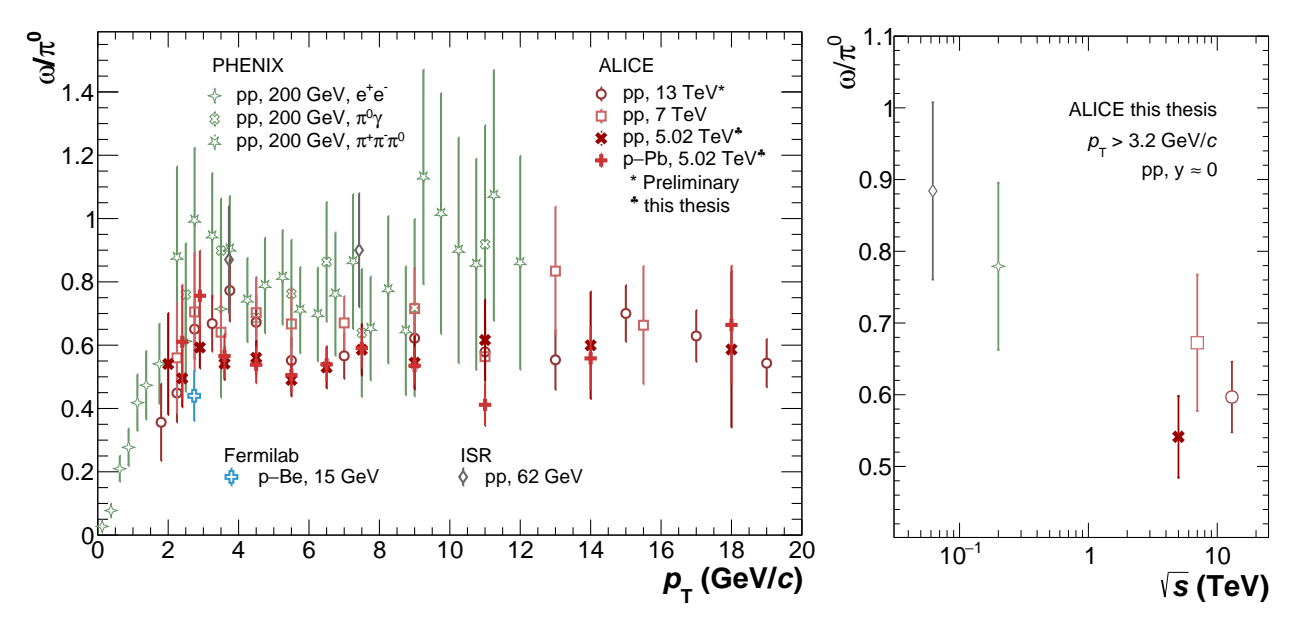


Figure 7.3: Production ratio ω/π^0 in pp and p-Pb collisions calculated using the ω meson production measurements from this analysis and π^0 references provided by [Sas19; Ach+18b]. Furthermore, two predictions by MC event generators are shown per collision system, as well as a m_T scaling curve, which converges towards a fitted high- p_T constant.

ratio by assuming that the production of all mesons follows the same fundamental underlying function of the particles transverse mass $(m_{\rm T} = \sqrt{p_{\rm T}^2 + m_{\rm inv}^2})$, scaled by a constant parameter C [Alt+17]. From the high- p_T constant given in 7.1, this assumption is used to derive the p_T dependence of the particle ratio, as shown with purple bands in figure 7.3. A slight tension between the ω/π^0 ratio prediction assuming m_T scaling and the data is observed at low transverse momenta $p_T \approx 3 \text{ GeV/}c$, where m_T scaling suggests a decrease of the ω/π^0 ratio, while the measured ω/π^0 ratios are p_T independent within their uncertainties. A slight discrepancy is expected, as m_T scaling was found to be broken for LHC energies due to the feed-down of decays into the π^0 [Alt+17]. However, the increased number of neutral pions from the feed-down of higher mass particles would decrease the ω/π^0 ratio compared to the m_T scaling prediction. The excess of the ω/π^0 ratio at low p_T compared to the m_T was also observed at $\sqrt{s}=13$ TeV, but its underlying cause remains unexplained. This discrepancy shows the need for ω meson production measurements like the one presented in this thesis, as studies of direct photons or dileptons commonly resort back to this $m_{\rm T}$ scaling prediction, due to the lack of experimental data [Ada+16; Ach+19].

In addition to the measured production ratios, figure 7.3 also includes predictions of the ω/π^0 ratio by three MC event generators. The predictions of the ω/π^0 ratio by EPOS LHC, shown in red, are very similar between pp and p-Pb, suggesting the system size does not have a strong impact on the relative hadronization fractions into ω mesons and neutral pions. However, the production ratio is overestimated by around 100% in both collision systems, possibly hinting at a lack of experimental data for tuning the implemented collective hadronization. The production ratios predicted by PYTHIA 8.2



- (a) Transverse momentum dependent ω/π^0 measurements at different center-of-mass energies and collision systems
- (b) High $p_{\rm T}$ constant of the ω/π^0 ratio at different energies in pp

Figure 7.4: Compilation of measurements of the ω/π^0 ratio at various center-of-mass energies covering 15 GeV $<\sqrt{s_{\rm NN}}<$ 13 TeV at Fermilab [Don+8o], the ISR [Bre+89], PHENIX [Ada+11a] and ALICE [Ach+20; Lü23] including the two measurements at $\sqrt{s_{\rm NN}}=$ 5.02 TeV presented in this thesis. Vertical error bars represent total uncertainties.

Monash 2013 in pp and DPMJET in p–Pb are somewhat similar. This can be traced back to the fact that the hadronization implemented in DPMJET is based on the Lund string model, also used by the PYTHIA event generator. Both MC generators using the Lund string model overestimate the ω/π^0 ratio by around 10-20 %. It is, however, not evident whether the different approaches to hadronization cause this more accurate description of the ω/π^0 ratio or whether this difference should be attributed to the different tunes and experimental input used.

Figure 7.4a shows the two measurements of the ω/π^0 ratio from this analysis in the context of the previous measurements introduced in section 1.5, covering different collision systems and almost three orders of magnitude in center-of-mass energies, from $\sqrt{s_{\rm NN}}=15$ GeV at Fermilab [Don+8o] up to $\sqrt{s}=13$ TeV at the LHC [Lü23]. For the datapoints provided by the Fermilab and ISR measurements, only a minimum $p_{\rm T}$ was set in the analysis. The $p_{\rm T}$ positions of these datapoints in a given $p_{\rm T}$ interval were therefore set to the expectation value of the Tsallis parametrization of the pp cross-section extracted in this analysis.

The ω/π^0 ratios measured at different energies are compatible within the given total uncertainties represented by vertical bars. A slight tension is, however, visible when considering the entire $p_{\rm T}$ range of the measurement at $\sqrt{s_{\rm NN}}=200$ GeV, depicted with green markers, and at $\sqrt{s_{\rm NN}}=5.02$ TeV, depicted with red markers. To better visualize

this possible difference of the ω/π^0 ratio for different center-of-mass energies, the ratios shown in figure 7.4a are parameterized with a constant for $p_T > 3.2$ GeV/c, with the resulting values of these high- p_T fits of the ω/π^0 ratio compiled in figure 7.4b. To isolate possible effects of the center-of-mass energy, only ω/π^0 ratios measured in p_T collisions are considered for this comparison.

As the correlation between the uncertainties of the PHENIX and Fermilab measurements are not precisely known, the systematic uncertainties of all measurements are assumed to be fully correlated within each measurement for calculating the uncertainty on the high- $p_{\rm T}$ constant. This assumption gives an upper-limit estimation of the total uncertainties shown in figure 7.4b.

The resulting high- $p_{\rm T}$ ω/π^0 constant as a function of the center-of-mass energy presented in figure 7.4b displays a slight tendency of a lower ω/π^0 ratio with rising center-of-mass energy. While this energy dependence is not significant within the relatively large uncertainties, center-of-mass energy dependent feed-down into the π^0 could offer a possible explanation for such a trend. Specifically, the production of heavier particles at larger center-of-mass energies could lead to increasing feed-down of these particles into the π^0 and thereby decrease the measured ω/π^0 ratio. Further measurements at low and high collision energies are needed to verify or disprove this trend.

7.3 NUCLEAR MODIFICATION FACTOR

The nuclear modification factor of the ω meson production at $\sqrt{s_{\text{NN}}} = 5.02$ TeV, extracted in the transverse momentum range of 2.2 GeV/ $c \le p_{\text{T}} < 20$ GeV/c, is shown with purple markers in figure 7.5. This represents the first measurement of the nuclear modification factor of the ω meson at LHC energies. Within the statistical and systematic uncertainties, represented by vertical bars and boxes, respectively, the nuclear modification factor is found to be compatible with unity over the measured p_{T} range. Consequently, no CNM effects on the ω meson production are observed within the given uncertainties.

Figure 7.5 furthermore displays the nuclear modification factor for neutral pions, measured at the same center-of-mass energy of $\sqrt{s_{\text{NN}}}=5.02$ TeV [Ach+18b]. The visible agreement between the nuclear modification factors for the light π^0 and the six times heavier ω meson [Pdg22] implies that within the given uncertainties of the two measurements, no mass dependency of the nuclear modification factor is observed.

Finally, figure 7.5 also includes the nuclear modification factor $R_{\rm dAu}$ for the production of ω mesons at $\sqrt{s_{\rm NN}}=200$ GeV [Ada+11b]. This nuclear modification factor $R_{\rm dAu}$ is compatible with the $R_{\rm pPb}$ extracted in the analysis presented in this thesis within the respective statistical and systematic uncertainties.

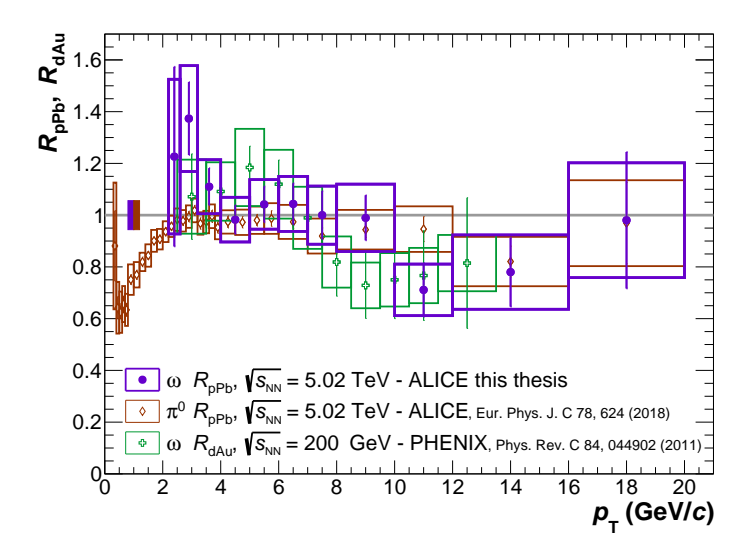


Figure 7.5: Nuclear modification factor $R_{\rm pPb}$ of the ω meson at $\sqrt{s_{\rm NN}}=5.02$ TeV extracted in this analysis shown with purple markers, as well as a nuclear modification factor of neutral pions at the same center-of-mass energy [Ach+18b] and a measurement for ω mesons at $\sqrt{s_{\rm NN}}=200$ GeV [Ada+11b]. Vertical error bars and boxes represent statistical and systematic uncertainties, while the two solid boxes show the normalization uncertainty of the ALICE measurements.

SUMMARY AND OUTLOOK

This thesis covers the measurement of the ω meson production in pp and p-Pb collisions at $\sqrt{s_{\rm NN}} = 5.02$ TeV. Between 2015 and 2017, the ALICE experiment at the LHC recorded 944 million pp collisions and 568 million p-Pb collisions using its large array of subdetectors. The ω mesons produced within these collisions are reconstructed via their three-pion decay ($\omega \to \pi^+\pi^-\pi^0$), of which the charged pions are tracked using ALICE's tracking detectors ITS and TPC. The charged pions are then identified out of all charged particles based on their specific energy loss dE/dx in the TPC and their time of flight from the collision vertex to the TOF detector. The neutral pion itself decays further into two photons, which are measured using the EMCal, or, in case the photons convert into an e^+e^- pair in the inner detector layers, they are reconstructed with the Photon Conversion Method (PCM) via tracks of these dilepton pairs in the TPC. The ensuing reconstruction of ω meson candidates from these pions displayed a smeared-out ω signal on top of a sizeable combinatoric background. While extensive background studies show no viable way of reducing the background, the smeared signal is traced back to the energy resolution of the photon reconstruction, which is then mitigated using a newly developed MC-driven resolution correction. After extracting the ω meson signal for the three different π^0 reconstruction methods, many corrections are applied, most notably the acceptance and efficiency correction, leading to three partially independent measurements of the crosssection in pp and p-Pb, and the nuclear modification factor. The individual measurements (PCM, PCM-EMCal and EMCal) are found to be compatible with each other within their uncertainties. They are then combined using the BLUE method, resulting in a reduction of the combined statistical and systematic uncertainties and effectively consolidating their complementary transverse momentum coverage.

The combined production cross-section of ω mesons is extracted in pp and p-Pb collisions within 1.8 GeV/ $c \le p_{\rm T} < 20$ GeV/c and 2.2 GeV/ $c \le p_{\rm T} < 20$ GeV/c, respectively. These cross-sections are now available as input not only for direct photon analyses but also to test and develop theoretical models describing the hadronization of vector mesons, as described in [SI17]. They can furthermore be used to tune MC generators to better describe the production of ω mesons, which seems especially relevant considering the varying success of predictions of the ω meson production by different MC event generators. From the extracted production cross-sections of the ω meson production in pp and p-Pb collisions together with the corresponding π^0 spectra at the same energy [Sas19; Ach+18b], the ω/π^0 ratio is calculated for the two collision systems. The production ratios in pp and p-Pb collisions are found to be constant within the measured $p_{\rm T}$ interval

and agree with each other within their uncertainties. When comparing the measured ω/π^0 ratios to an empirical model assuming transverse mass scaling, an excess of the measured ratio compared to the m_T -scaling prediction is observed. As this is contrary to the expected effect at LHC energies due to feed-down into the π^0 [Alt+17], further research is worth considering to gain a better understanding of this unexpected behavior. When comparing ω/π^0 ratios covering three orders of magnitude in center-of-mass energy, a slight hint of a possible energy dependence of the ω/π^0 ratio is observed. Specifically, analyses performed at LHC energies, including the one presented in this thesis, measure the ω/π^0 ratio to be smaller than measurements at lower center-of-mass energy at PHENIX. As this trend is not significant with the limited available statistics, additional investigations into the existence and the underlying reason for such an energy dependence are believed to be beneficial. Concluding this analysis, the first measured nuclear modification factor of ω mesons is extracted within the transverse momentum range of 2.2 GeV/ $c \le p_T < 20$ GeV/c. As the modification factor is compatible with unity, no nuclear modification is observed within the uncertainties.

A preliminary version of the results presented in this thesis was approved by the ALICE collaboration, and a publication on these results by the ALICE Collaboration is currently under preparation. Building upon this analysis, three aspects have been identified, which could further expand the significance of ω meson measurements in pp and p-Pb collisions in order to address the above-mentioned open issues:

- 1. Besides the analyzed MB events, the p-Pb data set furthermore includes a significant number of events triggered by the EMCal on the condition of highly energetic clusters in the EMCal. A dedicated analysis of these events could not only increase the precision of the existing measurement but also expand the measurement to higher transverse momenta.
- 2. Following a similar objective, the π^0 reconstruction methods could be expanded by the merged EMCal method, in which neutral pions with high transverse momenta are identified from elliptical clusters containing both decay photons [Ach+22].
- 3. Another promising approach to enhance the significance of the measurement lies in the discrimination between ω mesons and background using machine learning, as currently under development for the η' reconstruction also through the three pion channel [Gli].

With the ω meson production measured at the LHC in pp and p-Pb collisions, the measurements could also be expanded to Pb-Pb collisions, thereby providing insights into the properties of the QGP through the production and properties of ω mesons in Pb-Pb collisions. Regardless of their exact approach, all upcoming analyses on ω meson production stand to profit from the extensive detector upgrades to the ALICE detector that were installed between 2018 and 2020, allowing for data taking at much higher interaction rates, and thereby drastically reducing statistical uncertainties of future measurements.



APPENDIX

A.1 RUNLISTS

pp: LHC15n (Data) and LHC17e2+LHC18j3 (MCs)

PCM, PCM-EMCal & EMCal: 244340, 244343, 244351, 244355, 244359, 244364, 244377, 244421, 244453, 244456, 244480, 244481, 244482, 244483, 244484, 244531, 244540, 244542, 244617, 244618, 244619, 244626, 244627, 244628

pp: LHC17pq (Data) and LHC17l3b+LHC18j2 (MCs)

- PCM: 282008, 282016, 282021, 282025, 282030, 282031, 282050, 282051, 282078, 282098, 282099, 282118, 282119, 282120, 282122, 282123, 282125, 282126, 282127, 282146, 282147, 282189, 282206, 282224, 282227, 282229, 282230, 282247, 282302, 282303, 282304, 282305, 282306, 282307, 282309, 282312, 282313, 282314, 282340, 282341, 282342, 282343, 282367, 282366, 282365
- (PCM-)EMCal: 282343, 282342, 282341, 282340, 282314, 282313, 282312, 282307, 282306, 282305, 282304, 282303, 282302, 282247, 282230, 282229, 282227, 282224, 282206, 282189, 282147, 282146, 282126, 282123, 282122, 282119, 282118, 282099, 282098, 282078, 282051, 282031, , 282025, 282367, 282366, 282365

p-Pb: LHC16qt (Data) and LHC18f3 (MC)

- PCM: 265525, 265521, 265501, 265500, 265499, 265435, 265427, 265426, 265425, 265424, 265422, 265421, 265420, 265419, 265388, 265387, 265385, 265384, 265383, 265381, 265378, 265377, 265344, 265343, 265342, 265339, 265338, 265336, 265335, 265334, 265332, 265309, 267166, 267165, 267164, 267163
- (PCM-)EMCal: 265525, 265521, 265501, 265500, 265499, 265427, 265426, 265425, 265424, 265421, 265420, 265419, 265388, 265387, 265384, 265383, 265378, 265344, 265343, 265342, 265339, 265338, 265336, 265335, 265334, 265332, 265309, 267166, 267165, 267164, 267163

A.2 UNEXPECTED TOF SIGNALS

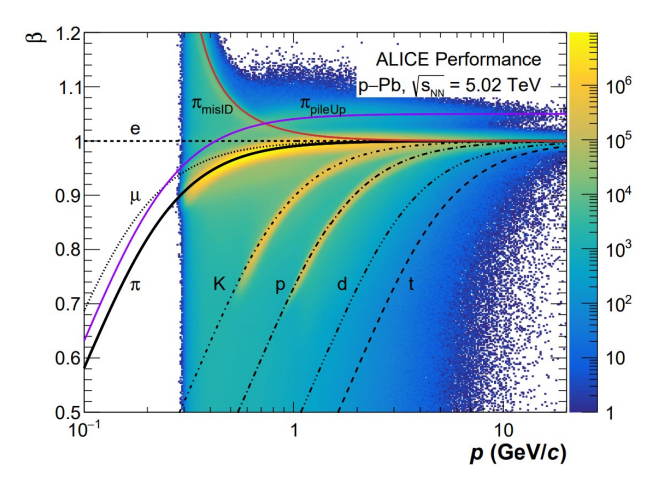
As described in section 4.1, the distribution of velocities β measured by the TOF detector shows two accumulations above one, as depicted in figure A.1a. Excluding the possibility of the improbable accidental discovery of tachyons, these shapes were traced back to detector effects. While these explanations are not proven to cause these accumulations, they have been derived from plausible assumptions and can quantitatively describe the observed shapes, as described in the following.

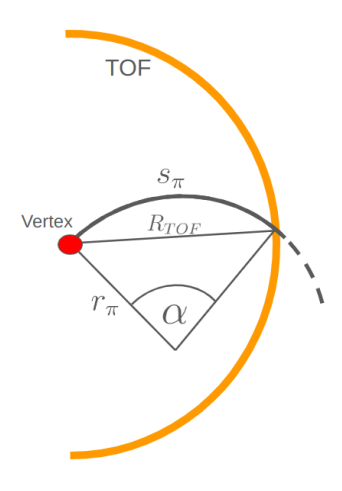
PILE-UP For the recorded data, bunches pass through ALICE every 200 ns. During these bunch crossings, particles are produced both in head-on collisions but also in interactions with the rest gas in the beam pipe. When a collision takes place, but a particle from a previous bunch crossing is already moving through ALICE, this particle could reach the TOF cylinder up to 200 ns earlier, than any particle produced in the actual collision. In other words, the start time for the TOF signal of this first particle would be triggered one bunch crossing later and therefore $\Delta t = 200$ ns too late. This would falsely increase the velocity of the particles by approximately

$$\Delta \beta_{\text{pile-up}} = \frac{R_{\text{TOF}}}{\Delta t} = \frac{3.7 \,\text{m}}{200 \,\text{ns}} = 0.06.$$
 (A.1)

This shift would therefore correspond to a duplicate of every particle species band in the TOF velocity plot, shifted upwards by 0.06. To test, whether this effect is observed and can even explain one of the unexpected accumulations in the velocity distribution, a shifted version of the pion band is included in purple in figure A.1a. One observes good qualitative agreement between the calculated and observed shapes, especially at high $p_{\rm T}$. While this shifted band would also be expected for the other species, they are not visible in figure A.1a, as these other particles are produced in much smaller quantities and therefore their *pile-up band* does not stand out from the background.

mismatched pion tracks — To assign the velocity to a given track, it has to be matched with the correct corresponding TOF cluster. To qualitatively describe one effect of a track-TOF cluster mismatch, one can consider the concrete mismatch depicted in figure A.1b. This example corresponds to a slow pion ($p \sim 0.5 GeV/c$) and another fast ($p \sim 5 GeV/c$) particle produced in the same collision, reaching the TOF in close proximity. As the radius of a particles trajectory in a magnetic field is proportional to its velocity, the slow pion would fly in a considerably curved trajectory s_{π} according to the radius r_{π} , while the trajectory of the fast particle can be approximated by a line of length R_{TOF} . Based on this example shown in figure A.1b, one can quantify the falsely measured velocity when the track of the slow pion is matched to the TOF cluster of the fast particle. In equation A.2, one first calculates the radius r_{π} of the slow-moving pion based on the equality of the centrifugal and the Lorentz force acting on the pion. Equation A.3 then





- (a) Measured velocities of charged particles by TOF including two lines explaining the two observed unexpected accumulations above unity
- (b) Example of a TOF-track mismatch

Figure A.1: Measured velocities by the TOF detector (left) and a schematic drawing of an explanation for one of the observed false signals (right)

describes the angle α , that the pion travels through on its circular trajectory s_{π} . Finally, equation A.4 utilizes the first two in order to quantify the velocity of the track of the slow pion, which was mismatched to the other particles TOF cluster.

$$F_{L} = qvB \stackrel{!}{=} \frac{v^{2}}{r_{\pi}}m = F_{C} \Rightarrow r_{\pi} = \frac{p}{qB}$$
(A.2)

$$\sin\left(\frac{\alpha}{2}\right) = \frac{R_{\text{TOF}}}{2r_{\pi}} \Rightarrow \alpha = 2\arcsin\left(\frac{R_{\text{TOF}}}{2r_{\pi}}\right)$$
 (A.3)

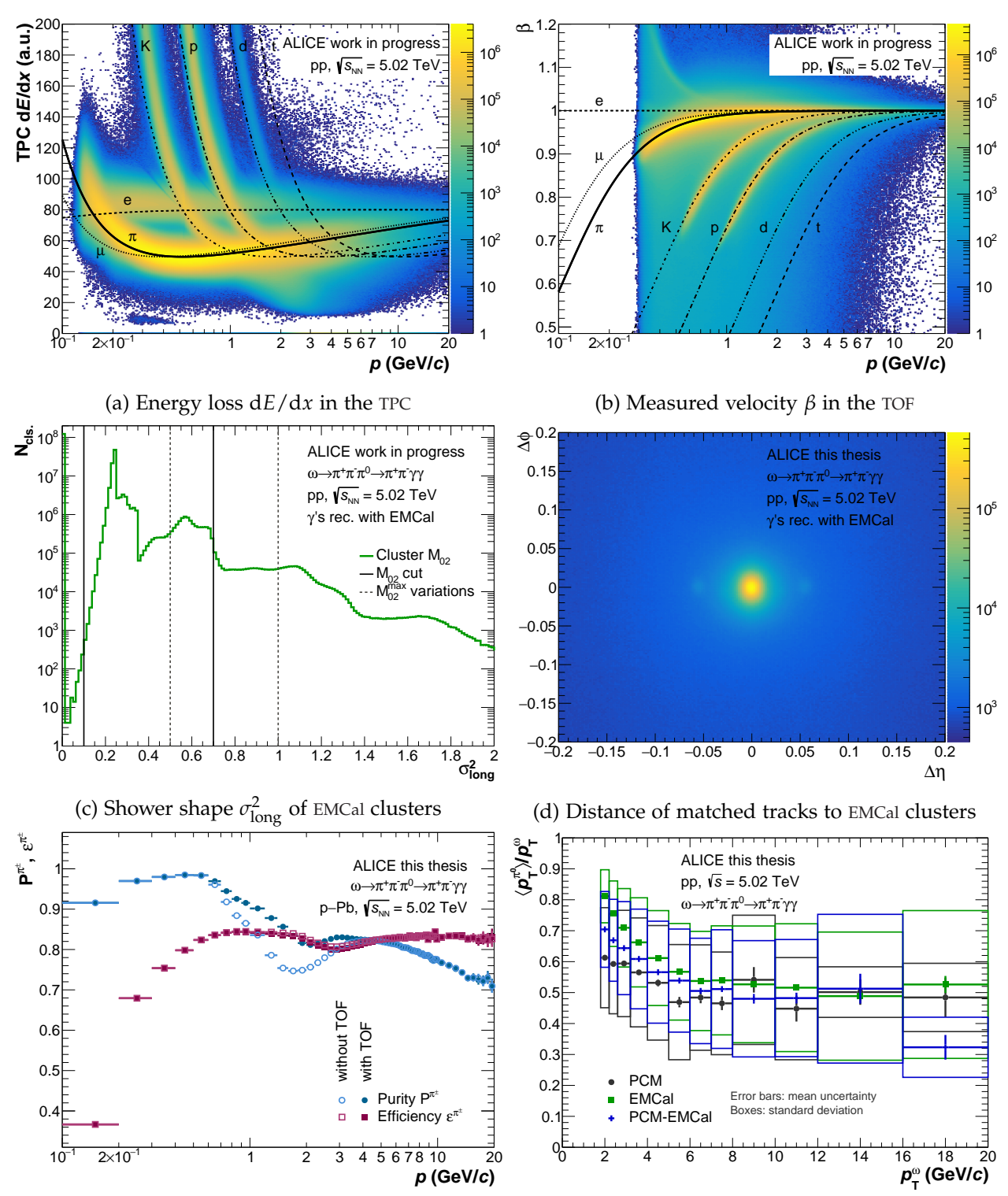
$$\beta = \frac{s_{\pi}}{tc} = \frac{\alpha r_{\pi}}{R_{\text{TOF}}} = \frac{2p}{qBR_{\text{TOF}}} \arcsin\left(\frac{qBR_{\text{TOF}}}{2p}\right) \tag{A.4}$$

Inserting the known variables $q_{\pi} = e$ (see 1.1), B = 0.5 T (see 2.2), and R = 3.7 m (see 2.2.4), the velocity of mismatched pion tracks can be approximated as:

$$\beta_{\text{mismatch}} = \frac{3.6 \ p}{\text{GeV}/c} \arcsin\left(\frac{1 \ \text{GeV}/c}{3.6 \ p}\right).$$
(A.5)

This velocity is expected to be falsely measured when a pions track is mismatched to the TOF cluster of any faster particle. The orange line in figure A.1a shows how this effect can qualitatively describe the second accumulation of particles with measured velocities larger than c. One can see how the velocity increase with decreasing momentum is well described by equation A.5, corresponding to increasing curvature of the particles trajectory. This considerable fraction of mismatched pions underlines the TOF rejection procedure described in section 4.1 compared to a selection-based approach, as these mismatched pions should still be included when reconstructing ω meson candidates.

A.3 PION AND PHOTON OBSERVABLES IN PP COLLISIONS



(e) Efficiency and purity of the reconstructed charged (f) ω $p_{\rm T}$ fraction of the π^0 , extracted from the properpions in p-Pb collisions ties in the pp MC simulation.

Figure A.2: Observables of the pion reconstruction in pp collisions.

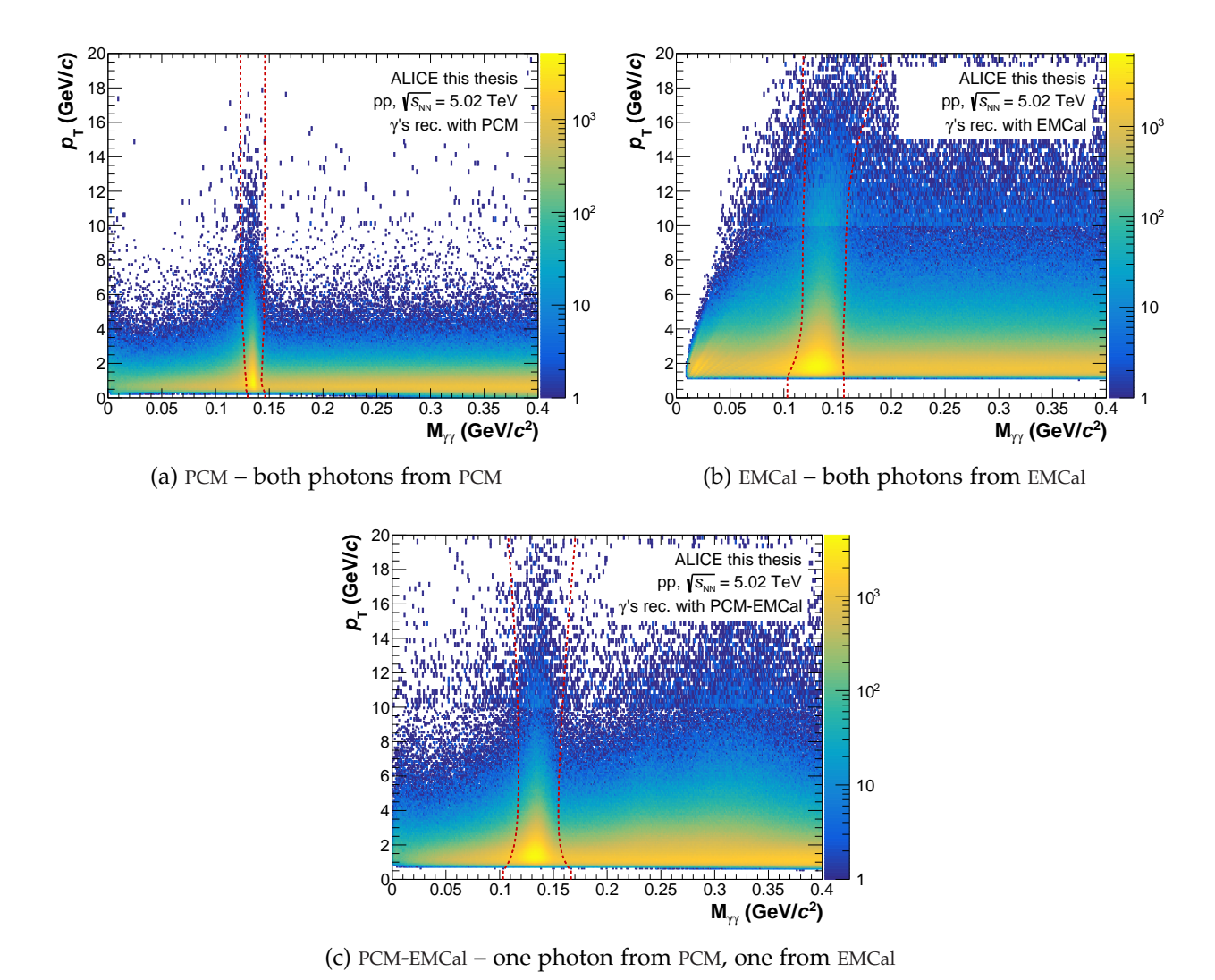


Figure A.3: Invariant mass distributions of all photon pairs in each event of the pp dataset as a function of transverse momentum for the three different reconstruction methods. For the subsequent ω meson reconstruction, only pion candidates in the $p_{\rm T}$ dependent mass range between the red, dotted lines were selected.

A.4 UNCERTAINTIES

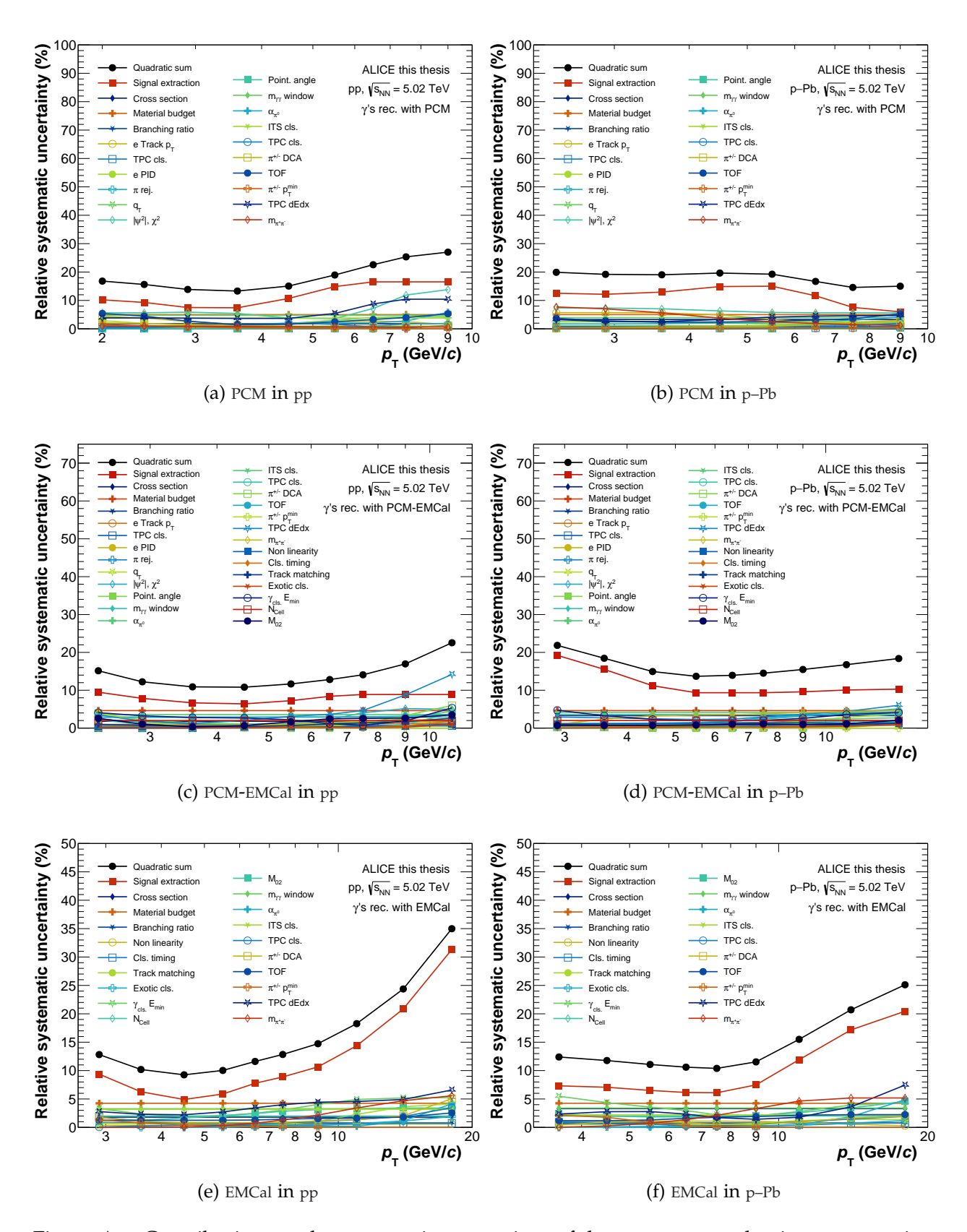


Figure A.4: Contributions to the systematic uncertainty of the ω meson production cross section for the three reconstruction methods and two collision systems

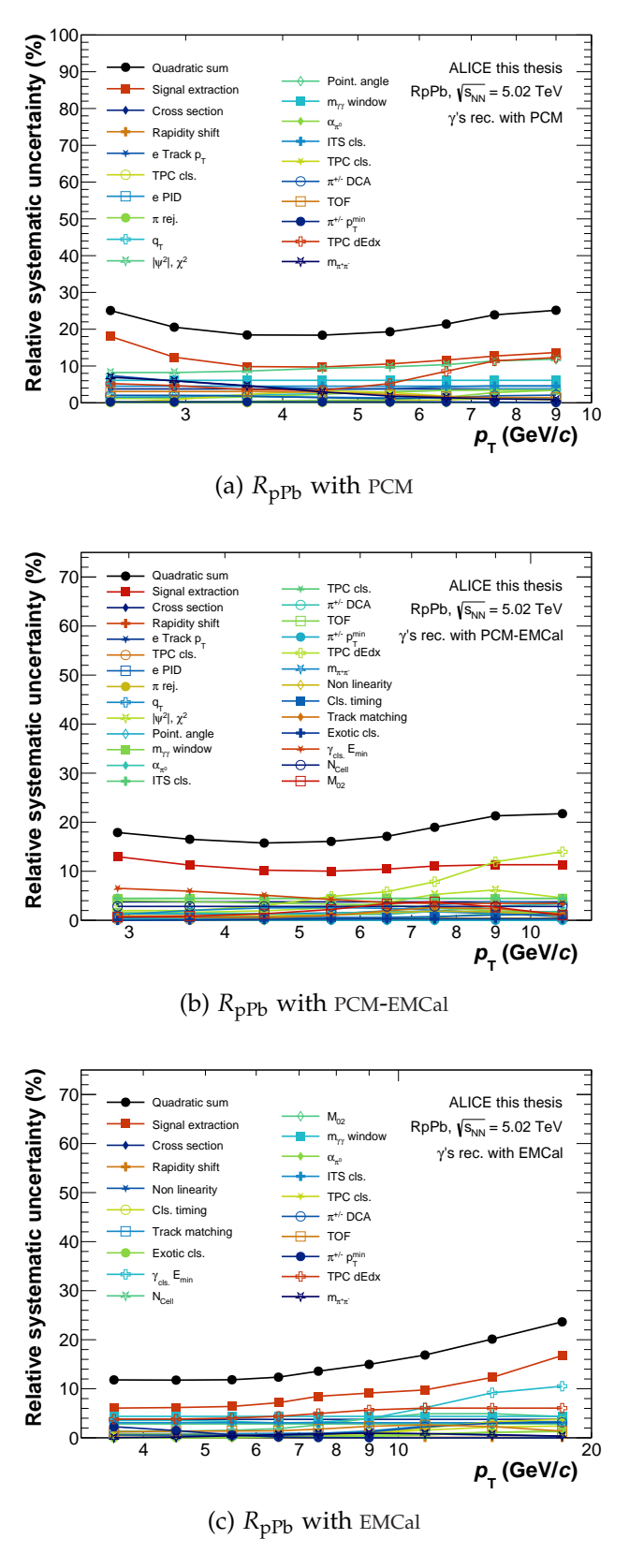
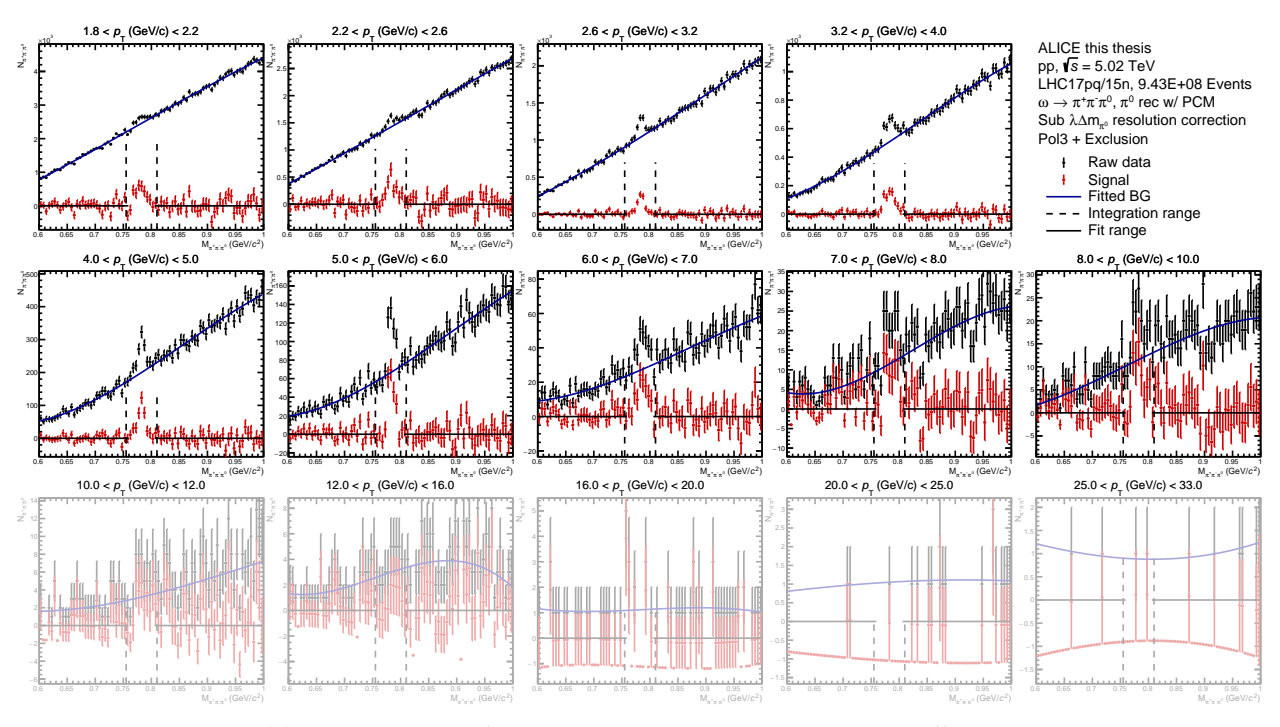


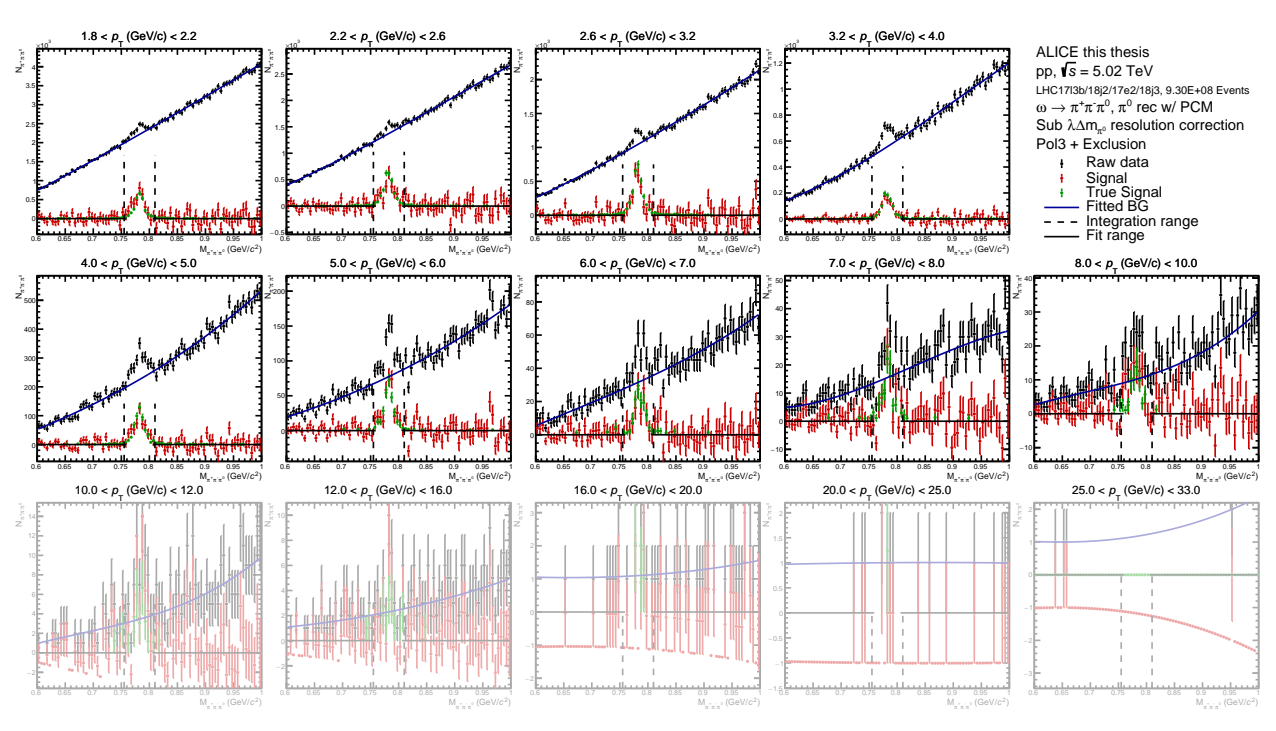
Figure A.5: Contributions to the systematic uncertainty of the nuclear modification factor R_{pPb} for the three reconstruction methods

A.5 INVARIANT-MASS DISTRIBUTIONS

PCM in pp



(a) Invariant-mass histograms in data using PCM in pp collisions



(b) Invariant-mass histograms in MC using PCM in pp collisions

Figure A.6: Invariant mass histograms in the different p_T intervals showing the distribution of ω -candidates, their background description, and the resulting signal. The background was fitted in the region of the solid horizontal line and the signal was then integrated within the dotted vertical lines

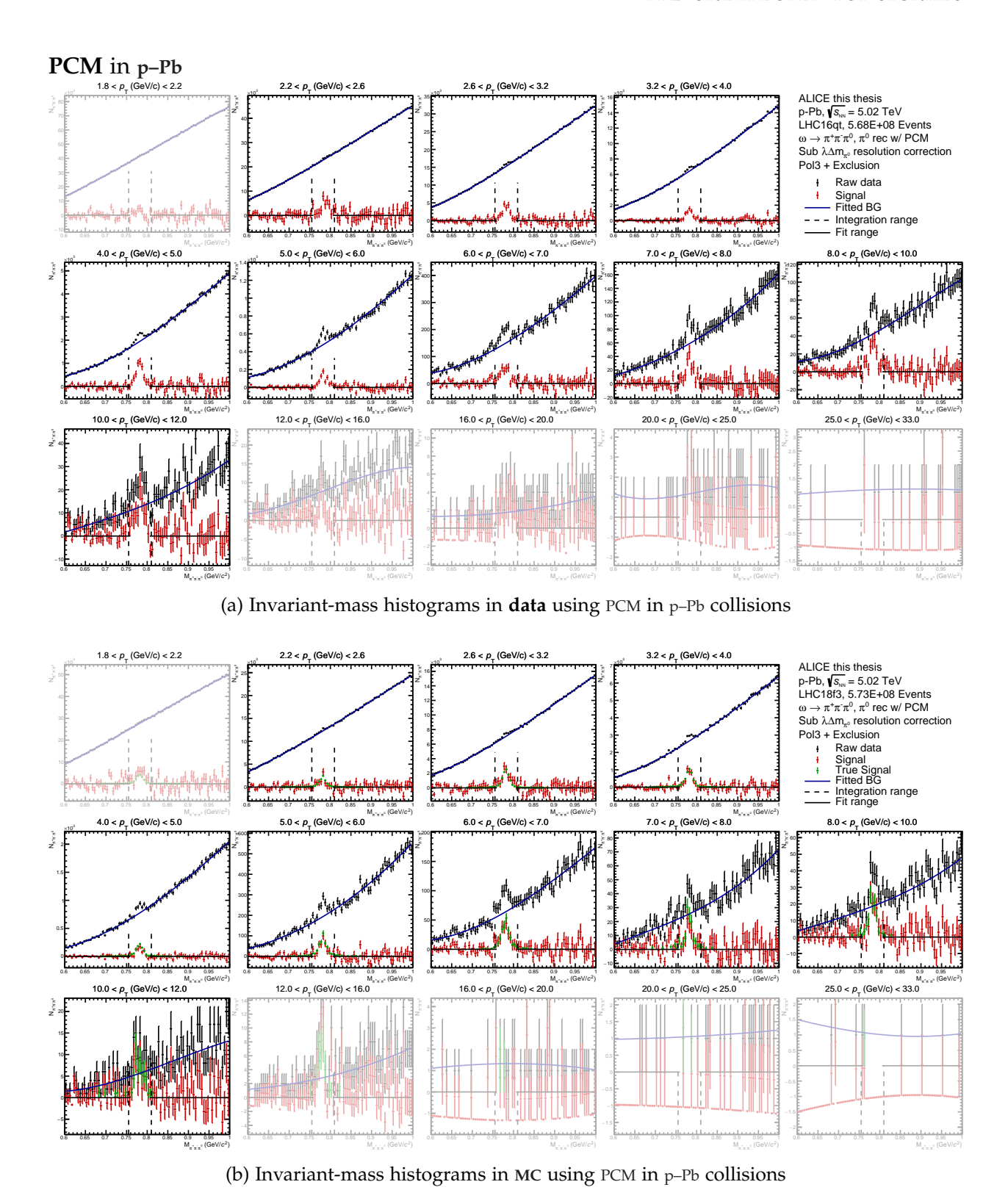
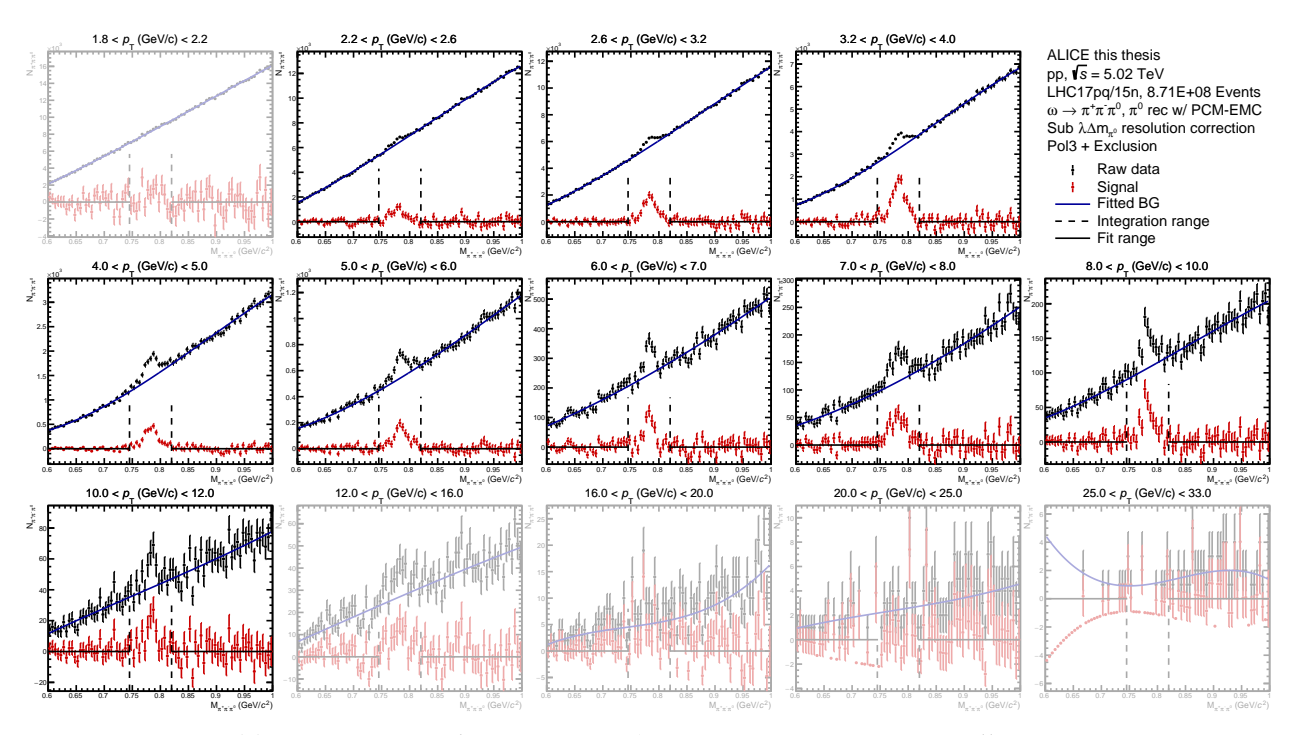
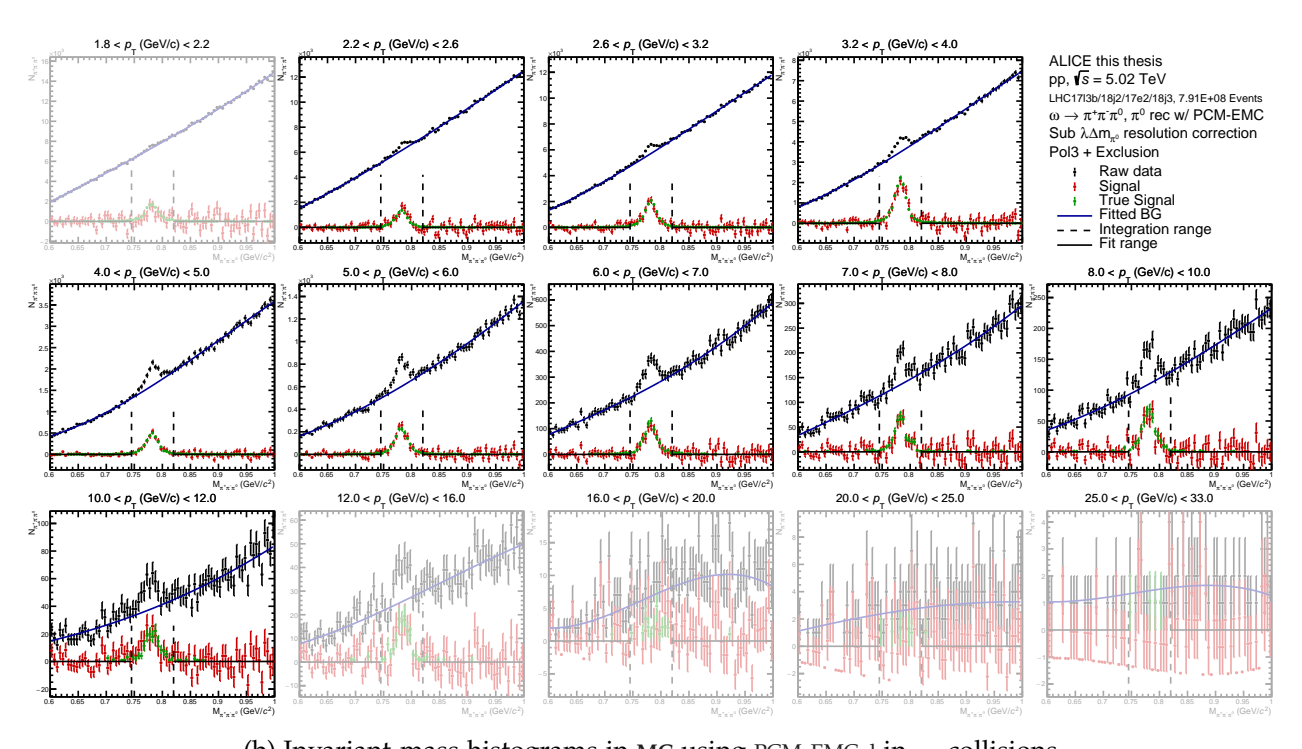


Figure A.7: Invariant mass histograms in the different p_T intervals showing the distribution of ω -candidates, their background description, and the resulting signal. The background was fitted in the region of the solid horizontal line and the signal was then integrated within the dotted vertical lines.

PCM-EMCal in pp



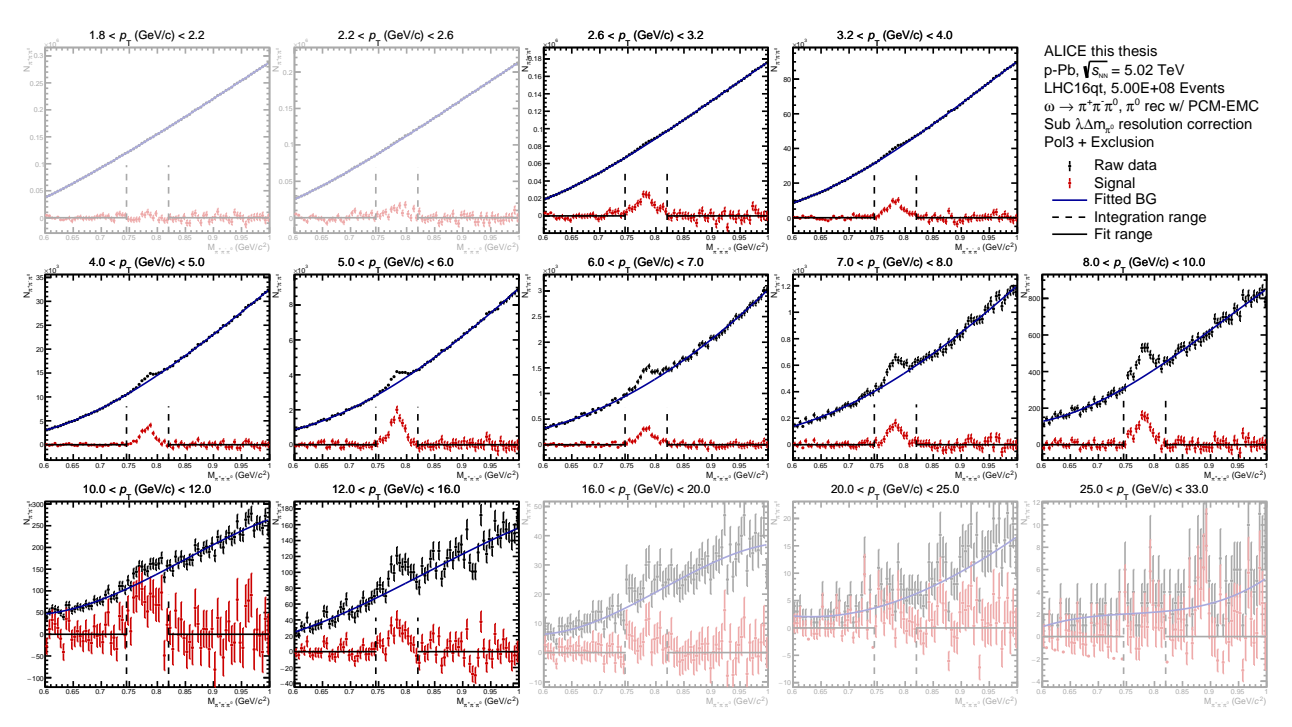
(a) Invariant-mass histograms in data using PCM-EMCal in pp collisions



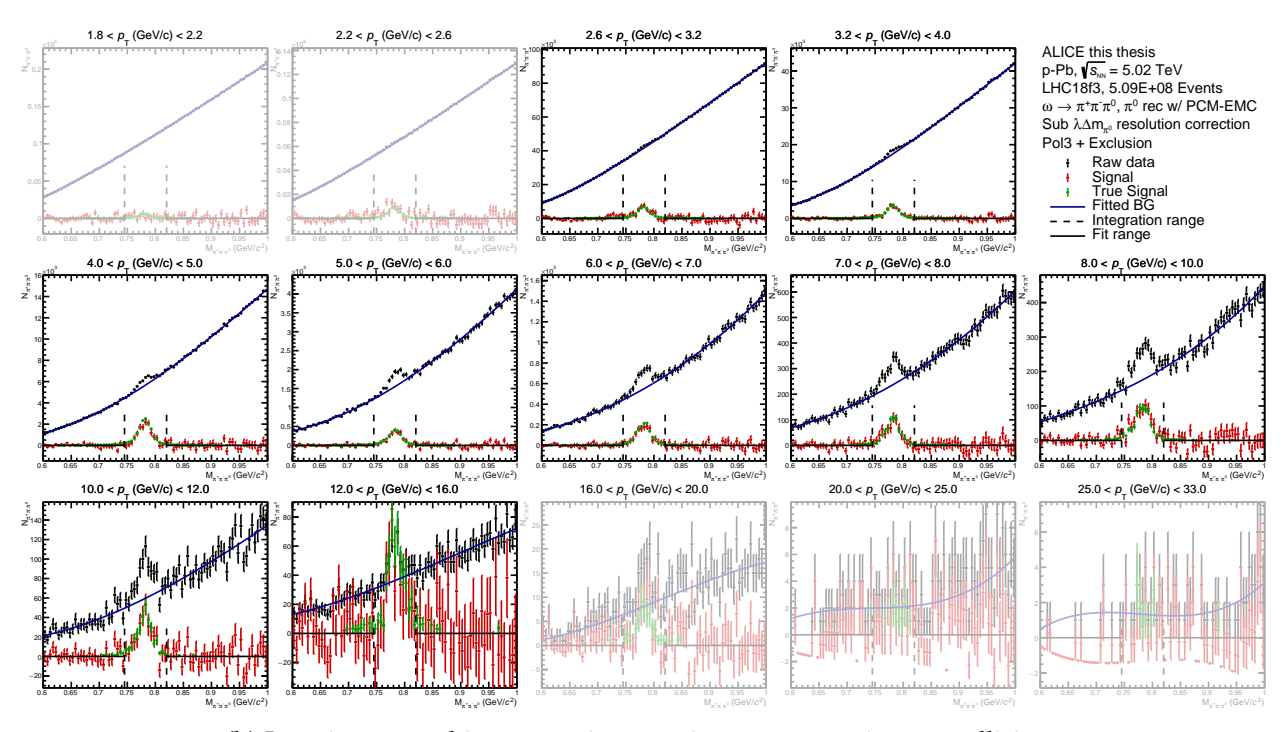
(b) Invariant-mass histograms in MC using PCM-EMCal in $\ensuremath{\text{pp}}$ collisions

Figure A.8: Invariant mass histograms in the different p_T intervals showing the distribution of ω -candidates, their background description, and the resulting signal. The background was fitted in the region of the solid horizontal line and the signal was then integrated within the dotted vertical lines.

PCM-EMCal in p-Pb



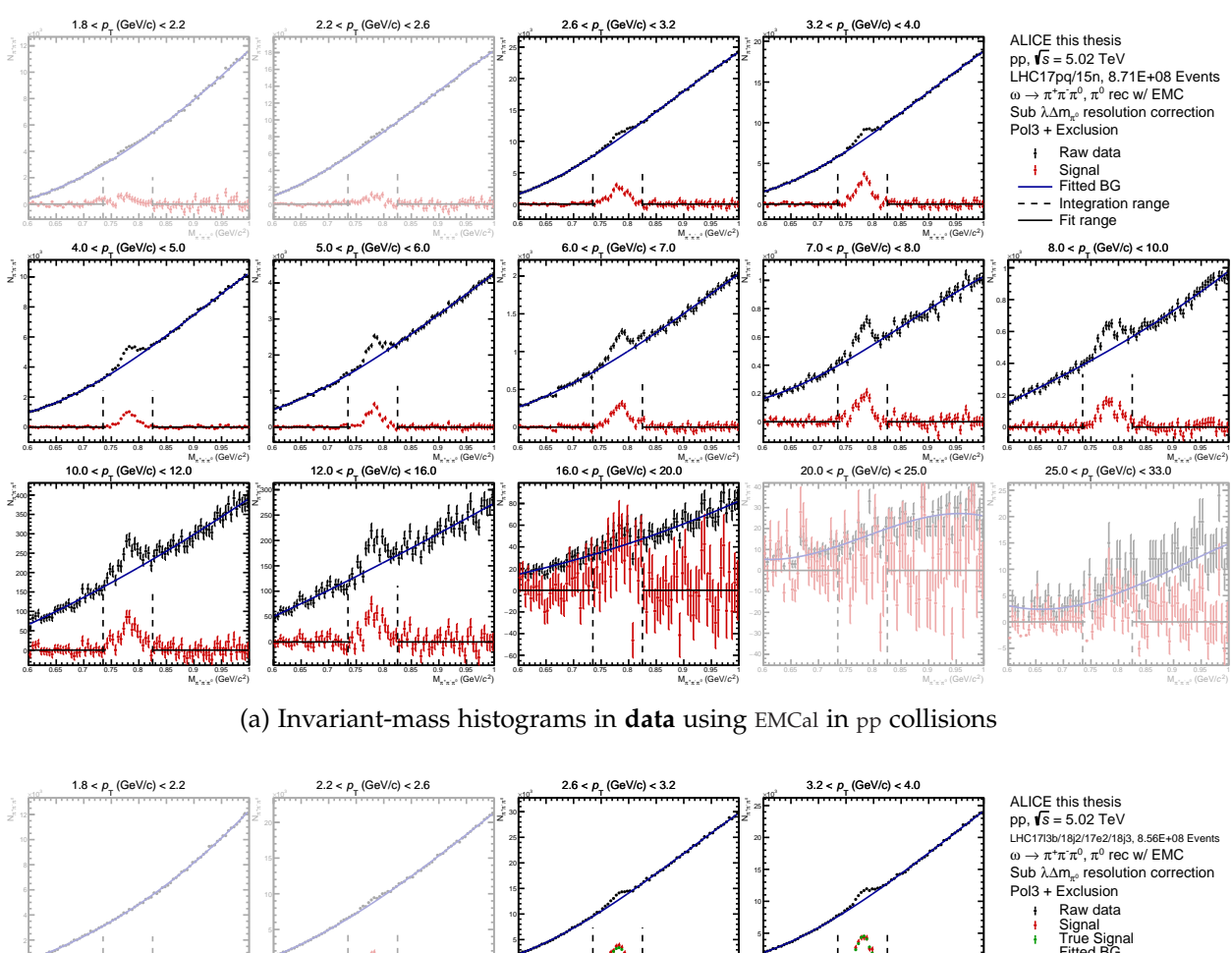




(b) Invariant-mass histograms in MC using PCM-EMCal in p-Pb collisions

Figure A.9: Invariant mass histograms in the different p_T intervals showing the distribution of ω -candidates, their background description, and the resulting signal. The background was fitted in the region of the solid horizontal line and the signal was then integrated within the dotted vertical lines.

EMCal in pp



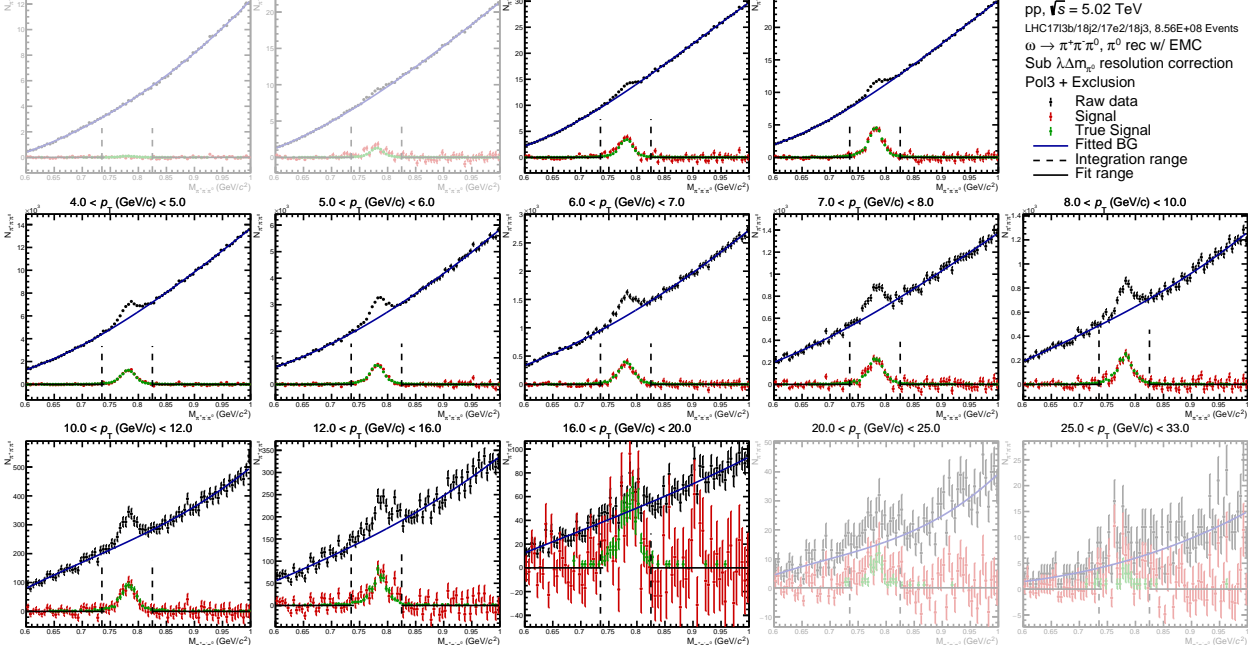
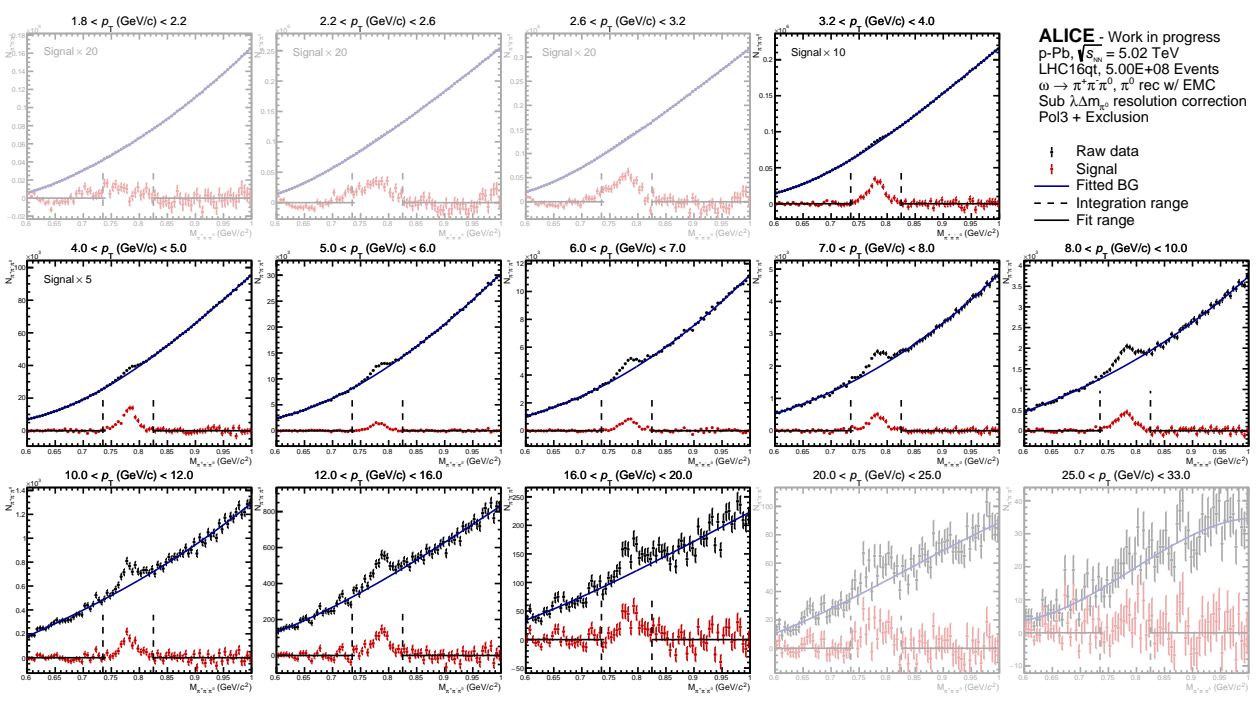


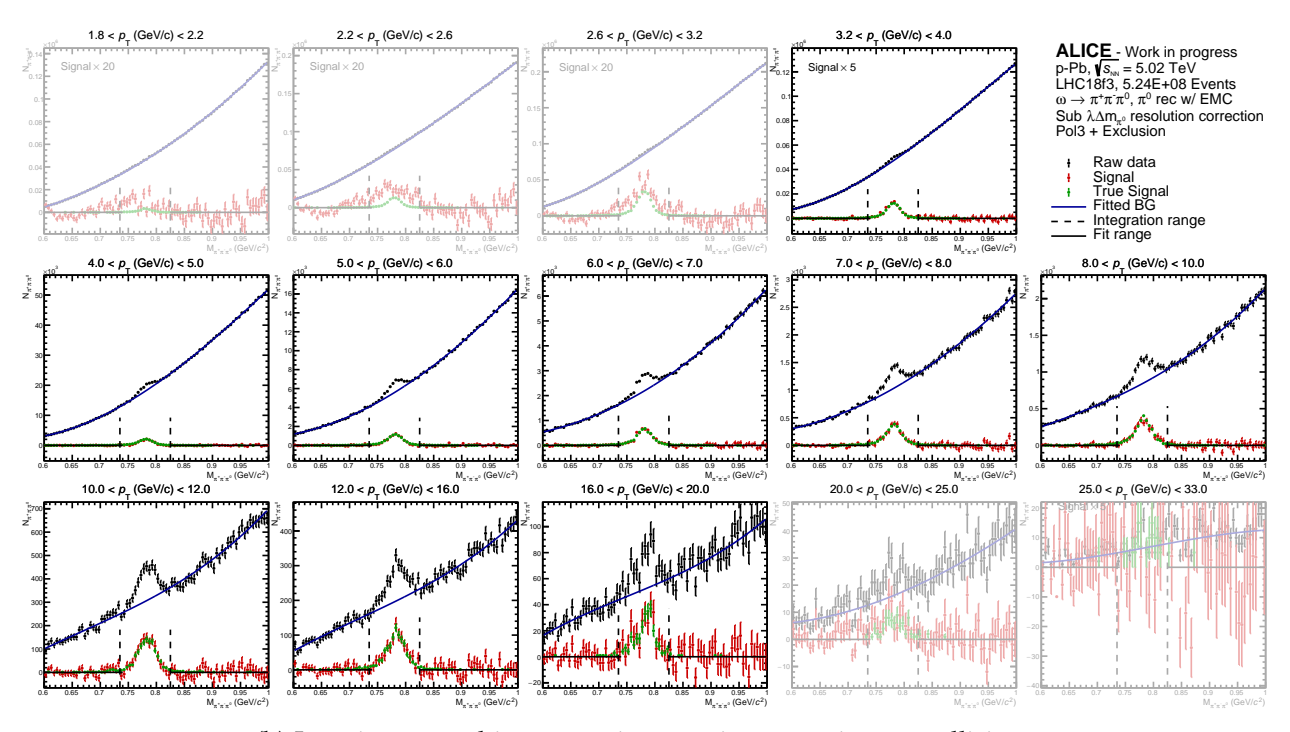
Figure A.10: Invariant mass histograms in the different $p_{\rm T}$ intervals showing the distribution of ω -candidates, their background description, and the resulting signal. The background was fitted in the region of the solid horizontal line and the signal was then integrated within the dotted vertical lines.

(b) Invariant-mass histograms in MC using EMCal in pp collisions

EMCal in p-Pb



(a) Invariant-mass histograms in **data** using EMCal in p-Pb collisions



(b) Invariant-mass histograms in MC using EMCal in p-Pb collisions

Figure A.11: Invariant mass histograms in the different $p_{\rm T}$ intervals showing the distribution of ω -candidates, their background description, and the resulting signal. The background was fitted in the region of the solid horizontal line and the signal was then integrated within the dotted vertical lines.

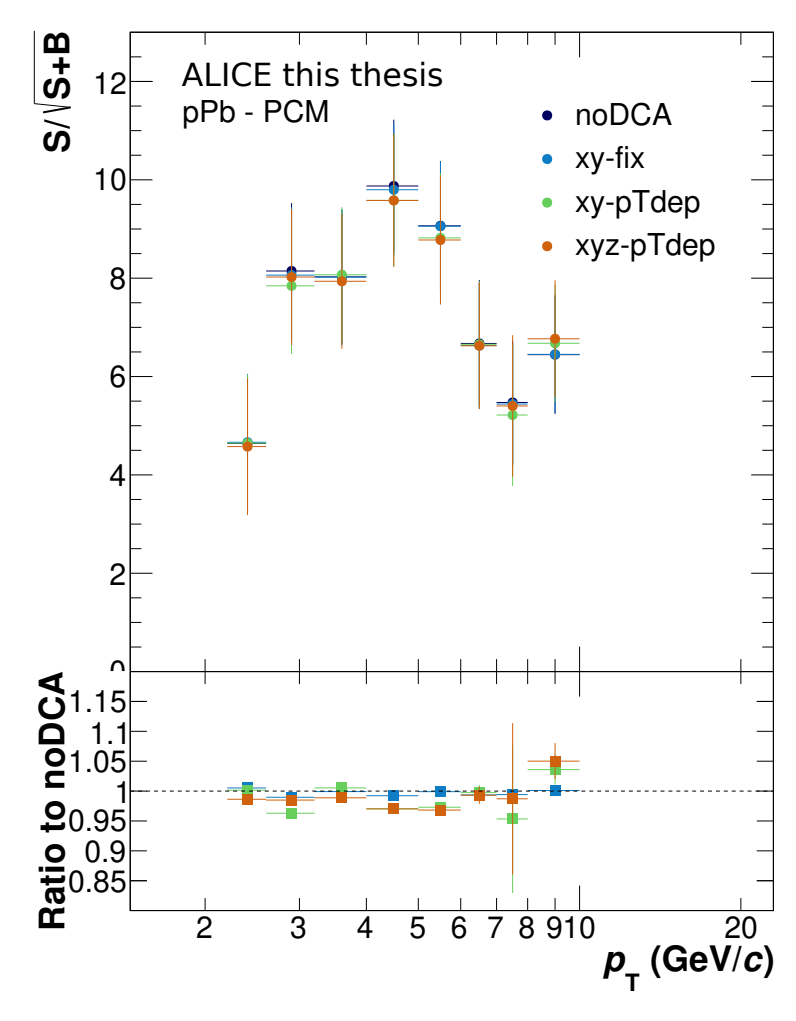


Figure A.12: Significance of the ω meson using different DCA cuts. noDCA in blue represents the utilized rather open DCA cut, while the variations describe restrictions of the DCA either in only the transverse plane (xy), or a three-dimensional cut (xyz). A reduction of the significance is observed for all DCA restrictions due to the loss in efficiency.

Background contributions using PCM

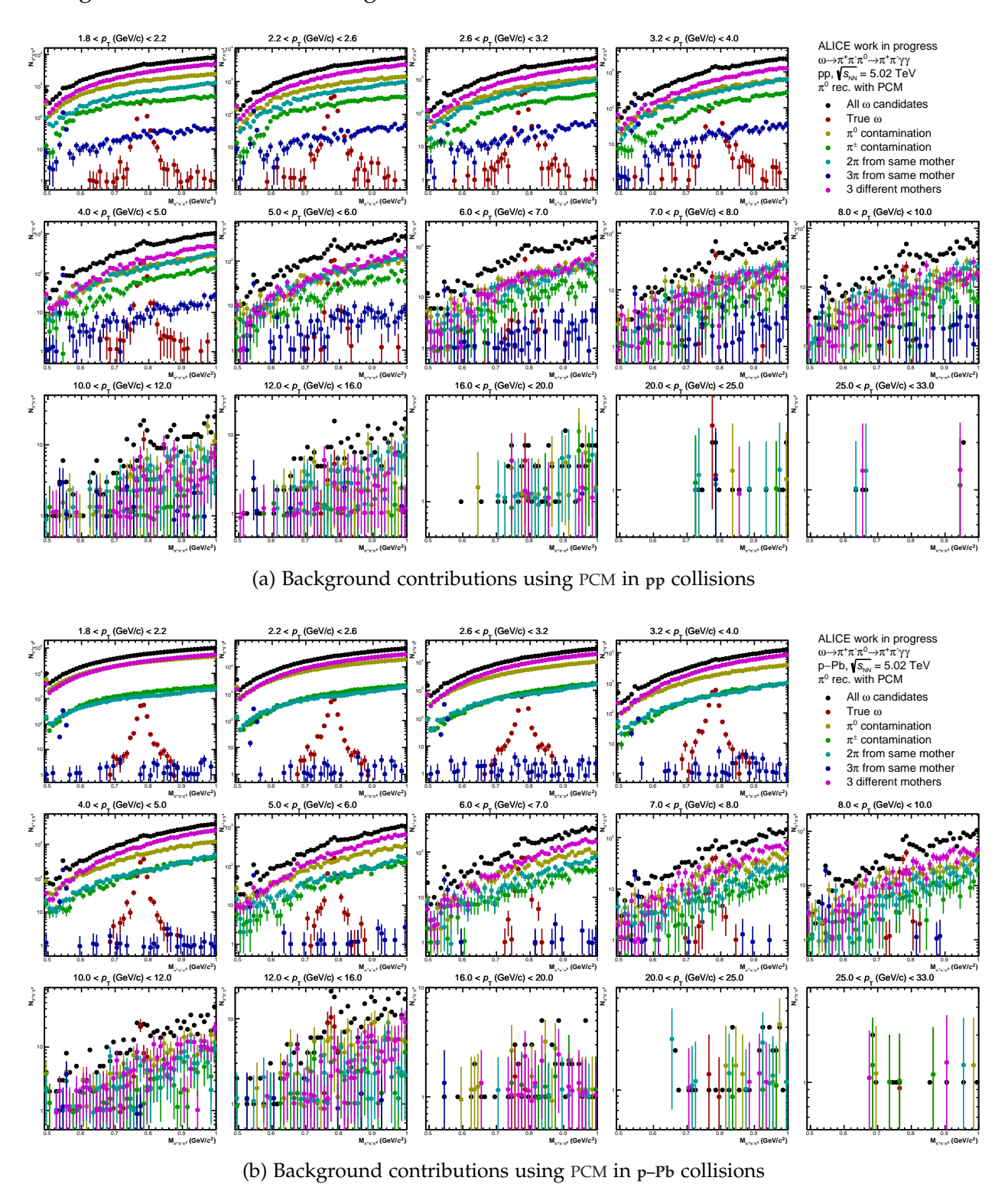


Figure A.13: Breakdown of the background contributions to the invariant mass distribution for the different p_T intervals using PCM

Background contributions using PCM-EMCal

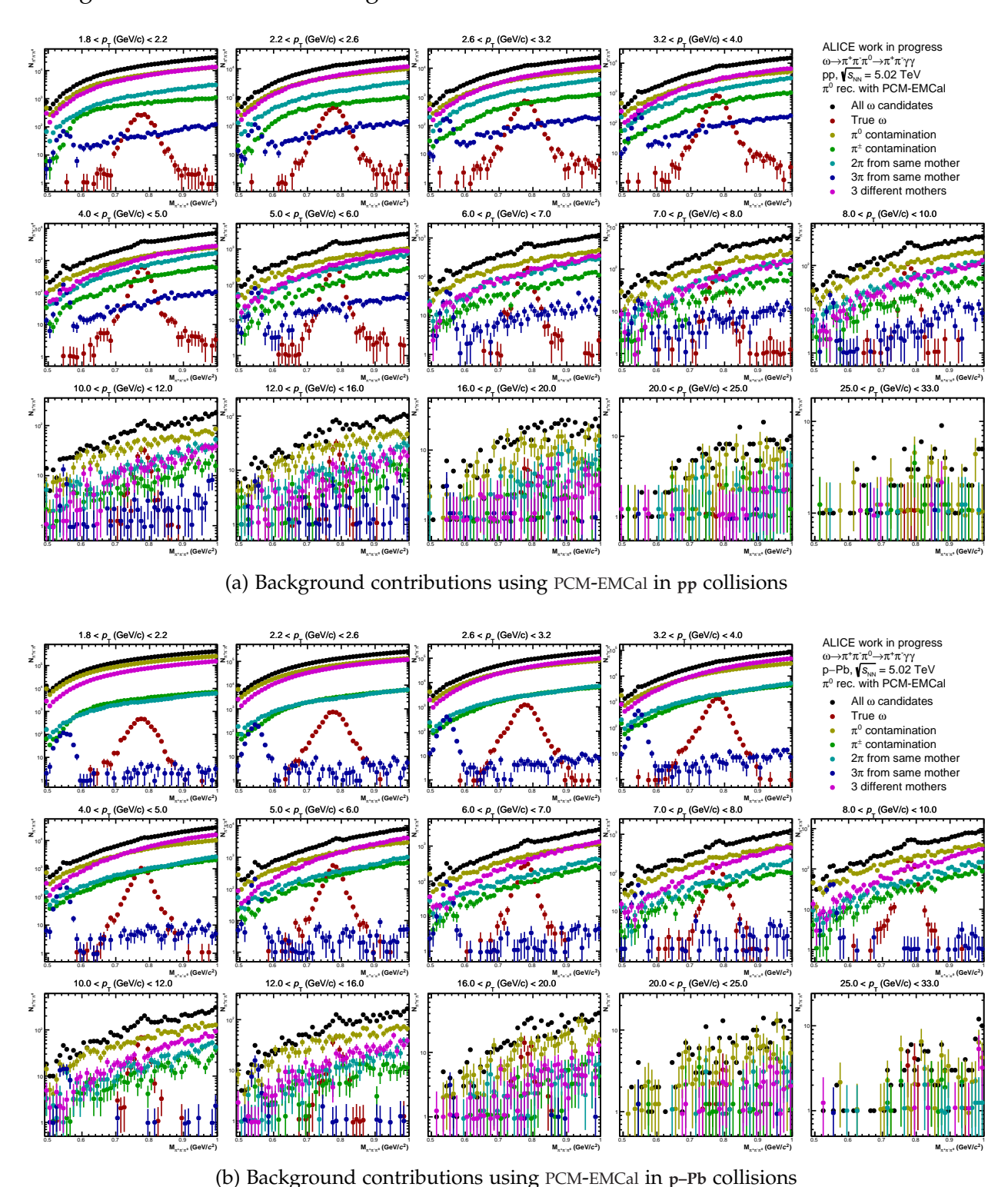


Figure A.14: Breakdown of the background contributions to the invariant mass distribution for the different p_T intervals using PCM-EMCal

Background contributions using EMCal

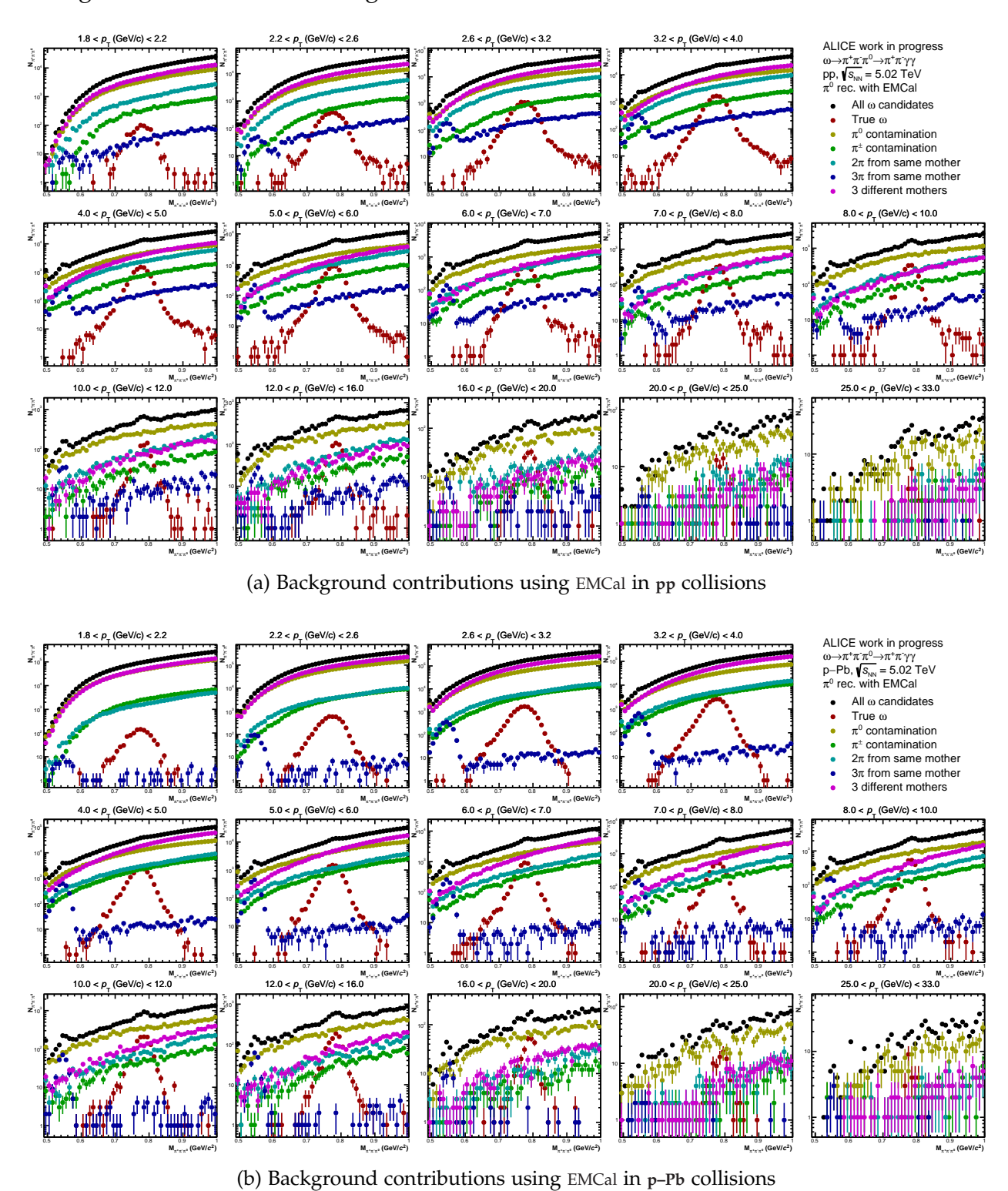


Figure A.15: Breakdown of the background contributions to the invariant mass distribution for the different p_T intervals using EMCal

Background contributions of two correlated pions using PCM

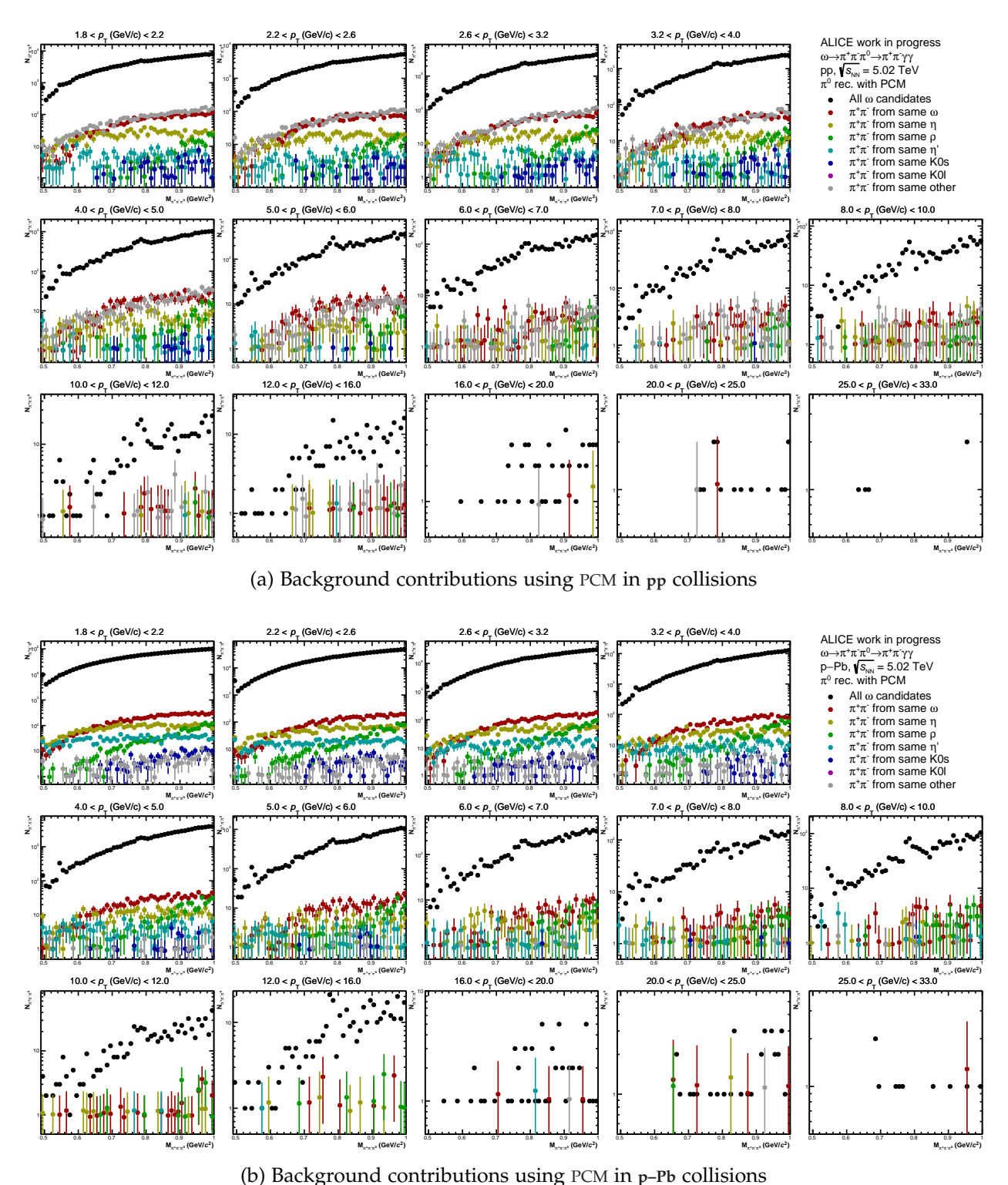
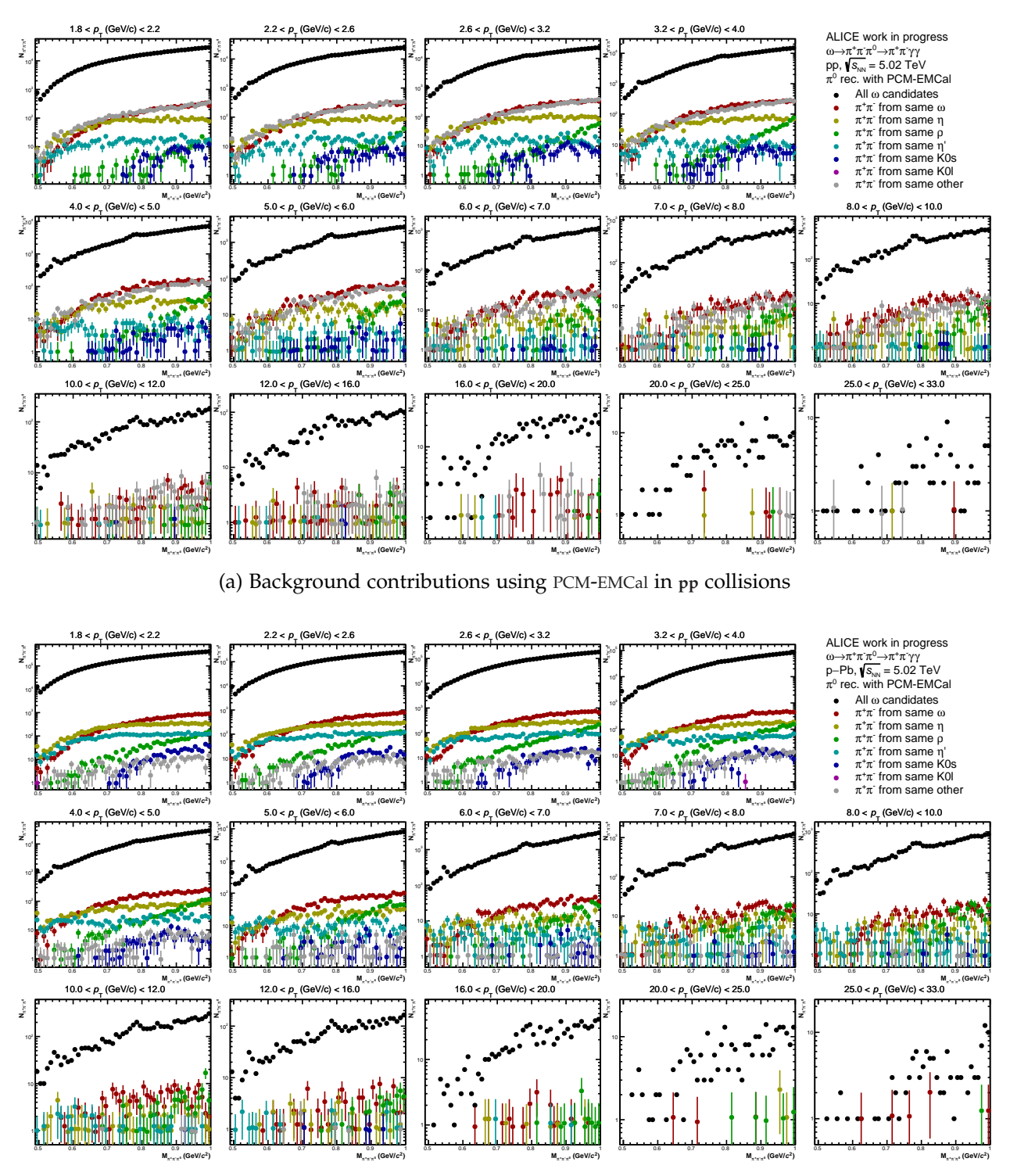


Figure A.16: Breakdown of the background contributions to the invariant mass distribution, where the π^+ and π^- come from the same mother using PCM

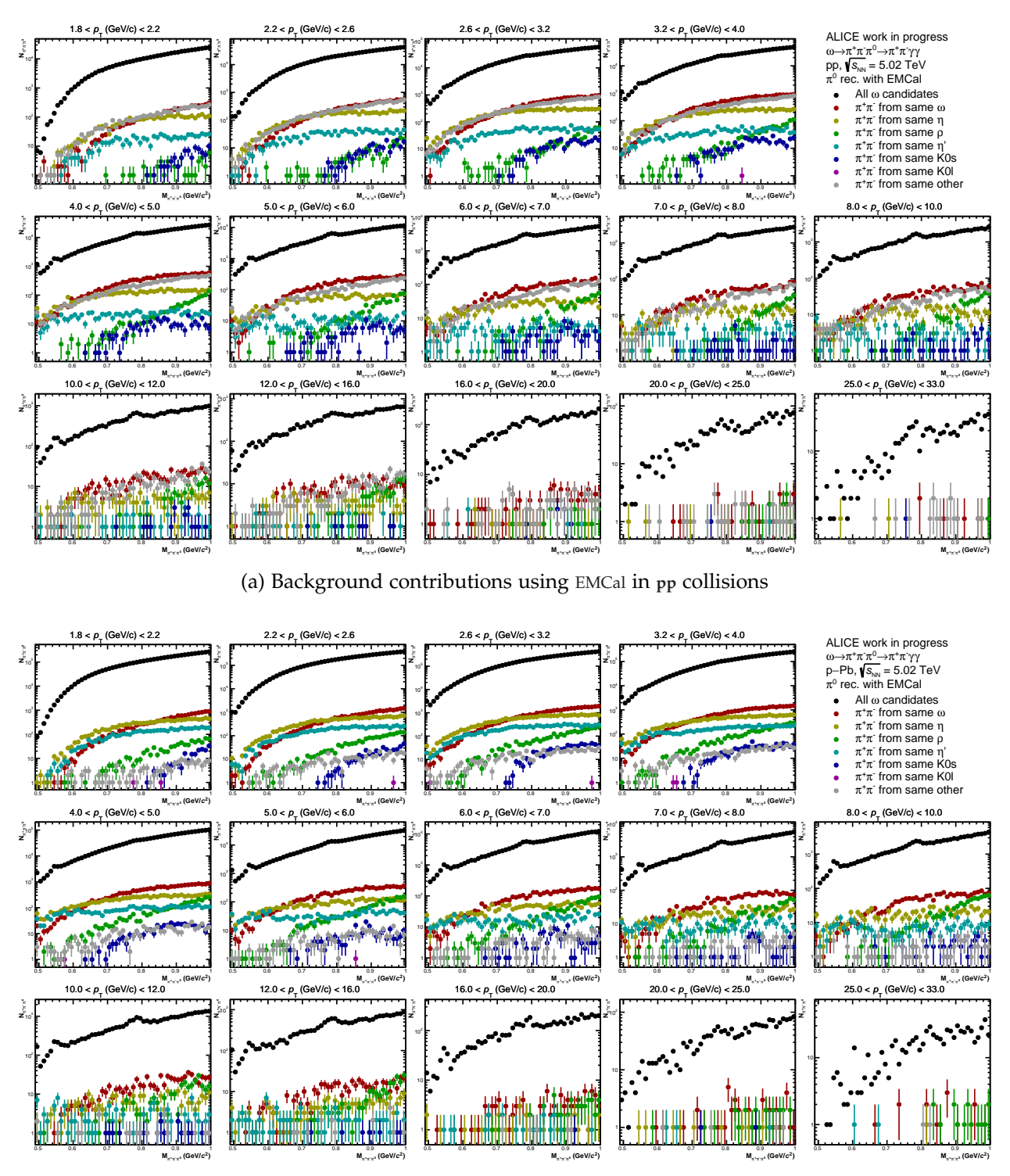
Background contributions of two correlated pions using PCM-EMCal



(b) Background contributions using PCM-EMCal in p-Pb collisions

Figure A.17: Breakdown of the background contributions to the invariant mass distribution, where the π^+ and π^- come from the same mother using PCM-EMCal

Background contributions of two correlated pions using EMCal



(b) Background contributions using EMCal in p-Pb collisions

Figure A.18: Breakdown of the background contributions to the invariant mass distribution, where the π^+ and π^- come from the same mother using EMCal

ACRONYMS

ALICE A Large Ion Collider Experiment

ATLAS A Toroidal LHC ApparatuS

BFKL Balitsky-Fadin-Kuraev-Lipatov

CERN Conseil Européen pour la Recherche Nucléaire

CGC Color Glass Condensate

CMS Compact Muon Solenoid

CNM Cold Nuclear Matter

DCA Distance of Closest Approach

DCal Di-Jet Calorimeter

DPM Dual Parton Model

GEANT GEometry ANd Tracking

DGLAP Dokshitzer-Gribov-Lipatov-Alterelli-Parisi

DPM Dual-Parton-Modell

ECRIS Electron Cyclotron Resonance Ion Source

EMC European Muon Collaboration

EMCal Electromagnetic Calorimeter

FAIR Facility for Antiproton and Ion Research

FWHM Full Width at Half Maximum

FF Fragmentation Function

ISR Intersecting Storage Rings

ITS Inner Tracking System

LHC Large Hadron Collider

LHCb LHC beauty

LEIR Low Energy Ion Ring

LINAC Linear Accelerator

MB Minimum Bias

MBW Material Budget Weight

MC Monte-Carlo

MIP Minimum-Ionizing Particle

MRPC Multigap Resistive Plate Chamber

MWPC Multi Wire Proportional Chamber

NSD Non Single Diffractive

Particle Data Group PDG

PHOS Photon Spectrometer

QGP Quark Gluon Plasma

SDD Silicon Drift Detector

Silicon Pixel Detector SPD

SPS Super Proton Synchrotron

SSD Silicon Strip Detector

TPC Time Projection Chamber

TRD Transition Radiation Detector

Time Of Flight TOF

Proton-Proton pр

p-Pb Proton-Lead

Pb-Pb Lead-Lead

PS Proton Synchrotron

Proton Synchrotron Booster PSB

pQCD perturbative QCD

PDF Parton Distribution Function

BLUE Best Linear Unbiased Estimator

Photon Conversion Method **PCM**

PID Particle Identification

PHENIX Pioneering High Energy Nuclear Interaction eXperiment

RMS Root Mean Square Value

Quality Assurance QA

Quantum Field Theory QFT

QCD Quantum Chromodynamics

BIBLIOGRAPHY

- [ALI99] ALICE. ALICE Inner Tracking System (ITS): Technical Design Report. Technical design report. ALICE. Geneva: CERN, 1999. URL: https://cds.cern.ch/record/391175.
- [Aai+23] Roel Aaij et al. "Nuclear modification factor of neutral pions in the forward and backward regions in *p*Pb collisions." In: *Phys. Rev. Lett.* 131 (2023), p. 042302. DOI: 10.1103/PhysRevLett.131.042302. arXiv: 2204.10608. URL: https://cds.cern.ch/record/2807334.
- [Aam+o8] K. Aamodt et al. "The ALICE experiment at the CERN LHC." In: *JINST* 3 (2008), So8002. DOI: 10.1088/1748-0221/3/08/S08002.
- [Abb+13] E. Abbas et al. "Performance of the ALICE VZERO system." In: JINST 8 (2013), P10016. DOI: 10.1088/1748-0221/8/10/P10016. arXiv: 1306.3130 [nucl-ex].
- [Abe+12] B. Abelev et al. "Neutral pion and η meson production in proton-proton collisions at $\sqrt{s}=0.9$ TeV and $\sqrt{s}=7$ TeV." In: *Phys. Lett. B* 717 (2012), pp. 162–172. DOI: 10.1016/j.physletb.2012.09.015. arXiv: 1205.5724 [hep-ex].
- [Abe+14a] Betty Bezverkhny Abelev et al. "Measurement of visible cross sections in proton-lead collisions at $\sqrt{s_{\mathrm{NN}}}=5.02$ TeV in van der Meer scans with the ALICE detector." In: *JINST* 9.11 (2014), P11003. DOI: 10.1088/1748-0221/9/11/P11003. arXiv: 1405.1849 [nucl-ex].
- [Abe+14b] Betty Bezverkhny Abelev et al. "Neutral pion production at midrapidity in pp and Pb-Pb collisions at $\sqrt{s_{\mathrm{NN}}}=2.76\,\mathrm{TeV}$." In: *Eur. Phys. J. C* 74.10 (2014), p. 3108. DOI: 10.1140/epjc/s10052-014-3108-8. arXiv: 1405.3794 [nucl-ex].
- [Abe+14c] Betty Bezverkhny Abelev et al. "Performance of the ALICE Experiment at the CERN LHC." In: *Int. J. Mod. Phys. A* 29 (2014), p. 1430044. DOI: 10.1142/S0217751X14300440. arXiv: 1402.4476 [nucl-ex].
- [Abe+13] Betty Abelev et al. "Transverse momentum distribution and nuclear modification factor of charged particles in p-Pb collisions at $\sqrt{s_{NN}}=5.02$ TeV." In: *Phys. Rev. Lett.* 110.8 (2013), p. 082302. DOI: 10.1103/PhysRevLett.110.082302. arXiv: 1210.4520 [nucl-ex].

- [Ach+17] Shreyasi Acharya et al. "Production of π^0 and η mesons up to high transverse momentum in pp collisions at 2.76 TeV." In: *Eur. Phys. J. C* 77.5 (2017), p. 339. DOI: 10.1140/epjc/s10052-017-4890-x. arXiv: 1702.00917 [hep-ex].
- [Ach+18a] Shreyasi Acharya et al. "ALICE 2017 luminosity determination for pp collisions at $\sqrt{s} = 5$ TeV." In: (2018). URL: http://cds.cern.ch/record/2648933.
- [Ach+18b] Shreyasi Acharya et al. "Neutral pion and η meson production in p-Pb collisions at $\sqrt{s_{\rm NN}}=5.02$ TeV." In: *Eur. Phys. J. C* 78.8 (2018), p. 624. DOI: 10.1140/epjc/s10052-018-6013-8. arXiv: 1801.07051 [nucl-ex].
- [Ach+18c] Shreyasi Acharya et al. " π^0 and η meson production in proton-proton collisions at $\sqrt{s}=8$ TeV." In: *Eur. Phys. J. C* 78.3 (2018), p. 263. DOI: 10.1140/epjc/s10052-018-5612-8. arXiv: 1708.08745 [hep-ex].
- [Ach+19] Shreyasi Acharya et al. "Dielectron and heavy-quark production in inelastic and high-multiplicity proton–proton collisions at $\sqrt{s_{NN}}=$ 13TeV." In: *Phys. Lett. B* 788 (2019), pp. 505–518. DOI: 10.1016/j.physletb.2018.11.009. arXiv: 1805.04407 [hep-ex].
- [Ach+20] Shreyasi Acharya et al. "Production of ω mesons in pp collisions at $\sqrt{s} = 7$ TeV." In: *Eur. Phys. J. C* 80.12 (2020), p. 1130. DOI: 10.1140/epjc/s10052-020-08651-y. arXiv: 2007.02208 [nucl-ex].
- [Ach+22] Shreyasi Acharya et al. "Nuclear modification factor of light neutral-meson spectra up to high transverse momentum in p–Pb collisions at sNN=8.16 TeV." In: *Phys. Lett. B* 827 (2022), p. 136943. DOI: 10.1016/j.physletb.2022. 136943. arXiv: 2104.03116 [nucl-ex].
- [Ach+23] Shreyasi Acharya et al. "Data-driven precision determination of the material budget in ALICE." In: (Mar. 2023). arXiv: 2303.15317 [physics.ins-det].
- [Ada+16] Jaroslav Adam et al. "Direct photon production in Pb-Pb collisions at $\sqrt{s_{NN}}=$ 2.76 TeV." In: *Phys. Lett. B* 754 (2016), pp. 235–248. DOI: 10.1016/j. physletb.2016.01.020. arXiv: 1509.07324 [nucl-ex].
- [Ada+11a] A. Adare et al. "Measurement of neutral mesons in p+p collisions at $\sqrt{s}=200$ GeV and scaling properties of hadron production." In: *Phys. Rev. D* 83 (5 2011), p. 052004. DOI: 10.1103/PhysRevD.83.052004. URL: https://link.aps.org/doi/10.1103/PhysRevD.83.052004.
- [Ada+11b] A. Adare et al. "Production of ω mesons in p+p, d+Au, Cu+Cu, and Au+Au collisions at $\sqrt{s_{NN}}=200$ GeV." In: *Phys. Rev. C* 84 (4 2011), p. 044902. DOI: 10.1103/PhysRevC.84.044902. URL: https://link.aps.org/doi/10.1103/PhysRevC.84.044902.
- [Alb12] Javier L. Albacete. *Testing the CGC in proton-lead collisions at the LHC*. 2012. arXiv: 1209.0336 [hep-ph].

- [Alm+10] J. Alme et al. "The ALICE TPC, a large 3-dimensional tracking device with fast readout for ultra-high multiplicity events." In: Nuclear Instruments and Methods in Physics Research Section A: Accelerators, Spectrometers, Detectors and Associated Equipment 622.1 (2010), pp. 316–367. DOI: 10.1016/j.nima.2010.04.042. URL: https://doi.org/10.1016%2Fj.nima.2010.04.042.
- [AP77] G. Altarelli and G. Parisi. "Asymptotic freedom in parton language." In: Nuclear Physics B 126.2 (1977), pp. 298–318. ISSN: 0550-3213. DOI: https://doi.org/10.1016/0550-3213(77)90384-4. URL: https://www.sciencedirect.com/science/article/pii/0550321377903844.
- [Alt+17] Lucas Altenkämper et al. "Applicability of transverse mass scaling in hadronic collisions at energies available at the CERN Large Hadron Collider." In: *Physical Review C* 96.6 (Dec. 2017). ISSN: 2469-9993. DOI: 10.1103/physrevc.96.064907. URL: http://dx.doi.org/10.1103/PhysRevC.96.064907.
- [Ams18] Claude Amsler. *The Quark Structure of Hadrons*. Ed. by W. Beiglböck et al. Vol. 949. Springer, 2018. ISBN: 978-3-319-98526-8. DOI: 10.1007/978-3-319-98527-5.
- [And+83] B. Andersson et al. "Parton fragmentation and string dynamics." In: *Physics Reports* 97.2 (1983), pp. 31–145. ISSN: 0370-1573. DOI: https://doi.org/10.1016/0370-1573(83)90080-7. URL: https://www.sciencedirect.com/science/article/pii/0370157383900807.
- [Ang+93] N Angert et al. CERN heavy-ion facility design report. CERN Yellow Reports: Monographs. Geneva: CERN, 1993. DOI: 10.5170/CERN-1993-001. URL: https://cds.cern.ch/record/249000.
- [AGK20] E. Annala, T. Gorda, and A. et al. Kurkela. "Evidence for quark-matter cores in massive neutron stars." In: *Nat. Phys.* 16 (2020), pp. 907–910. DOI: https://doi.org/10.1038/s41567-020-0914-9.
- [Armo6] Néstor Armesto. "Nuclear shadowing." In: *Journal of Physics G: Nuclear and Particle Physics* 32.11 (2006), R367–R393. ISSN: 1361-6471. DOI: 10.1088/0954-3899/32/11/r01. URL: http://dx.doi.org/10.1088/0954-3899/32/11/R01.
- [Aub+83] J.J. Aubert et al. "The ratio of the nucleon structure functions F2N for iron and deuterium." In: *Physics Letters B* 123.3 (1983), pp. 275–278. ISSN: 0370-2693. DOI: https://doi.org/10.1016/0370-2693(83)90437-9. URL: https://www.sciencedirect.com/science/article/pii/0370269383904379.
- [Bal15] A. Baldisseri. "The ALICE MUON Arm." MFT Meeting, Hiroshima. 2015. URL: https://indico.cern.ch/event/448477/contributions/1942927.
- [Baz+14] A. Bazavov et al. "Equation of state in (2+1)-flavor QCD." In: *Physical Review D* 90.9 (2014). DOI: 10.1103/physrevd.90.094503. URL: https://doi.org/10.1103%2Fphysrevd.90.094503.

- [Bie+22] Christian Bierlich et al. *A comprehensive guide to the physics and usage of PYTHIA 8.3.* 2022. arXiv: 2203.11601 [hep-ph].
- [Bir11] Ian Bird. "Computing for the Large Hadron Collider." In: Annual Review of Nuclear and Particle Science 61.1 (2011), pp. 99–118. DOI: 10.1146/annurev-nucl-102010-130059. eprint: https://doi.org/10.1146/annurev-nucl-102010-130059.
- [BGVo4] Jean-Paul Blaizot, François Gelis, and Raju Venugopalan. "High energy pA collisions in the color glass condensate approach I: gluon production and the Cronin effect." In: *Nuclear Physics A* 743.1-3 (2004), pp. 13–56. DOI: 10.1016/j.nuclphysa.2004.07.005. URL: https://doi.org/10.1016%2Fj.nuclphysa.2004.07.005.
- [Boc17] Friederike Bock. "Measurement of Direct Photons and Neutral Mesons in Small Collisions Systems with the ALICE Experiment at the LHC." PhD thesis. Ruperto-Carola University of Heidelberg, 2017. URL: https://archiv.ub.uni-heidelberg.de/volltextserver/23888/1/PHDThesis_SubmissionVersion_20171016.pdf.
- [BSS21] Friederike Bock, Nicolas Schmidt, and Mike Sas. Multiplicity dependence of neutral meson & direct photon production in pPb 5TeV. https://alicenotes.web.cern.ch/node/1126. 2021.
- [Bol+79] E. Boltezar et al. "Performance of the New CERN 50 MeV Linac." In: *IEEE Transactions on Nuclear Science* 26.3 (1979), pp. 3674–3676. DOI: 10.1109/TNS. 1979.4330576.
- [Bon+o5] M. Bondila et al. "ALICE To detector." In: *IEEE Trans. Nucl. Sci.* 52 (2005), pp. 1705–1711. DOI: 10.1109/TNS.2005.856900.
- [Bre+89] A. Breakstone et al. "Production of Meson Resonances as Leading Particles in Jets in Proton Proton Collisions at $\sqrt{s} = 62$ -GeV at the CERN ISR." In: Z. *Phys. C* 43 (1989), p. 185. DOI: 10.1007/BF01588205.
- [Bru+04] Oliver Sim Bruening et al. *LHC Design Report*. CERN Yellow Reports: Monographs. Geneva: CERN, 2004. DOI: 10.5170/CERN-2004-003-V-1. URL: https://cds.cern.ch/record/782076.
- [Bru+87] R Brun et al. *GEANT 3: user's guide Geant 3.10, Geant 3.11; rev. version*. Geneva: CERN, 1987. URL: https://cds.cern.ch/record/1119728.
- [Bü21] Henner Büsching. *Kern- und Teilchenphysik 4b: Die Physik des Quark-Gluon-Plasmas*. Lecture notes. 2021.

- [Car19] F. Carnesecchi. "Performance of the ALICE Time-Of-Flight detector at the LHC." In: *Journal of Instrumentation* 14.06 (2019), pp. Co6023–Co6023. DOI: 10.1088/1748-0221/14/06/c06023. URL: https://doi.org/10.1088% 2F1748-0221%2F14%2F06%2Fc06023.
- [Tra] Charged Track QA. https://twiki.cern.ch/twiki/bin/view/Main/QA: ChargedTracks. Accessed: 2023-02-20.
- [Cor+o8] P. Cortese et al. *ALICE Electromagnetic Calorimeter Technical Design Report*. Tech. rep. 2008. URL: https://cds.cern.ch/record/1121574.
- [Del+oo] G. Dellacasa et al. "ALICE technical design report of the time-of-flight system (TOF)." In: (Feb. 2000).
- [DLR15] Luigi Di Lella and Carlo Rubbia. "The Discovery of the W and Z Particles." In: *Adv. Ser. Dir. High Energy Phys.* 23 (2015), pp. 137–163. DOI: 10.1142/9789814644150_0006. URL: https://cds.cern.ch/record/2103277.
- [Dia10] Dmitri Diakonov. "QCD scattering: from DGLAP to BFKL." In: CERN courier (2010). URL: https://cerncourier.com/a/qcd-scattering-from-dglap-to-bfkl/ (visited on 10/06/2023).
- [Don+8o] G. J. Donaldson et al. "Observation of inclusive ω production at large transverse momentum." In: *Phys. Rev. D* 21 (3 1980), pp. 828–830. DOI: 10. 1103 / PhysRevD. 21.828. URL: https://link.aps.org/doi/10.1103/PhysRevD.21.828.
- [DGH94] J. Donoghue, E. Golowich, and B Holstein. *Dynamics of the Standard Model*. Cambridge University Press, 1994.
- [Wik] EMC effect Wikipedia, The Free Encyclopedia. Accessed: 2023-10-18. URL: https://en.wikipedia.org/wiki/EMC_effect.
- [Esk19] K.J. Eskola. "Nearly perfect quark–gluon fluid." In: *Nat. Phys.* 15 (2019), 1111–1112. DOI: https://doi.org/10.1038/s41567-019-0643-0.
- [Fer74] Enrico Fermi. Nuclear Physics: A Course Given by Enrico Fermi at the University of Chicago. The university of chicago press, 1974.
- [Fid15] Giuseppe Fidecaro. 60 Years of CERN Experiments and Discoveries. World Scientific, 2015, pp. 397–414.
- [GEL13] FRANÇOIS GELIS. "Color glass condensate and glasma." In: *International Journal of Modern Physics A* 28.01 (2013), p. 1330001. DOI: 10.1142/s0217751x13300019. URL: https://doi.org/10.1142%2Fs0217751x13300019.
- [Gel+63] N. Gelfand et al. "Lifetime of the ω Meson." In: *Phys. Rev. Lett.* 11 (9 1963), pp. 436–438. DOI: 10.1103/PhysRevLett.11.436. URL: https://link.aps.org/doi/10.1103/PhysRevLett.11.436.

- [Gel+10] Francois Gelis et al. "The Color Glass Condensate." In: *Ann. Rev. Nucl. Part. Sci.* 60 (2010), pp. 463–489. DOI: 10.1146/annurev.nucl.010909.083629. arXiv: 1002.0333 [hep-ph].
- [GM61] M Gell-Mann. "The Eightfold way: A theory of strong interaction symmetry." In: (Mar. 1961). DOI: 10.2172/4008239. URL: https://www.osti.gov/biblio/4008239.
- [Gli+19] Vladimir V. Gligorov et al. "Leveraging the ALICE/L3 cavern for long-lived particle searches." In: *Physical Review D* 99.1 (2019). DOI: 10.1103/physrevd. 99.015023. URL: https://doi.org/10.1103%2Fphysrevd.99.015023.
- [Gli] Ewa Glimos. "Eta prime result in pp." Soft Photons and Neutral Mesons PAG Meeting. URL: https://indico.cern.ch/event/1312983/#2-eta-prime-result-in-pp.
- [Gri67] V. N. Gribov. "A Reggeon diagram technique." In: *Zh. Eksp. Teor. Fiz.* 53 (1967), pp. 654–672.
- [Hem21] Marvin Hemmer. Analyse von $\omega \to \pi^0 \gamma$ in pp-Kollisionen bei $\sqrt{s}=13$ TeV mit dem ALICE EMCal. 2021.
- [Hen+17] Or Hen et al. "Nucleon-nucleon correlations, short-lived excitations, and the quarks within." In: *Reviews of Modern Physics* 89.4 (2017). DOI: 10.1103/revmodphys.89.045002. URL: https://doi.org/10.1103%2Frevmodphys.89.045002.
- [Hon79] M A Hone. *The duoplasmatron ion source for the new CERN Linac preinjector*. Tech. rep. Geneva: CERN, 1979. URL: https://cds.cern.ch/record/2640736.
- [Hor21] Fabian Hordt. Reconstruction of Partonic Substructure and Fragmentation of Jets in Heavy Ion Collisions at the LHC. 2021.
- [Jon23] Florian Jonas. "Probing the initial state of heavy-ion collisions with isolated prompt photons." PhD thesis. Westfälische Wilhelms-Universität Münster, 2023. URL: https://cds.cern.ch/record/2875942.
- [Kan19] Zhongbo Kang. "Small-x physics and gluon saturation." LPC Workshop on Physics Connections between the LHC and EIC. 2019. URL: https://indico. cern.ch/event/853569/contributions/3633694/attachments/1945927/ 3228523/Kang-smallx.pdf.
- [Kha20] Zhanna Khabanova. "Studies of collective effects in pp collisions at the LHC with the balance function for identified particles." Presented 02 Dec 2020. Utrecht U., 2020. URL: https://cds.cern.ch/record/2747217.
- [Kla23] Michael Klasen. "Nuclear PDFs after 10 years of LHC data." ALICE FSP Meeting. 2023.

- [Koc11] Kathrin Koch. " π^0 and η measurement with photon conversions in ALICE in proton-proton collisions at $\sqrt{s}=7$ TeV." In: *Nuclear Physics A* 855.1 (2011), pp. 281–284. DOI: 10.1016/j.nuclphysa.2011.02.059. URL: https://doi.org/10.1016%2Fj.nuclphysa.2011.02.059.
- [Koe20] Joshua Leon Koenig. Measurement of neutral pions and η in pp Collisions at \sqrt{s} =13TeV with ALICE. https://alice-notes.web.cern.ch/node/1067. 2020.
- [Koe22] Joshua Leon Koenig. "Measurement of neutral meson production as a function of multiplicity in pp collisions at $\sqrt{s}=13~TeV$ with ALICE." Quark Matter 2022 the XXIXth International Conference on Ultra-relativistic Nucleus-Nucleus Collisions. 2022. URL: https://indico.cern.ch/event/895086/contributions/4723711/.
- [Kra+64] Robert Kraemer et al. "Meson Resonance Production in π^+-d Interactions at 1.23 BeV/c." In: *Phys. Rev.* 136 (2B 1964), B496–B506. DOI: 10.1103/PhysRev. 136.B496. URL: https://link.aps.org/doi/10.1103/PhysRev.136.B496.
- [Kö23] Joshua König. "Measurement of light neutral meson production inside jets in pp collisions at \sqrt{s} = 13TeV with ALICE." Quark Matter 2019 the XXXth International Conference on Ultra-relativistic Nucleus-Nucleus Collisions. 2023. URL: https://indico.cern.ch/event/1139644/contributions/5456410/.
- [LW95] G.D. Lafferty and T.R. Wyatt. "Where to stick your data points: The treatment of measurements within wide bins." In: Nuclear Instruments and Methods in Physics Research Section A: Accelerators, Spectrometers, Detectors and Associated Equipment 355.2 (1995), pp. 541–547. ISSN: 0168-9002. DOI: https://doi.org/10.1016/0168-9002(94)01112-5. URL: https://www.sciencedirect.com/science/article/pii/0168900294011125.
- [Lip12] Christian Lippmann. "Performance of the ALICE Time Projection Chamber." In: *Physics Procedia* 37 (2012). Proceedings of the 2nd International Conference on Technology and Instrumentation in Particle Physics (TIPP 2011), pp. 434–441. ISSN: 1875-3892. DOI: https://doi.org/10.1016/j.phpro.2012.02.390. URL: https://www.sciencedirect.com/science/article/pii/S187538921201721X.
- [Lis17] Luca Lista. "Combination of measurements and the BLUE method." In: *EPJ Web of Conferences* 137 (2017). Ed. by Y. Foka, N. Brambilla, and V. Kovalenko, p. 11006. DOI: 10.1051/epjconf/201713711006. URL: https://doi.org/10.1051%2Fepjconf%2F201713711006.

- [Lue22] Jens Robert Luehder. Measurement of ω meson production at mid-rapidity with ALICE in pp collisions at \sqrt{s} =13TeV. https://alice-notes.web.cern.ch/node/1313. 2022.
- [Lü23] Jens Lühder. "Measurement of ω mesons in pp collisions in \sqrt{s} = 13TeV at the LHC with ALICE." 11th International Conference on Hard and Electromagnetic Probes of High-Energy Nuclear Collisions. 2023. URL: https://www.indico.uni-muenster.de/event/1409/contributions/2175/.
- [Ma+19] Guo-Yang Ma et al. "NLO Productions of ω and K_S^0 with a global extraction of the jet transport parameter in heavy-ion collisions." In: *The European Physical Journal C* 79.6 (2019). DOI: 10.1140/epjc/s10052-019-7005-z. URL: https://doi.org/10.1140%2Fepjc%2Fs10052-019-7005-z.
- [MT45] L. Mandelstam and Ig. Tamm. "The uncertainty relation between energy and time in non-relativistic quantum mechanics." In: *Journal of Physics* 9 (4 1945). URL: http://daarb.narod.ru/mandtamm/mt-eng.pdf.
- [Man+99] V I Man'ko et al. *ALICE Photon Spectrometer (PHOS): Technical Design Report.*Technical design report. ALICE. Geneva: CERN, 1999. URL: https://cds.cern.ch/record/381432.
- [MPCo4] Felix Matathias and (for the PHENIX Collaboration). " π /K/p production and Cronin effect from p+p, d+Au and Au+Au collisions at 200 GeV from the PHENIX experiment." In: *Journal of Physics G: Nuclear and Particle Physics* 30.8 (2004), S1113–S1116. DOI: 10.1088/0954-3899/30/8/070. URL: https://doi.org/10.1088%2F0954-3899%2F30%2F8%2F070.
- [McLo2] Larry McLerran. "The Color Glass Condensate, RHIC and HERA." In: DIS2002. 2002. URL: https://www.bnl.gov/isd/documents/24457.pdf.
- [McLo8a] Larry McLerran. "A Brief Introduction to the Color Glass Condensate and the Glasma." In: *International Symposium on Multiparticle Dynamics*. 2008. DOI: http://dx.doi.org/10.3204/DESY-PROC-2009-01/26. URL: https://bib-pubdbl.desy.de/record/296833/files/ismd08_mcl_intro-corr.pdf.
- [McLo8b] Larry McLerran. Gluon Saturation and the Formation Stage of Heavy Ion Collisions. 2008. arXiv: 0807.4095 [hep-ph].
- [Mee68] S van der Meer. *Calibration of the effective beam height in the ISR*. Tech. rep. Geneva: CERN, 1968. URL: https://cds.cern.ch/record/296752.
- [Nam57] Yoichiro Nambu. "Possible Existence of a Heavy Neutral Meson." In: *Phys. Rev.* 106 (6 1957), pp. 1366–1367. DOI: 10.1103/PhysRev.106.1366. URL: https://link.aps.org/doi/10.1103/PhysRev.106.1366.

- [Noro3] P R Norton. "The EMC effect." In: Reports on Progress in Physics 66.8 (2003), p. 1253. DOI: 10.1088/0034-4885/66/8/201. URL: https://dx.doi.org/10. 1088/0034-4885/66/8/201.
- [Atl] "Observation of a new particle in the search for the Standard Model Higgs boson with the ATLAS detector at the LHC." In: *Physics Letters B* 716.1 (2012), pp. 1–29. DOI: 10.1016/j.physletb.2012.08.020. URL: https://doi.org/10.1016%2Fj.physletb.2012.08.020.
- [Alia] "Performance of the ALICE Electromagnetic Calorimeter." In: (Sept. 2022). arXiv: 2209.04216 [physics.ins-det].
- [Phi20] Owe Philipsen. "Numerical Determination of the Phase Diagram of Hadronic and Nuclear Matter." Online; abgerufen am 30 April 2021. 2020. URL: https://www.gauss-centre.eu/results/elementaryparticlephysics/article/numerical-determination-of-the-phase-diagram-of-nuclear-matter/.
- [Pie+15] T. Pierog et al. "EPOS LHC: Test of collective hadronization with data measured at the CERN Large Hadron Collider." In: *Physical Review C* 92.3 (2015). DOI: 10.1103/physrevc.92.034906. URL: https://doi.org/10.1103% 2Fphysrevc.92.034906.
- [Pla49] Max Planck. "The Meaning and Limits of Exact Science." In: *Science* 110 (1949), pp. 319–327. DOI: 10.1126/science.110.2857.319.
- [PPW10] S. Porteboeuf, T. Pierog, and K. Werner. *Producing Hard Processes Regarding the Complete Event: The EPOS Event Generator*. 2010. arXiv: 1006.2967 [hep-ph].
- [Pov+13] Bogdan Povh et al. *Teilchen und Kerne*. Vol. 9. Springer, 2013. ISBN: 978-3-642-37822-5.
- [Fri] Proceedings of the 1974 CERN School of Computing: Godøysund, Norway 11 24
 Aug 1974. 3rd CERN School of Computing. CERN. Geneva: CERN, 1974. DOI:
 10.5170/CERN-1974-023. URL: https://cds.cern.ch/record/186223.
- [Reg62] Edouard Regenstreif. The CERN Proton Synchrotron. CERN Yellow Reports: Monographs. French version published as CERN 61-09. Geneva: CERN, 1962. DOI: 10.5170/CERN-1962-003. URL: https://cds.cern.ch/record/278715.
- [Rei69] K H Reich. "THE CERN PROTON SYNCHROTRON BOOSTER." In: *IEEE* (*Inst. Elec. Electron. Eng.*), *Trans. Nucl. Sci.*, *NS-16*: 959- 61(*June* 1969). (Jan. 1969). DOI: 10.1109/TNS.1969.4325414. URL: https://www.osti.gov/biblio/4773934.

- [RER01] S. Roesler, R. Engel, and J. Ranft. "The Monte Carlo Event Generator DPMJET-III." In: *Advanced Monte Carlo for Radiation Physics, Particle Transport Simulation and Applications*. Springer Berlin Heidelberg, 2001, pp. 1033–1038. DOI: 10.1007/978-3-642-18211-2_166. URL: https://doi.org/10.1007% 2F978-3-642-18211-2_166.
- [Sal+11] C A Salgado et al. "Proton-nucleus collisions at the LHC: scientific opportunities and requirements." In: *Journal of Physics G: Nuclear and Particle Physics* 39.1 (2011), p. 015010. ISSN: 1361-6471. DOI: 10.1088/0954-3899/39/1/015010. URL: http://dx.doi.org/10.1088/0954-3899/39/1/015010.
- [Sas19] Mike Sas. "Light neutral meson production in heavy ion collisions with ALICE in the era of precision physics at the LHC." Quark Matter 2019 the XXVIIIth International Conference on Ultra-relativistic Nucleus-Nucleus Collisions. 2019. URL: https://indico.cern.ch/event/792436/contributions/3547545/.
- [SI17] H. Saveetha and D. Indumathi. "Fragmentation of ω and ϕ mesons in e^+e^- and pp collisions at NLO." In: *International Journal of Modern Physics A* 32.33 (2017), p. 1750199. DOI: 10.1142/s0217751x17501998.
- [SS19] Nicolas Schmidt and Mike Sas. *Combination of different neutral meson measure- ments in pp collisions at 5.02 TeV*. https://alice-notes.web.cern.ch/node/
 924. 2019.
- [SE] Stannered and E2m. *Meson Wikipedia, The Free Encyclopedia*. Accessed: 2023-06-20. URL: https://en.wikipedia.org/wiki/Meson.
- [Str21] Nicolas Strangmann. Messung von ω -Mesonen in Proton-Blei-Kollisionen bei $\sqrt{s_{NN}}=5,02\,\text{TeV}$. Bachelor's Thesis. 2021.
- [Alib] "The ALICE experiment A journey through QCD." In: (Nov. 2022). arXiv: 2211.04384 [nucl-ex].
- [Tsa88] Constantino Tsallis. "Possible generalization of Boltzmann-Gibbs statistics." In: *Journal of Statistical Physics* 52 (1988), pp. 479–487. URL: https://doi.org/10.1007/BF01016429.
- [Pdg22] R. L. et al. (Particle Data Group) Workman. "Review of Particle Physics." In: *Prog. Theor. Exp. Phys.* (2022), p. 083Co1. DOI: 10.1093/ptep/ptac097.

An experiment is a question which science poses to Nature, and a measurement is the recording of Nature's answer.

— Max Planck [Pla49]

ACKNOWLEDGMENTS

Looking back on the journey of the past two years that led to this thesis, I would like to take this opportunity to extend my deepest gratitude to those who have made this journey not only possible but also immensely enjoyable.

First and foremost, I am particularly thankful to *Prof. Dr. Henner Büsching* for welcoming me into his working group and fully integrating me into the scientific community of ALICE.

I am immensely grateful to *Joshua König* for much more than just supervising the analysis but also offering constant inspiration and tireless support.

Special thanks are due to *Dr. Friederike Bock* for her mentorship and incredible expertise, covering the entire spectrum from trigger rejection factors to detector construction, even extending to horseback riding.

I extend my appreciation to *Dr. Florian Jonas* and *Dr. Ana Marin*, who volunteered to form the analysis review committee, whose critical questions and expertise immensely solidified the analysis.

My heartfelt thanks go to my entire *working group* in Frankfurt for so many fruitful discussions and creative endeavors related to physics and beyond.

Lastly, I must express my deepest gratitude to my *parents*, who have been my unwavering support system throughout this journey. Their endless encouragement and all-encompassing support have been the bedrock of my achievements.

EIGENSTÄNDIGKEITSERKLÄRUNG

Erklärung nach §30 (12) Ordnung für den Bachelor- und dem Masterstudiengang

Hiermit erkläre ich, dass ich die Arbeit selbstständig und ohne Benutzung anderer als der angegebenen Quellen und Hilfsmittel verfasst habe. Alle Stellen der Arbeit, die wörtlich oder sinngemäß aus Veröffentlichungen oder aus anderen fremden Texten entnommen wurden, sind von mir als solche kenntlich gemacht worden. Ferner erkläre ich, dass die Arbeit - auch nicht auszugsweise - für eine andere Prüfung verwendet wurde.

| Frankfurt, November 2023 | |
|--------------------------|--------------------|
| | |
| | |
| | Nicolas Strangmann |